3D Bioprinting Tissue Scaffolds with Living Cells for Tissue Engineering Applications

A Thesis Submitted to

the College of Graduate and Postdoctoral Studies

in Partial Fulfillment of the Requirements for

the Degree of Doctor of Philosophy

in the Department of Mechanical Engineering

University of Saskatchewan

By

Liqun Ning

PERMISSION TO USE

In presenting this thesis in partial fulfilment of the requirements for a postgraduate degree from the University of Saskatchewan, I agree that the Libraries of this University may make it freely available for inspection. I further agree that permission for copying of this thesis in any manner, in whole or in part, for scholarly purpose may be granted by the professor who supervised my thesis work, or in their absence, by the Head of the Department or the Dean of the College in which my thesis work was done. It is understood that any copying or publication or use of this thesis or part thereof for financial gain shall not be allowed without my written permission. It is also understood that due recognition shall be given to me and to the University of Saskatchewan in any scholarly use which may be made of any material in my thesis.

Requests for permission to copy or to make other use of material in this thesis in whole or part should be addressed to:

College of Graduate and Postdoctoral Studies
116 Thorvaldson Building
110 Science Place
University of Saskatchewan
Saskatoon, Saskatchewan (S7N 5C9)

OR

Head of the Department of Mechanical Engineering
57 Campus Dr.
University of Saskatchewan
Saskatoon, Saskatchewan (S7N 5A9)

ABSTRACT

In tissue engineering, tissue scaffolds are used as temporary supports to promote regeneration of dysfunctional tissues. Of the available strategies, scaffolds produced from hydrogels and living cells show the great potential for their enhanced biological properties. To produce such scaffolds, three-dimensional (3D) bioprinting has evolved and is showing promise as a fabrication technique. However, its applications for fabricating customized hydrogel scaffolds containing living cells is still in its infancy. The major challenge with this approach is to print scaffolds while preserving cell viability and functionality as well as ensuring the structural integrity of the scaffold. To overcome this challenge, the present thesis aims to investigate the influences of hydrogel properties and the bioprinting process on cell viability and functionality, while also ensuing structural integrity, and on this basis, to develop bioprinting processes to produce tissue scaffolds with living cells for potential tissue engineering applications.

This thesis first examined the influence of the mechanical properties of hydrogel on cell viability and functionality, utilizing alginate hydrogels and Schwann cells (the major glial cells of peripheral nervous system). Due to its poor cell adhesion, the alginate hydrogel was modified in this study with cell-adhesion supplements, including fibronectin, poly-l-lysine (PLL), and RGD (Arg-Gly-Asp) peptides. The RGD-modified alginate substrates were prepared with varying alginate concentrations in order to alter the mechanical properties of hydrogels, which were then seeded and encapsulated with Schwann cells. Cell viability and functionality, including proliferation, morphology, and expression of the extracellular matrix protein, were examined and correlated to the hydrogel mechanical properties. The results demonstrate that the viability and functionality of Schwann cells within alginate-based hydrogel vary with hydrogel mechanical properties, thus highlighting the importance of regulating the mechanical properties of hydrogel for improved cell viability and functionality in scaffold bioprinting.

During the bioprinting process, cells are subject to process-induced forces, such as shear and extensional stresses, which can result in cell damage and therefore loss of cell function and even cell death. A method was developed to study the cell damage introduced by the shear and extensional stresses in the bioprinting process. A plate-and-cone rheometer was adopted to examine the effect of shear stress on cell damage. In these

experiments, the relationship of cell damage to the shear stress was examined and quantified, which was then applied to identify the cell damage attributed to shear stress in bioprinting. On this basis, the damage to cells caused by extensional stress was inferred from the difference between the total cell damage occurring during the bioprinting process and the cell damage attributed to shear stress. This developed method allowed a relationship to be established between cell damage and both shear and extensional stresses during bioprinting. The experiments on this method provide insight into both the cell damage that occurs during bioprinting and the effect on cell viability and proliferative ability thereafter, which can be used to optimize the bioprinting process so as to preserve cell functionality.

Based on the previous investigations, bioprinting processes were developed to fabricate tissue scaffolds containing Schwann cells for potential applications in nerve tissue engineering. Composite hydrogels consisting of alginate, fibrin, hyaluronic acid, and RGD peptide were prepared, and their hydrogel microstructures, mechanical stiffness after gelation, and capability to support the Schwann cell spreading were examined for identifying appropriate composite hydrogel for bioprinting processes. The flow behavior of composite hydrogel solutions and bioprinting process parameters (e.g., dispensing pressure, dispensing head speed, crosslinking process) were then examined with regard to their influence on the structure of the printed scaffolds and on this basis, bioprinting process were developed to fabricate scaffolds with Schwann cells. The functionality of Schwann cells within the printed scaffolds were assessed in terms of cell viability, proliferation, morphology, orientation, and protein expression, demonstrating that the printed scaffolds have potential for nerve tissue engineering applications.

This thesis presents a comprehensive study on the bioprinting of scaffolds with living cells. The method developed and the study results will pave the way to fabricate scaffolds with living cells for more tissue engineering applications.

ACKNOWLEDGMENTS

I would like to express my utmost gratitude to my supervisor, Dr. Daniel Chen, for all his academic advice, suggestions, encouragement and support in my way of pursuing the doctoral degree. I would also like to give my thanks to Dr. David J Schreyer, for his advice and support in many of my biological experiments. I also extend my appreciation to my advisory committee members; Dr. Li Chen, Dr. Fangxiang Wu, and Dr. Scott Noble for their valuable comments.

I would like to thank Dr. James Bugg, Dr. Ning Zhu, Dr. Lifeng Zhang, Dr. Georges Kipouros and Dr. Brian Eames for their guidance in image acquisition, flow dynamics analysis, and biological and mechanical experiments. My thanks also go to Doug Bitner for his technical support during the scaffold bioprinting and mechanical tests.

I acknowledge the finical support from the University of Saskatchewan (via the Devolved Graduate Research Scholarship to me) and from the Saskatchewan Health Research Foundation (SHRF) (via the research grants to Tissue Engineering research group).

I appreciated the support from the Bio-Fabrication lab at the University of Saskatchewan and the Cameco MS Neuroscience Research Center at Saskatoon City Hospital, where most of the experiments presented in this thesis were performed. I would also like to thank the Canadian Light Source (CLS), WCVM Imaging Centre of College of Veterinary Medicine, and Dr. Eames's Laboratory, where the images of samples were obtained. Specifically, I wish to thank Dr. Tuanjie Chang, Peng Zhai, Ning Cao and Eiko Kawamura for their dedicated technical support. In addition, I would like to thank my fellows in Tissue Engineering Research Group, Dr. Ajay Rajaram, Md. Aslam Sarker, Jingwen Li, Dr. Zohreh Izadifar, Dr. Adeola Olubamiji, and Xue Han, who always encouraged and helped me through many thought-provoking discussions. I also would like to thank my colleagues, mentors and friends at the City Hospital, Dr. Valerie Verge, Dr. Ruiling Zhai, Shannon Berko, Jayne Johnston, Anita Givens, and Dr. Nikki McLean, for their valuable suggestions in many cell-culture experiments. I would specially thank Yitong Xu, Arthur Guillemot, Jingxuan Zhao, Nicholas Betancourt, Romain Guilloteau, Tiphanie Lelong, and Haoying Sun, for their assistance in experiments involving cell damage and scaffold bioprinting.

I am grateful to my parents, Hongsheng Ning and Aixia Cong, for their motivation, encouragement, support and dedication. Particularly, I would give my deepest love to my wife, Shuting Kou, who helped me, encouraged me, and took most of the family responsibilities to make me time to focus on research.

TABLE OF CONTENTS

LIST OF TABLES

LIST OF FIGURES

LIST OF ABBREVIATIONS

Abbreviation	Explanation
ANOVA	Analysis of variance
ART	Attenuated total reflectance
BMIT	Biomedical Imaging and Therapy facility
BSA	Bovine Serum Albumin
CAD	Computer-aided design
CFD	Computational fluid dynamics
CLS	Canadian Light Source
CT	Computed tomography
dECM	Decellularized extracellular matrix
DMEM	Dulbecco's Modified Eagle's Medium
DMSO	Dimethyl sulfoxide
EACA	6-aminocaproic acid
ECM	Extracellular matrix
EDTA	Ethylenediaminetetraacetic acid
FBS	Fetal bovine serum
GelMA	Gelatin methacrylate
HA	Hyaluronic acid
IKVAV	le-Lys-Val-Ala-Val
L8	Myoblast cell line
MRI	Magnetic resonance imaging
MTT	3-(4,5-Dimethylthiazol-2-yl)-2,5-diphenyltetrazolium bromide
NHS	N-Hydroxysuccinimide
NIH-3T3	Fibroblast cell line
PCL	Polycaprolactone
PEG	Poly(ethylene glycol)
PEI	Polyethyleneimine
PEO	Poly(ethylene oxide)
PI	Propidium iodide
PLGA	Poly(lactic-co-glycolic acid)

PLL	Poly-l-lysine
PNS	Peripheral nervous system
PS	Penicillin-streptomycin
PVA	Polyvinyl alcohol
RGD	Arg-Gly-Asp
RSC96	Schwann cell line
SD	Standard deviation
SEM	Scanning electron microscopy
SLA	Stereolithography
SMC	Smooth muscle cells
SR-inline-PCI-CT)	Synchrotron-based X-ray inline phase contrast imaging-computed tomography
TBS	Tris-buffered saline
VIC	Aortic valve leaflet interstitial cells
YIGSR	Tyr-Ile-Gly-Ser-Arg
2D	Two-dimensional
2PP	Two photon-polymerization
3D	Three-dimensional

CHAPTER 1

Introduction

1.1 Tissue engineering and scaffolds

The loss or failure of human tissues and organs has become one of the most devastating and costly issues in health care. For example, injuries to the peripheral nervous system (PNS) due to crushing or transection of axons lead to the disconnection of axonal pathways, causing the dysfunction of the body components attached to the nerve distally from the site of injury, leading to deficits such as movement, sensation, and autonomic function [1, 2]. Although nerve axon regeneration is triggered automatically following injuries by the pro-regenerative response of resident Schwann cells, the function recovery is very limited due to poor axonal re-innervation between the separated nerve segments [3]. To promote the regeneration of axons, therapies such as autografts and allografts transplantation of the donor nerves into the targeted sites have been developed. However, problems remain due to the limited availability of donor nerves, mismatch between the injured and donor nerves, and a lack of a supportive construct to organize the growth of nerve tissues and axons [4]. To help alleviate these kinds of problems, a new field, tissue engineering, has emerged.

Tissue engineering is an interdisciplinary field that combines the principles and technologies from engineering, material science, cell biology, and biomedicine with an aim to develop functional substitutes or scaffolds to support injured or damaged tissue regeneration [5]. Over the past decades, researchers have utilized cells, biomaterials, and other biomolecules to create numerous types of functional scaffolds for restoring or replacing the damaged tissues [6]. Scaffolds are three-dimensional (3D) porous structures that contain essential characteristics that support and guide the regeneration of targeted tissues [7]. To achieve the required functionality, the scaffolds must 1) be porous structures that allow for cell growth and ensure the diffusion of nutrients and metabolic wastes to and from the cells; 2) be biocompatible, maintain and facilitate cell functionality, and match the growth of cells and tissues; 3) have suitable chemical and biological properties for cell attachment, proliferation, migration, differentiation, and other cellular functions; and 4)

have sufficient mechanical strength to support structural integrity. Depending on specific applications, more functional requirements may be imposed upon scaffolds.

Encapsulating cells within scaffolds during fabrication (or scaffold biofabrication) has emerged recently to fulfill the above functions. Different from seeding cells on the scaffolds, scaffold biofabrication allows for production of scaffolds with spatial control of cells within, thereby creating scaffolds with highly-organized cell arrangement mimicking that of native tissues or organs [8]. To this end, the major challenges include the synthesis of biomaterials that are suitable for cell encapsulation and scaffold biofabrication from cell-encapsulated biomaterials.

1.2 Biomaterials for cell encapsulation

Hydrogel materials are generally required for cell encapsulation. Hydrogels are 3D polymeric structures that contain large amounts of water trapped by large numbers of linked polymer chains [9]. This ability to retain a high water content makes hydrogels compatible with cell encapsulation and delivery, as cells can stay between the polymer chains inside hydrogels [10]. Hydrogels are predominantly classified as either natural or synthetic biomaterials. Natural hydrogels are typically derived from organisms, and they generally support good cellular functionality. Alginate, a naturally derived polysaccharide extracted from seaweed, is an extensively used hydrogel for building scaffolds for cell encapsulation and delivery due to its ability to maintain cell viability, and convenient gelation process achieved by crosslinking with calcium ions under mild physiological conditions [11]. However, it is noted that alginate hydrogel has limited capability to provide cues for cell attachment, which significantly reduce other cellular functions of encapsulated cells. To address this deficiency, the most common method of alteration is to add proteins and peptides like laminin, fibronectin, or RGD (Arg-Gly-Asp) peptides into alginate prior to its gelation. With sufficient cell-binding sites provided by supplements with stable connections to alginate, outcomes such as cellular attachment and proliferation can be greatly improved.

In addition to the supplement proteins, to develop a functional scaffold that gives conductive environments for cells, some of the natural characteristics of the targeted tissues can be designed into the scaffold [12]. Among these characteristics, the mechanical

property of alginate hydrogel scaffold is important because the interactions of encapsulated cells with the scaffold can be influenced by the mechanical cues [13, 14]. These cues that cells experience include the resistance from alginate itself and the applied external forces to the hydrogel scaffold during scaffold handling or implantation. The resistance due to the hydrogel stiffness is the most common mechanical cue that change the fate of cells, as cells respond differently based on the stiffness of hydrogel, therefore the performance of cells can be regulated and improved if a mechanically-favourable environment is provided [15]. By changing the concentrations of alginate, the mechanical stiffness after crosslinking can be tuned. By measuring cell performance in culture following scaffold fabrication, the alginate concentrations favoured by cells can be identified, which can then be selected as the hydrogel concentration for scaffold biofabrication.

1.3 Extrusion-based bioprinting and bioprinting process-induced cell damage

Fabrication of scaffolds is one of the essential step towards the success in tissue engineering as it can decide the properties of scaffolds, including structural architecture, mechanical stability, and biocompatibility [16]. Conventional fabricating techniques, such as solvent-casting, gas-leaching, gas foaming, phase separation, and melt modeling, often rely on prefabricating a solid framework [17]. These techniques normally require extreme processing conditions for scaffold fabrication (e.g., high temperature, non-neutral pH, chemical or biological toxicity, etc.), affecting the ability to manipulate biological components such as living cells in the process, and therefore demanding post-fabrication cell seeding, which is inefficient. In addition, such methods normally result in disorganized and random fabrication of scaffold in structures and cell seeding that cannot be designed and repeated. All of these mentioned issues negatively influence the functions of scaffolds in their interacting with cells and tissue for tissue regeneration [17]. With the advancements in biofabrication techniques, such as 3D bioprinting technique, these major limitations of traditional techniques can be significantly alleviated, particularly for fabricating scaffolds with encapsulated cells.

Three-dimensional bioprinting techniques are the most promising methods because of the ability to deposit biomaterials, cells, and other biological components in a controllable, layer-by-layer pattern for fabricating scaffolds [18]. Among developed

bioprinting techniques, extrusion-based bioprinting (often referred to simply as bioprinting) works by dispensing biomaterials, components, and living cells to form continuous strands or fibers through a computer-controlled, automated fluid-dispensing head [8]. During the process of printing loaded materials in a fluid state are extruded through a small-bore needle and deposited in a location in a defined structure based on a computer model. A pneumatic extruding system, which utilizes pressurized air to drive the solution, has been extensively utilized in fluid-dispensing systems. By adopting extrusion-based bioprinting techniques, the fabrication of cell-encapsulated scaffolds using hydrogels and cells with desired cell distribution, reproducible and customized architecture can be facilitated.

As previously mentioned, the hydrogel-cell suspension can be loaded and then dispensed through a needle by the applied air pressure to build 3D scaffolds with encapsulated cells. In this process, the movement of the hydrogel and the cells contained therein through the needle can induce sustained shear and extensional stresses on the cells, which can elicit the deformation of cells and thus may breach the cell membranes [19]. This failure of the cell membrane leads to cellular dysfunction and damage, thereby reducing the viability of the cells [20]. Thus, knowledge regarding the stresses that influence the bioprinting-induced cell damage is important, and it can be used to guide the design of the printing process to maximize the preservation of cell viability and function. The shear stress that cells experience during bioprinting, which mainly occurs as cells are driven through the narrow needle tip, is considered to be one of the major factors that causes cell damage [21]. To investigate this effect, a specified shear stress should be provided, and the resulting damage to the cells subjected to this shear stress should be examined. Using a plate-and-cone rheometer can provide uniform and controllable shear stress on cells when the suspension is sheared. By setting the rheometer parameters, the resulting amount of cell damage associated with the level of shear stress, shearing time (or the exposure time), and cell density can be determined. Thus, a relationship between cell damage and shear stress can be built and then used to investigate cell damage in the bioprinting process. It is also worth noting that cell types from different tissue origins would respond differently to stresses. As such, evaluating cell damage using various cell types under shearing is necessary for understanding of the control of the bioprinting process to maintain high cell viability.

Besides the effects on cells due to shear stress, evidence demonstrates that the extensional stress that cells experience during the bioprinting process can also introduce cell damage and thus influence their viability after bioprinting [22]. Extensional stress is generated due to the abrupt velocity change as the cell suspension is driven through the geometrically-contracted region of the needle. Compared to shear stress, extensional stress may lead to more acute cell damage [23, 24]. Therefore, considering extensional stress is important for establishing a relationship between cell damage and the bioprinting process, however, this has rarely been taken into account. Whereas the cell damage caused by shear stress can be investigated using a rheometer, investigating cell damage introduced by extensional stress has proved challenging due to the difficulty in producing a pure extensional flow with cell suspensions to evaluate. To address this issue, a novel method should be developed by considering the cell damage in bioprinting as an aggregation of both shear and extensional stress-induced cell damage and extrapolating from there. As cell damage attributed to shear stress in bioprinting can be determined from the established relationship using the rheometer, and the resulting percent damage of cells in bioprinting can be measured, an accurate approximation of cell damage due to extensional stress can be obtained, and then the relationship between cell damage and extensional stress can be built. With the achieved relationship, the overall representation of the cell damage introduced by the bioprinting process can be given. It has also been noticed that cell damage can reduce the viability of cells in a short period after bioprinting; however, the influence of the bioprinting process on the functionality of cells, such as cell proliferation, after a longer period has not been well documented. To maintain high viability of cells and biological functions of a scaffold, the investigation of cell performance in a long-culture period after bioprinting is important.

1.4 Bioprinting of scaffold with encapsulated cells

In order to produce a scaffold that maintains the expected cell functionality and is also mechanically stable, with a structure that has fully interconnected porosity, a bioprinting method which considers and controls the parameters of the bioprinting processing conditions needs to be investigated and developed [25]. From the aforementioned investigations on the influences of hydrogel properties and the bioprinting

process on cell functionality, hydrogels with processing conditions that are cytocompatible need to be further studied for use in scaffold fabrication. One of the major challenges of using hydrogels for scaffold bioprinting is their mechanical printability, which refers to the ability to be dispensed into an integrated architecture with sufficient mechanical stability. To improve the printability of hydrogels, increasing the of viscosity of hydrogels by tuning the concentration of hydrogels is normally used. However, using a higher concentration also affects the functionality of cells due to the stiffer substrate that forms after hydrogel gelation [26]. Therefore, investigations on both hydrogel solution viscosity and the related cell performances within the gelled hydrogels is of importance for a hydrogel-based bioprinting. Printability of hydrogels is also heavily determined by the crosslinking condition [27]. Bioprinting with submerged crosslinking, whereby the hydrogel solution is deposited and gelled in a crosslinking medium, is one of the promoted method to alleviate the printability problem when relatively low viscosity hydrogel solutions are printed. This technique favours the formation of scaffolds because the medium prevents the vertical collapse due to the buoyancy provided by the medium. However, this method is only suitable when the appropriate amount of crosslinking agent is used, otherwise the buoyancy would have negative effect on scaffold stacking by either not preventing collapse due to insufficient concentration and thus reduce buoyancy, or preventing adherence of the subsequent layers due to excessive concentration and buoyancy. Thus, the crosslinking process in scaffold bioprinting should also be considered and adjusted. Additionally, the bioprinting process parameters, including the dispensing pressure and the dispensing head speed, not only affect the viability and functionality of cells, but also predicts the integrity of the scaffold by influencing the size and continuity of the scaffold strands. By tuning and optimizing all the mentioned processing conditions in the bioprinting process, a structurally-integrated and cytocompatible scaffold can be produced, which can be verified by long-term evaluation of the structure and cellular activities *in vitro*.

1.5 Research objectives

This research aims to investigate the influences of hydrogel properties and the bioprinting process on cell viability and functionality, and on this basis, develop

bioprinting processes to produce tissue scaffolds with encapsulated living cells for tissue engineering applications. The specific objectives of this thesis are to:

- Investigate the influence of hydrogel properties on the performances of encapsulated cells within scaffolds, including cell attachment, viability, proliferation, and cellular protein expression. Alginate and Schwann cells, as examples, are used for examination.
- Examine the cell damage to Schwann cells, fibroblasts, and myoblasts under shearing, and thus relate cell damage to shear stress, exposure time, cell density, and cell type. On this basis, the influence of cell damage on cell proliferation is further studied.
- Develop methods to assess the bioprinting process-induced cell damage due to both shear and extensional stresses. On this basis, models to characterize cell damage related to these stresses are established.
- Develop 3D bioprinting processes to fabricate hydrogel-based Schwann cell-encapsulated scaffold with desired structural integrity and cell functionality.

1.6 Organization of this thesis

This thesis includes seven chapters, which are this chapter of introduction, five chapters adapted from manuscripts, and a chapter on conclusions and areas of future study.

Chapter 2 presents a review on various extrusion-based bioprinting processes and associated methods developed for tissue scaffold biofabrication. The working principles of extrusion-based bioprinting are explained and achievements in cell-encapsulated scaffold fabrication are described. Advanced extrusion-based bioprinting strategies that have been developed for scaffold biofabrication are subsequently presented. Recommendations for future research to overcome the limitations identified from current extrusion-based bioprinting processes are also provided.

Chapter 3 investigates the influence of the properties of hydrogel substrates on the viability, proliferation, morphology, and protein expression of Schwann cells as a prelude for bioprinting tissue scaffolds for nerve tissue engineering. Schwann cells were integrated within alginate-based hydrogels for culture, and their morphology and viability were analyzed when the hydrogels were supplemented with the cell adhesion-enhanced

materials that included fibronectin, poly-l-lysine (PLL), and RGD peptide. After comparing the performances of cells for 7 days, the RGD-modified alginate hydrogels with different levels of stiffness were prepared by varying alginate concentrations, and the influence of the mechanical properties of alginate on the performance of encapsulated cells was investigated.

Chapter 4 presents a study on the flow behavior of alginate/cell suspensions and cell damage under shearing conditions. Schwann cells, fibroblasts, and myoblasts were selected and respectively mixed with alginate solutions for evaluation. Experiments to examine flow behavior were conducted using the prepared alginate solutions of varying concentrations, cell types, and cell densities. Experiments aimed at examining the effects of shear stress on cell damage were then carried out, with the percent cell damage measured and quantified as a function of shear stress, exposure time, and cell density. Cells from both sheared and non-sheared suspensions were also cultured, and their ability to recover from the injured situation and proliferate over 48 h were examined.

Chapter 5 investigates the bioprinting process-induced cell damage by considering both shear and extensional stresses. Because studying cell damage caused by extensional stress has proved challenging due to the difficulty in producing a pure extensional flow with cell suspension, a novel method is developed to determine cell damage models, or laws. Since cell damage in the bioprinting process is the result of both shear and extensional stress, experiments were conducted in which living cells integrated in alginate solutions were dispensed and the resulting percent cell damage was measured. Since percent cell damage attributed by shear stress can be determined experimentally and used to build a shear stress-based cell damage law, cell damage due to extensional stress in bioprinting can be analyzed and extensional stress-based cell damage law can be established. The degree of cell damage within 6 h after bioprinting, as well as the viability and proliferation of cells after 24-to-72 h were also evaluated, the results of which could be used to understand the influence of cell damage on the long-term preservation of biological functions in produced scaffolds.

Chapter 6 presents the development of bioprinting processes to fabricate Schwann cell-encapsulated scaffolds using cell-hydrogel suspensions comprised of alginate, fibrin, hyaluronic acid (HA), and RGD peptide. The influence of fibrinogen with varying

concentrations on the properties of formed hydrogels were examined. With correlated Schwann cell morphological spreading inside hydrogels, suitable hydrogel compositions were identified for scaffold bioprinting. The flow behavior of identified hydrogel solutions was evaluated, and on this basis, processing parameters for 3D bioprinting, including the dispending pressure, dispensing head speed, and concentrations of crosslinkers, were investigated and identified so as to fabricate scaffolds with structural integrity and improved cellular performance.

Finally, chapter 7 concludes the results drawn from this research, followed by recommendations for possible research in the future.

1.7 Contributions of the primary investigator

Contributions of all authors are greatly appreciated and acknowledged as manuscripts involved in this thesis are co-authored. However, it is the mutual understanding that Liqun Ning, as the first author, is the primary investigator of these research works.

1.8 References

[1] Robinson LR. Traumatic injury to peripheral nerves. *Muscle Nerve*. 2000 23 863-873.

[2] Struzyna LA, Katiyar K, Cullen DK. Living scaffolds for neuroregeneration. *Curr Opin Solid State Mater Sci.* 2014 18 308-318.

[3] Pfister BJ, Gordon T, Loverde JR, et al. Biomedical engineering strategies for peripheral nerve repair: surgical applications, state of the art, and future challenges. *Crit Rev Biomed Eng*. 2011 39 81-124

[4] Deumens R, Bozkurt A, Meek MF, et al. Repairing injured peripheral nerves: bridging the gap. *Prog Neurobiol*. 2010 92 245-276.

[5] Langer R, Vacanti JP. Tissue engineering. *Science*. 1993 260 920-926.

[6] Griffith LG, Naughton G. Tissue engineering-current challenges and expanding opportunities. *Science*. 2002 295 1009-1014.

[7] Hutmacher DW. Scaffold design and fabrication technologies for engineering tissues—state of the art and future perspectives. *J Biomater Sci Polym Ed*. 2001 12 107-124.

[8] Ning L, Chen X. A brief review of extrusion-based tissue scaffold bio-printing. *Biotechnol J*. 2017 12 1600671.

[9] Drury JL, Mooney DJ. Hydrogels for tissue engineering: scaffold design variables and applications. *Biomaterials*. 2003 24 4337-4351.

[10] Ladet S, David L, Domard A. Multi-membrane hydrogels. *Nature*. 2008 452 76-79.

[11] Draget KI, Skjåk-Bræk G, Smidsrød O. Alginate based new materials. *Int J Biol Macromol*. 1997 21 47-55.

[12] Klein TJ, Malda J, Sah RL, et al. Tissue engineering of articular cartilage with biomimetic zones. *Tissue Eng Part B Reviews*. 2009 15 143-157.

[13] Gu Y, Ji Y, Zhao Y, et al. The influence of substrate stiffness on the behavior and functions of Schwann cells in culture. *Biomaterials*. 2012 33 6672-6681.

[14] Even-Ram S, Artym V, Yamada KM. Matrix control of stem cell fate. *Cell*. 2006 126 645-647.

[15] Discher DE, Janmey P, Wang Yl. Tissue cells feel and respond to the stiffness of their substrate. *Science*. 2005 310 1139-1143.

[16] Ozbolat IT, Hospodiuk M. Current advances and future perspectives in extrusion-based bioprinting. *Biomaterials*. 2016 76 321-343.

[17] Zhu N, Chen X. Biofabrication of tissue scaffolds. *Advances in biomaterials science and biomedical applications*. InTech, 2013.

[18] Mironov V, Reis N, Derby B. Review: bioprinting: a beginning. *Tissue Eng*. 2006 12 631-634.

[19] Gupta R, Truong L, Bear D, et al. Shear stress alters the expression of myelin-associated glycoprotein (MAG) and myelin basic protein (MBP) in Schwann cells. *J Orth Res*. 2005 23 1232-1239.

[20] Smith CM, Stone AL, Parkhill RL, et al. Three-dimensional bioassembly tool for generating viable tissue-engineered constructs. *Tissue Eng*. 2004 10 1566-1576.

[21] Chang R, Nam J, Sun W. Effects of dispensing pressure and nozzle diameter on cell survival from solid freeform fabrication-based direct cell writing. *Tissue Eng Part A*. 2008 14 41-48.

[22] Bae YB, Jang HK, Shin TH, et al. Microfluidic assessment of mechanical cell damage by extensional stress. *Lab Chip*. 2016 16 96-103.

[23] Aguado BA, Mulyasasmita W, Su J, et al. Improving viability of stem cells during syringe needle flow through the design of hydrogel cell carriers. *Tissue Eng Part A*. 2011 18 806-815.

[24] Down LA, Papavassiliou DV, Edgar A. Significance of extensional stresses to red blood cell lysis in a shearing flow. *Ann Biomed Eng*. 2011 39 1632-1642.

[25] Murphy SV, Atala A. 3D bioprinting of tissues and organs. *Nat Biotechnol*. 2014 32 773-785.

[26] Little CJ, Bawolin NK, Chen X. Mechanical properties of natural cartilage and tissue-engineered constructs. *Tissue Eng Part B Reviews*. 2011 17 213-227.

[27] Hennink W, Van Nostrum C. Novel crosslinking methods to design hydrogels. *Adv Drug Del Rev*. 2012 64 223-236.

CHAPTER 2

A Brief Review of Extrusion Based Tissue Scaffold Bioprinting

This chapter has been published as "Liqun Ning and Xiongbiao Chen, A Brief Review of Extrusion Based Tissue Scaffold bioprinting. *Biotechnology Journal*. 2017, 12, 1600671." According to the Copyright Agreement, "the authors retain the right to include the journal article, in full or in part, in a thesis or dissertation".

2.1 Abstract

Extrusion based bioprinting has great potential as a technique for manipulating biomaterials and living cells to create 3D scaffolds for damaged tissue repair and function restoration. Over the last two decades, advances in both engineering techniques and life sciences have evolved extrusion based bioprinting from a simple technique to one able to create diverse tissue scaffolds from a wide range of biomaterials and cell types. However, the complexities associated with synthesis of materials for bioprinting and manipulation of multiple materials and cells in bioprinting pose many challenges for scaffold fabrication. This chapter presents an overview of extrusion based bioprinting for scaffold fabrication, focusing on the prior-printing considerations (such as scaffold design and materials/cell synthesis), working principles, comparison to other techniques, and to-date achievements. This chapter also briefly reviews the recent development of strategies with regard to hydrogel synthesis, multi-materials/cells manipulation, and process induced cell damage in extrusion based bioprinting. The key issues and challenges for extrusion based bioprinting are also identified and discussed along with recommendations for future works, aimed at developing novel biomaterials and bioprinting systems, creating patterned vascular networks within scaffolds, and preserving the cell viability and functions in scaffold bioprinting. The address of these challenges will significantly enhance the capability of extrusion based bioprinting.

2.2 Introduction

Tissue engineering is an interdisciplinary field that combines knowledge and technologies in engineering, materials science, cell biology, and biomedicine to improve

or replace natural or biological tissues [1]. Notably, natural tissues consist of highly-organized cells and cellular components that perform specific functions. Over the past three decades, researchers have utilized cells, biomaterials growth factors, and other supporting components to create functional constructs for facilitating the regeneration of natural tissues following injury or disease [2-5]. A particularly promising tissue engineering approach involves the development of 'tissue scaffolds', which are 3D constructs comprised of biomaterials and cells to support and guide the regeneration of targeted tissues by facilitating the cell differentiation, migration, and proliferation [6, 7]. Tissue scaffolds are porous structures with interconnected architectures and used to facilitate the metabolism of cells by mimicking the cellular environment, meanwhile providing appropriate mechanical support to maintain the stability of structures both in vitro and in vivo [8]. Tissue scaffolds should also be degradable with a rate that, ideally, matches cell and tissue regeneration.

Traditionally, scaffolds are fabricated from biomaterials and subsequently seeded with cells. With the advance of bioprinting techniques, living cells can be incorporated in bioprinting scaffolds with the structure of highly-organized cells. In the bioprinting process, biomaterials, living cells, and other relevant biological molecules
are deposited in a layer-by-layer pattern to form spatially controlled structures [9, 10]. Among the bioprinting approaches developed to date, extrusion based bioprinting, which is based on pneumatic or mechanical mechanisms to extrude or dispense materials and cells through nozzles, has been widely used in the development of tissue scaffolds [11–14]. Using the extrusion based bioprinting techniques, tissue scaffolds can be fabricated with biological and mechanical properties appropriated for the restoration of damaged-tissue functions. To this end, one big challenge is to manipulate multiple materials and cell types that can reproduce the complex architecture and composition of natural tissue, in order to facilitate the restoration of functions of damaged tissues.

The present chapter reviews various extrusion based bioprinting processes as well as associated strategies developed for creating tissue scaffolds. An overview of extrusion based bioprinting for tissue scaffold fabrication is presented and the advanced strategies that have been developed for incorporating cells in scaffolds are discussed.

Recommendations for future research to overcome the limitations and/or issues identified from current extrusion based bioprinting processes are also provided.

2.3 Overview of extrusion based tissue scaffold bioprinting

A typical tissue scaffold bioprinting process involves several key steps, as shown in Figure 2.1. Structural design is the first step in producing a tissue scaffold that can faithfully represent the composition and organization of the tissue of interest. Therefore, a comprehensive understanding of the targeted tissue structure is necessary. After the design, synthesis of cells and biomaterials that can appropriately support the desired cellular and extracellular functions of the tissue is the next step. The selected materials must be not only compatible with the functions of selected cells and targeted tissues but also with the bioprinting process [15]. The extrusion based bioprinting method is then applied based on the structural design and materials/cells selected to produce tissue scaffolds, which are then cultured in vitro or implanted into the localized tissue area for in vivo applications. If adverse performance or undesired effects are observed, the outcomes from both in vitro and in vivo applications can be evaluated and the results used to modify the bioprinting process to improve the fabrication of tissue scaffolds [16].

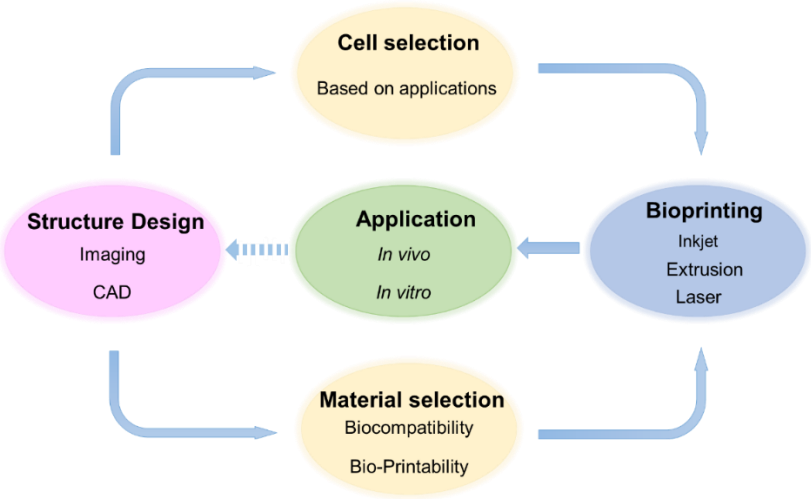

Figure 2. 1 Schematic of tissue scaffold bioprinting process

2.3.1 Considerations before tissue scaffold bioprinting

A comprehensive understanding of the composition and organization of the targeted tissue is important for tissue scaffold design, and is the first step for tissue scaffold bioprinting. Generally, the combination of medical imaging and computer-aided design (CAD) techniques is used for tissue scaffold design. Medical imaging techniques such as computed tomography (CT) and magnetic resonance imaging (MRI) are the most frequently adopted methods to detect tissue components, as they are able to provide information on tissue composition at the cellular, tissue, and organ levels [17, 18]. Once imaging data have been acquired, 3D models of the tissue components can be built with the help of CAD techniques, which are used to reproduce three-dimensional views that reflect the anatomical structures derived from the imaging modalities [19, 20]. The CAD models are then recognized by the bioprinting system and used to produce tissue scaffolds for the repair of tissues that are defective due to disease or injury. Therefore, ensuring adequate resolution of the imaging techniques to precisely represent the structural of tissues as well as the accuracy of CAD techniques to rebuild the tissue components are important for producing tissue scaffolds with expected organization and structure.

Materials play a central role in tissue scaffold bioprinting by providing the physical support and structural interface necessary for interactions with cells and tissues. Before the bioprinting process, understanding the performance of materials, predominantly based on their intrinsic properties, is necessary for material synthesis. The first and the most important property is biocompatibility, which refers to the material characteristic of passively allowing or actively producing desirable effects on cells and tissues [21]. In tissue scaffold bioprinting, a biocompatible material is expected to have positive contributions to the biological functions of cells and tissue components, which include the support of cellular activity (e.g. cell proliferation, migration, and differentiation) without leading to cell functional damage or death, the facilitation of molecular signaling, and the protection of cells from the immune system. In addition, a biocompatible material should be suitable for supporting long-term transplantation. This requires the degradation rate of the material to be controllable so as to allow the scaffold to be gradually replaced by the extracellular matrix (ECM) proteins secreted from the associated cells. Thus, a candidate biocompatible material should have a degradation rate that matches the ECM secretion rate and produce

only non-toxic degradation byproducts that can be metabolized or rapidly cleared from the body. The other crucial property to be considered during material synthesis is bioprintability, which indicates the materials can be deposited in a controllable pattern and have suitable stability after deposition to avoid structural collapse [22]. Particularly for extrusion based bioprinting, a bioprintable material should have an appropriate fluidic viscosity so it can be deposited in a controlled manner as well as suitable crosslinking mechanisms that allow solidification of the designed structure with appropriate mechanical properties to ensure structural stability [23]. For tissue scaffold bioprinting, cells are mixed or encapsulated inside the material solutions, which requires the adopted material to be permeable, non-toxic, pH neutral, able to provide an aqueous environment for cell metabolism, and able to be processed under mild conditions to maintain cell viability. Before loading materials into the bioprinter, proper selection by considering both biocompatibility and bioprintability, including cell-material interactions, material degradation, material viscosity, crosslinking mechanism, and mechanical properties, is necessary to achieve scaffolds with desired functions.

Hydrogel polymers are one of the biomaterial types extensively used in extrusion based bioprinting for tissue scaffold fabrication due to their inherent ability to provide a compatible, aqueous environment for mixed cells both in and after the printing process. Hydrogel materials can be crosslinked to form a polymeric structure that contains a large amount of water and possesses similar properties to tissue ECM [24, 25]. Generally, hydrogel polymers are predominantly classified as either natural polymers or synthetic polymers. Natural polymers such as polysaccharides (e.g. alginate, chitosan, agarose) and protein-based polymers (e.g. collagen, gelatin, fibrin, elastin, resilin), have been widely used in tissue scaffold bioprinting. Polysaccharides normally have crosslinking rates that ensure bioprintability, but are limited with respect to cell attachment due to the lack of cell adhesion sites [26-28]. Protein-based polymers are biocompatible for cell attachment and functions, but have relatively slow crosslinking rates and weak mechanical stabilities [29]. Synthetic polymers such as poly(ethylene glycol) (PEG) and poly(ethylene oxide) (PEO) have more uniform and tailorable properties compared to natural hydrogels, but lack the biocompatibility to facilitate cellular functions; toxic degradation byproducts may also limit their utilization if they are used independently in tissue scaffold bioprinting [30].

Therefore, selecting appropriate material types before the bioprinting process is important and can determine the performance of the printed tissue scaffolds.

Mixing cells into the material solution and then loading the solution into the bioprinter is the last step before tissue scaffold bioprinting. One advantage of extrusion based bioprinting for tissue scaffold fabrication is that it allows a wide range of cell densities to be mixed into the material solutions, which can reach physiological density (10^8-10^9 cells/mL) in tissues. This greatly reduces the preparation period for cell proliferation and maturation before scaffold implantation [21].

2.3.2 Working principles of extrusion based tissue scaffold bioprinting

Extrusion based tissue scaffold bioprinting refers to a technique that is capable of depositing filaments, fibers, or droplets of biomaterials and cells to form tissue scaffolds in a controllable layer-by-layer pattern [31]. An extrusion based bioprinting system combines a fluid dispensing head and an automated robotic system [32]. During bioprinting, the dispensing head is moved along X and Y axes controlled by the robotic system to deposit biomaterial/cell solutions onto a stage, and moved up or down along the Z axis (or the stage is controlled while the head is fixed) to deposit different layers and form the scaffolds as directed by the CAD models. Based on deposition mechanisms, extrusion based bioprinting methods can be classified into three categories: pneumatic-, piston-, and screw-based bioprinting (Figure 2.2). Pneumatic-based bioprinting is a simple and extensively used method that utilizes compressed air to drive biomaterials/cells from a syringe and nozzle at a controllable volume flow rate (Figure 2.2A). The accuracy of material deposition is heavily dependent on the flow properties of the material solution and can be significantly affected by the solution viscosity [33]. In piston- or screw-based bioprinting systems, biomaterial cell solutions are mechanically pushed by a linear moving piston or a rotating screw-driven configuration (Figure 2.2B and 2.2C) [34]. Both printing mechanisms can provide large deposition forces for control over solution volumes. Thus, a larger pressure drop from the inlet of the syringe to the outlet of the nozzle is of benefit of printing higher viscosity suspensions. Mechanically driven mechanisms often require relatively complex components, and the large driving forces may induce the rupture of cell membranes in the dispensing process [35].

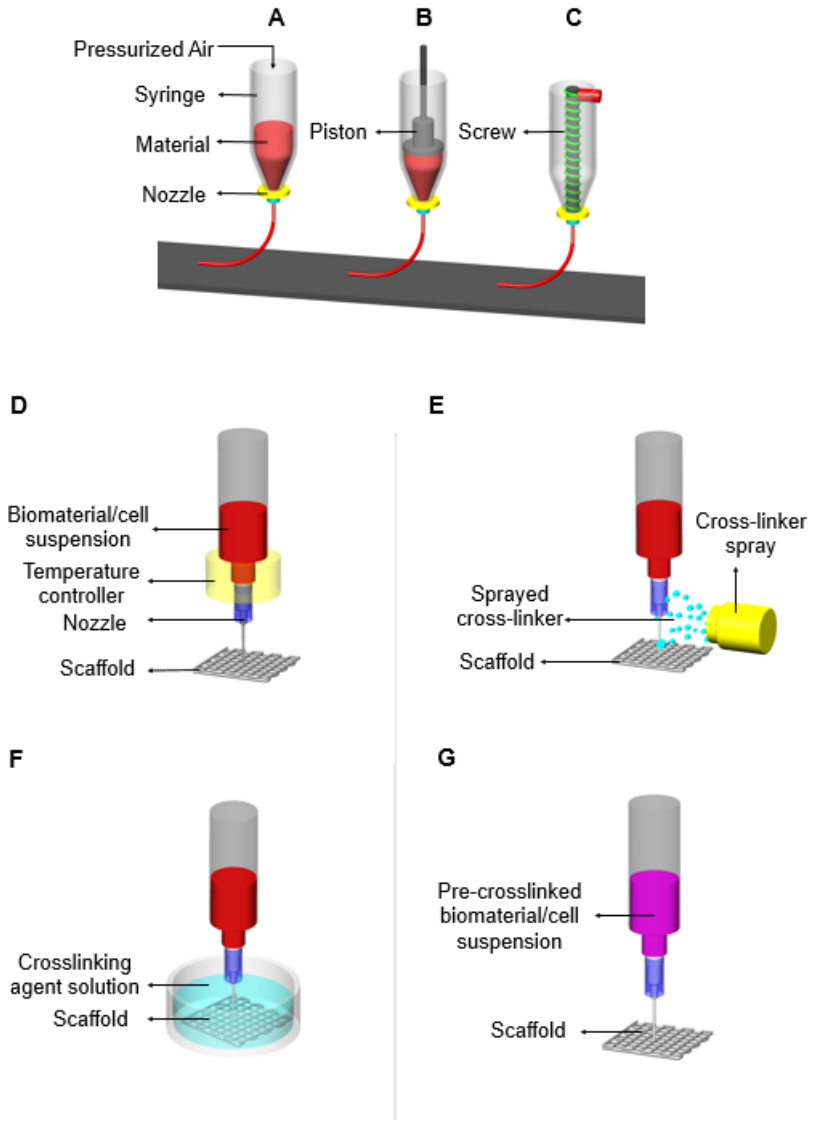

Figure 2. 2 Schematic of extrusion based bioprinting methods and configurations for hydrogel scaffold bioprinting. A, pressurized air; B, moved piston; C, rotated screw; D, thermal based bioprinting; E, spray based bioprinting; F, bioplotting; and G pre-crosslinked bioprinting

Extrusion based bioprinting is compatible with a wide range of fluid viscosities. Higher viscosity materials are more suitable in terms of providing structural support for the tissue scaffolds while lower viscosity materials are more appropriate for cellular bioactivities [36, 37]. Therefore, synthesis of materials with expected flow behavior must be carefully considered to ensure both mechanical stability of structures of tissue scaffolds and cell functionalities [38]. Increasing the diameter of dispensed filaments and fibers or

reducing the porosity by controlling the bioprinting process or the nozzle diameter can increase the mechanical stability of structures, but thicker filaments and lower porosities reduce cellular diffusion and thus prevent the exchange of nutrients and metabolic wastes [39]. On the other hand, reducing the diameter of filaments can eliminate diffusion barriers but weakens mechanical properties. Because different cell types require specific environments, adjusting the mechanical properties of scaffolds by regulating material types, material viscosities, or the bioprinting process is necessary to meet the requirements of structural stability and cellular functionality [40, 41].

Various crosslinking methods, including physical crosslinking (e.g. via temperature) and chemical crosslinking (e.g. via ionic or covalent bonding), have been developed for various hydrogels in bioprinting [42]. Thermal crosslinked hydrogel polymers (e.g. collagen, gelatin) are fluid within a certain temperature range but crosslink into hydrogels at a given temperature (Figure 2.2D) [43]. This process needs no extra crosslinking agent to trigger hydrogel solidification, but maintaining the mechanical stability of the printed structure can be relatively difficult due to the material properties. Ionic or covalent crosslinking results in chemical bonds between hydrogel polymers and crosslinking agents upon mixing [44-46]. Therefore, one method developed to promote the encounter is to atomize crosslinking agents and spray them onto the bioprinted materials (Figure 2.2E) [47]. Challenges for the atomization approach include control of the distribution of atomized agents on the materials as well as incomplete crosslinking due to a lack of crosslinking agent. Maintaining the stability of bioprinted structures becomes more challenging if low viscosity material solutions are applied [16]. A method to deposit material solutions into the related crosslinking solutions has been developed and is capable of addressing the issues faced by atomization crosslinking. As this method provides sufficient crosslinking agents in solution, the crosslinking process can be rapidly and uniformly completed. This method is also known as bioplotting (Figure 2.2F) [48]. Bioplotting is suitable for material types that have a fast crosslinking rate, as otherwise structural collapse is likely to occur due to the buoyancy of the crosslinking solution [49, 50]. Furthermore, if unmatched concentrations of material and crosslinking solutions are conjugated, the printed structures may float up or stack at the point of deposition and result in structural failure [50]. Pre-crosslinked materials are also used due to the regulated flow

properties of material solutions (Figure 2.2G) [51]. Controlled pre-crosslinking can significantly improve the viscosity of material flows, and thus ensure the bioprintability of the solutions. During pre-crosslinking, selecting the appropriate amount of crosslinking agent is crucial because too much may alter the flow properties of materials by inducing material phase change [52].

2.3.3 Comparison between extrusion based bioprinting and other bioprinting techniques

Bioprinting techniques besides extrusion based bioprinting have been used to produce tissue scaffolds, and, these techniques are generally classified as laser-based bioprinting (including stereolithography (SLA), two photon-polymerization (2PP), mask-assisted bioprinting) and inkjet-based bioprinting (including thermal inkjet and piezoelectric inkjet) based on their working principles (Table 2.1). Compared to these two bioprinting methods, extrusion based bioprinting has several advantages [53]. It is able to dispense a wide array of biomaterials and cells, including both native and synthetic hydrogel polymers, cell aggregates, and decellularized extracellular matrix, while other techniques are limited to bioprinting hydrogel polymers with suspended cells [54]. Depositing biomaterials with physiological cell density, which is a major challenge for other bioprinting techniques, is feasible with the extrusion based bioprinting method [55]. Due to its fast deposition speed, extrusion based bioprinting is also often used to produce large-scale scaffolds.

Table 2. 1 Comparison of three 3D bioprinting techniques

Techniques	Sub-classified systems	Principles of operation	Advantages	Disadvantages	References
Extrusion based bioprinting	3D bioprinting 3D bioplotting	Layer-by-layer deposition of material-cell suspensions onto a predefined location (without crosslinking solution)	Simple components and simple control; compatible with a wide range of materials; mild printing environment for cells; able to	Limited printing resolution; solidification rate requirements; tip clogging; cell number reduced in	[13, 59-64]

		Layer-by-layer deposition of material-cell suspensions onto a predefined location (with crosslinking solution)	produce large-scale scaffolds; possible to print high cell densities	large-scale printing	
Inkjet-based bioprinting	Thermal inkjet Piezoelectric inkjet	Layer-by-layer drop-based deposition of material-cell suspensions driven by pulses of pressure from electrical heating. Layer-by-layer drop-based deposition of material-cell suspensions driven by pulses of pressure from piezoelectric material.	Simple and affordable; fast deposition speed; relatively high printing resolution and precision	Low viscous solution required; probable cell damage induced by printing forces and temperature changes; difficult to achieve physiological cell densities	[12, 18, 39, 65, 66]
Laser-based bioprinting	SLA 2PP Mask-assisted	Photopolymerization in a reservoir by using a laser-based beam. 3D structures are formed by controlling the movement of light beam and platform. Photopolymerization using two photons that are absorbed by a photon initiator at the focal point of a laser-based beam. Use of a mask for photopolymerization to crosslink polymers and form designed	High bioprinting resolution and precise spatial control; no clogging problem; compatible with biomaterials with diverse viscosities	Fast gelation kinetics requirements; time-consuming for manipulation of multiple cell types; toxic photon initiators to cells	[27, 30, 56, 67-69]

		constructs by the mask.			

Despite the benefits, extrusion based bioprinting also has several disadvantages. It has limited bioprinting resolution (typically more than 100 μm) mainly due to the compromised consideration of the pressure required to drive a scaffold solution through the nozzle and the nozzle mechanical strength to bear such a pressure. Organizing deposition at the micro level is challenging compared to other bioprinting techniques (e.g. laser-based bioprinting can reach the highest resolution of 1 μm [56], and inkjet-based bioprinting produces droplets less than 50 μm in diameter [12]). The bioprintability of hydrogels is heavily dependent on the crosslinking speed in extrusion based bioprinting, and the utilization of slow crosslinking speed biomaterials can be restricted [57]. Preparing biomaterial/cell suspensions with appropriate flow properties is important for bioprintability and cell functions but is time-consuming, especially for depositing multiple types of biomaterials and cells [16]. Cell viability after dispensing has proven to be lower than inkjet-based bioprinting due to process-induced stresses in bioprinting that become worse if higher pressures or smaller diameter nozzles are used [58]. Using extrusion- based bioprinting for large-scale construct fabrication may also have negative effects on living cells because they are exposed to a non-tissue culture environment for a long period. Nozzle clogging caused by biomaterial solidification is another problem in extrusion based bioprinting that is not found in nozzle-less techniques such as laser-based bioprinting; indeed, severe clogging can completely interrupt biomaterial deposition and therefore scaffold integrity.

2.3.4 Achievements using extrusion based bioprinting

Extrusion based bioprinting can produce tissue scaffolds using various cells types, including both primary cells and stem cells. Primary cell types, which are isolated from animals and humans and include osteocytes, chondrocytes, and keratinocytes, have already been used in tissue scaffolds to faithfully represent tissue components such as bones, cartilage, and skin [70-72]. Recently, the fabrication of lung analogues using alveolar epithelial type II cells and endothelial cells has demonstrated the feasibility of extrusion-base bioprinting for producing lung components [73]; the human air-blood barrier analogue

produced had a high cell viability and similar function to native lung analogues. Functional skeletal muscle scaffolds with different structures have been created by an extrusion based bioprinting technique using myoblast cells for muscle tissue regeneration [74]. Cells can be aligned in a spatial pattern within the constructs via bioprinting process control, with expected myogenic differentiation and myotube formation after a certain period in culture. Scaffolds with high viability and the expected function of hepatocytes have also been printed, indicating the potential of extrusion based bioprinting techniques for restoration of human liver function [75]. Artificial valve conduits built from smooth muscle cells (SMC) and aortic valve leaflet interstitial cells (VIC) have been produced and applied to replace traditional prosthetic substitutes for heart valve disease treatment [61]. The alpha-smooth muscle actin and vimentin secreted by the printed cells demonstrate the ability of extrusion based bioprinting to fabricate valve-like tissue constructs. Mechanisms of neuro regeneration after injury include various cues aimed at promoting axon growth [46], and printed tissue scaffolds with encapsulated aligned glial cells have been created to facilitate this procedure [76]. In many cases, isolating primary cells from living tissues is difficult or they are challenging to culture [77]. In such cases, stem cells are often used as a substitute for primary cells in tissue scaffold bioprinting. Stem cells can self-renew and differentiate into specific cell types when certain cues are provided. The extrusion based bioprinting technique has shown great potential for regulating and conducting stem cell growth and differentiation in many applications, such as those targeting brain tissue, gingival tissue, adipose tissue, and bone marrow tissue and [52, 64, 78, 79].

In addition to the ability of the extrusion based bioprinting method to manipulate diverse cell types, various printed structures such as beads, filaments, fibers, channels, sheets, rolls, grids, and porous 3D constructs that mimic the tissue components have been successfully printed at micro or macro levels. Among these structures, the formation of vasculature is a major challenge in tissue engineering. The function of vascularization is to supply oxygen, nutrients, and metabolites of cellular activities to ensure the long-term viability of cells and tissues. In extrusion based bioprinting, vessel-like permeable channels have been produced and used to facilitate vascularization with the expectation of forming vascular networks. Supporting cells such as endothelial cells are often deposited in vessel-like channels during bioprinting to initiate the formation of vasculatures and subsequently

support their stabilization and function, which can further facilitate the angiogenesis of vessel networks [80].

2.4 Advanced strategies for extrusion based 3D bioprinting

As noted above, the production of tissue scaffolds contains varying cells types, ECM components, and other functional materials in an organized pattern to mimic tissues using typical extrusion based bioprinting techniques is challenging [81]. New materials and bioprinting approaches to produce tissue scaffolds from multiple materials and cells types with high deposition resolution and expected biological

2.4.1 Strategies of hydrogel preparation for extrusion based tissue scaffold bioprinting

Satisfying the demands of biocompatibility and bioprintability in tissue scaffold bioprinting is difficult using a single hydrogel polymer. As such, mixing different materials can be undertaken to create more suitable hydrogel blends that may demonstrate synergistic properties. For example, adding proteins such as laminin or fibronectin to hydrogels such as alginate results in a large improvement in cell adhesion while maintaining the desired bioprintability; however, the major challenge of this method is avoiding the escape of materials in the long-term due to their weak connections [83]. The same limitation affects hydrogels mixed with nanoparticles (e.g. bio-glass and carbon tubes) [84, 85]. Using blended hydrogels can prevent the material from escaping because all of the materials can be solidified. In this application, hydrogel materials with rapid crosslinking are selected to support the bioprinting process and mechanical requirements of tissue scaffolds, while other hydrogels are used to ensure biocompatibility for cell functions [86]. Using blended hydrogels introduces the problem of discrepant biodegradation, which brings challenges with respect to structural replacement by cell-secreted ECM.

Modification of bioprintable hydrogels can also be undertaken to improve their biocompatibility. Materials such as proteins or peptides are normally permanently immobilized in the molecular chains of hydrogel polymers under controllable conditions, thus improving the interaction of hydrogels and cells [87]. Modification by proteins introduces the risk of inducing non-specific interactions with hydrogels, such as undefined

bonds due to protein complexes, and therefore the reaction process is relatively difficult to control [88]. This issue can be overcome by introducing modifications with peptides, which are specific sequences in proteins such as Arg-Gly-Asp-Ser (RGDS) derived from fibronectin and Tyr-Ile-Gly-Ser-Arg (YIGSR) and Ile-Lys-Val-Ala-Val (IKVAV) from laminin; this approach is widely used for improving cell attachment [26]. Peptides can activate particular groups of hydrogel chains to form covalent amide bonds and therefore a hydrogel with improved cell adhesion properties [89]. Meanwhile, peptides are normally costly, and the reactive environment of each chemical (e.g. pH value, temperature, concentration) must be carefully selected.

Hydrogels have also been modified using special materials and approaches to improve their bioprintability. Some hydrogels have good biocompatibility but poor bioprintability. For example, gelatin is an inexpensive, denatured collagen that retains natural cell binding sites [48]. Addition of methacrylate groups to the amine-containing side groups of gelatin results in the formation of gelatin methacrylate (GelMA), which is a photopolymerizable hydrogel that can be lightly crosslinked. Therefore, by controlling both the temperature and light (e.g. UV light), the stability of bioprinted GelMA scaffolds can be ensured [45, 62]. This method of modifying materials to be photopolymerizable has also been applied to other hydrogels with poor bioprintability, such as hyaluronic acid and PEG [30, 90], but requires the integration of a light generator into the bioprinting system.

2.4.2 Multi-material/cell manipulation in extrusion based bioprinting

Tissue scaffolds produced from multiple materials/cells are in high demand because they have the potential to faithfully represent the composition and organization of tissues components. The most straightforward method to build this type of scaffold is to deposit physically mixed materials/cells [91]. Obviously, the drawback of this method is that materials and cells can hardly be organized individually in the desired spatial pattern. Depositing cells and materials in a certain arrangement is challenging in typical extrusion based bioprinting, and the development of advanced techniques is required [54]. Extrusion based bioprinting systems with multiple dispensing heads make organizing the deposition of multiple materials/cells more feasible as they can be loaded and dispensed from separate heads (Figure 2.3A1) [92]. Multiple heads also extend the range of available material types,

allowing materials with a poor crosslinking rate to be adopted in tissue scaffold bioprinting because of the utilization of other bioprintable materials (such as polycaprolactone (PCL) and poly(lactic-co-glycolic acid) (PLGA)) that can provide mechanical support to those that solidify more slowly [60, 93]. Figure 2.3A1 shows that bioprinting systems are clearly limited with respect to simultaneously dispensing individual materials/cells from separate heads as only one head can be activated at a time; exchanging heads would reduce the printing efficacy and raise the risk of nozzle clogging when the head is inactive. Other multiple head bioprinting systems with simultaneously controllable dispensing functions have also been developed (Figure 2.3A2 and A3) [94, 95]. These systems allow materials/cells to be deposited individually and simultaneously by operating each dispensing head, which can greatly improve the printing efficiency and avoid nozzle clogging during printing.

The utilization of microfluidics in extrusion based bioprinting increases the feasibility of processing multiple materials to produce micro level blocks for tissue scaffold fabrication. Microfluidics is based on laminar flows in parallel using a multiplex technique to organize low-scale fluid volumes [51, 96]. Multiple materials can be used to form the parallel streams, and therefore special printed blocks such as multiple-phase filaments (containing several materials) and micro-channels can be produced [97]. In extrusion based bioprinting, two microfluidic methods including co-axial capillaries and lab-on-a-chip have been developed and can be adopted to create parallel flows between different material solutions. Co-axial capillary is a configuration featuring two or more capillaries connected in a co-axial form (Figure 2.3B1). When different material solutions are loaded and dispensed from the separate capillaries (e.g. outer and inner capillaries), they can coaxially flow inside the capillaries in parallel based on the laminar flow behavior [98]. The structures created are predominantly determined by the dispensed materials. For example, if two materials (e.g. PCL and collagen) are dispensed separately from outer and inner capillaries, a two-phase filament made by these two materials in a coaxial distribution can be achieved after solidification [71]. If a material is dispensed from the outer capillary while the associated crosslinking solution is dispensed from the inner capillary (e.g. alginate and calcium solutions), a hollow fiber can be produced [99]. In this case, the selected material must have rapid solidification speed to avoid the collapse of the hollow

channel. If the material is loaded into the inner capillary and the crosslinking solution is outside, a single-phase filament can be printed [100]. This method avoids the buoyancy issue faced by 3D bioplotting because the crosslinking reservoir can be omitted; the printed filament can be solidified inside the capillaries before being dispensed [96]. The sizes of printed filaments or hollow channels can range widely, from the millimeter- to micrometer-scale depending on the capillary diameter, and can be easily adjusted by regulating the dispensing pressures.

The morphologies of printed filaments or fibers from co-axial capillaries are limited to relatively simple structures such as core-shell-type or hollow shapes, and therefore lack the ability to represent tissue components with complex and highly organized cells [101]. Lab-on-a-chip is an alternative method that has been applied in extrusion based bioprinting to assist in the fabrication of tissue scaffold blocks with more complicated cross sections. Lab-on-a-chip is a device that integrates several tiny channels into one chip (Figure 2.3B2). These channels with various cross-sectional shapes (e.g. round, square) are normally carved using photolithography or electroplating at the micrometer to millimeter scale [102]. Therefore, micro fibers or filaments made from multiple materials with a controllable cross-sessional morphology can be achieved. Micro fibers made from multiple hydrogels have been successfully printed using lab-on-a-chip [103]. In this example, two material solutions are dispensed from separate inlets, and flow in parallel inside the gelation channel after they emerge from the focusing nozzle with a special cross-sectional shape. The multiple phase fiber is then gelled by the crosslinking solution flowing in the parallel channel dispensed from the other inlet. Because flows in the micro channel can be easily affected by capillary forces, surface roughness, and even chemical interactions, ensuring the printed fiber shape is a challenge with the lab-on-a-chip method. A full understanding of the lab-on-a-chip technique, including both its manufacturing requirements and utility for bioprinting process control, has not yet been achieved.

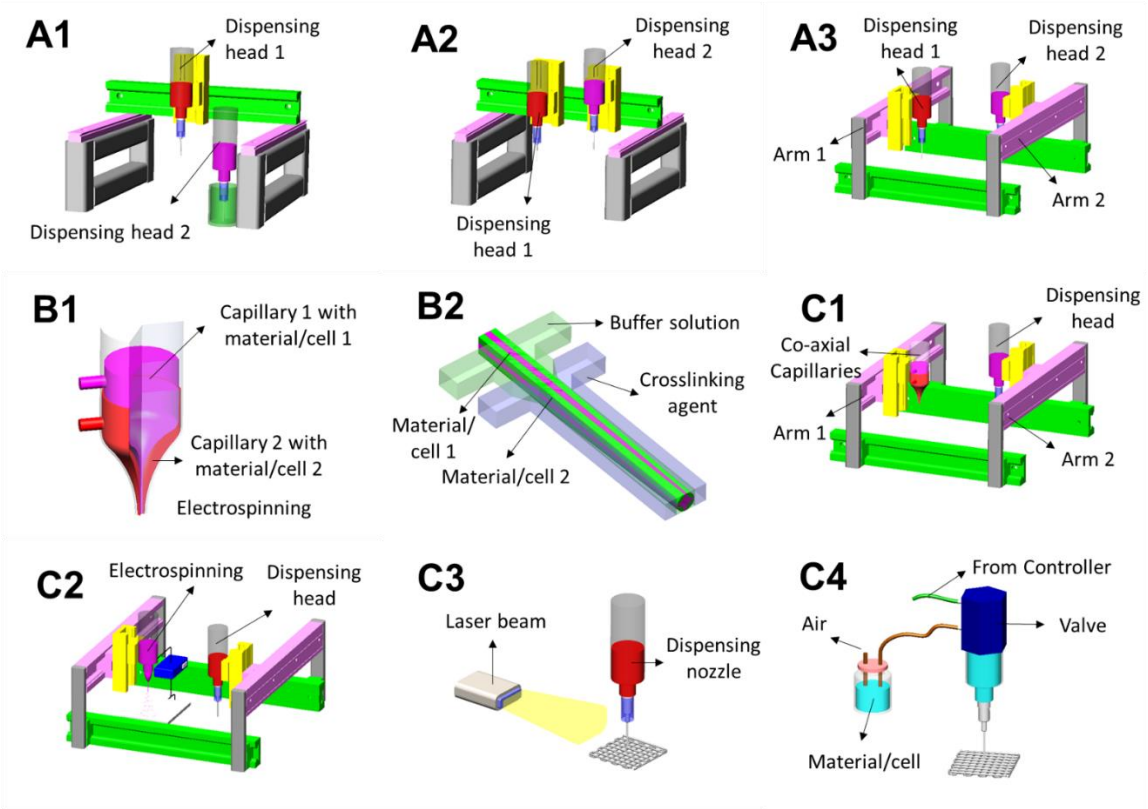

Figure 2. 3 Advanced extrusion based bioprinting approaches for multi-biomaterial/cell manipulation. A1, one-arm multi-nozzle bioprinting system with one activated dispensing head; A2, one-arm multi-nozzle bioprinting with multiple activated dispensing heads; A3, multi-arm/nozzle bioprinting with multiple activated dispensing heads; B1, coaxial capillaries; B2, lab-on-a-chip; C1, integration of multi-nozzle bioprinting and coaxial capillaries; C2, integration of bioprinting and electrospinning; C3, integration of bioprinting and laser beam; C4, integration of bioprinting and valves.

Integrating extrusion based bioprinting technique with other fabrication methods can be undertaken to bring together advantages from each approach while reducing their limitations. Table 2.2 summarizes such integration approaches. For example, one integration method is to combine multi-head bioprinting systems with microfluidics configurations (Figure 2.3C1). With the help of microfluidics in a multi-head dispensing system, microchannels can be printed into the main constructs that are formed using materials and cells [23, 63]. Electrospinning uses an electric field to produce nanofibers that can be used for cell adhesion [104]. Integrated extrusion based bioprinting and

electrospinning has been used to produce orthogonal arrays of hydrogel filaments in a grid-like arrangement with embedded nonwoven nanofibers (Figure 2.3C2) [105, 106]. Adopting laser beams (e.g. UV light beams) in extrusion based bioprinting supports the gelation of materials therefore the bioprintability (Figure 2.3C3) [100, 107]. The crosslinking of materials can be triggered by the laser beam during or after bioprinting, which greatly strengthens the mechanical stability of printed structures, especially for those materials with poor bioprintability [53]. Material droplets produced in inkjet-based bioprinting have a higher resolution compared to those produced in normal extrusion based bioprinting. Adopting a micro-valve technique in extrusion-base bioprinting to produce micro droplets as blocks for tissue scaffolds can be preferable because it not only improves the printing resolution by controlling the pressure and pulse frequency but is also compatible with a wide range of material types (Figure 2.3C4) [73, 108]. Microvalves are a typical mechanical configuration regulated by a controller to open and close the valve via applied air pressure or other forces, such as electromagnetic or piezoelectric forces [109]. A droplet can be produced within an open-and-close period by regulating the valve, or fibers can be deposited if the valve is forced to open. Similar to other nozzle-based systems, however, clogging is still a challenge when micro-valves are incorporated.

Table 2. 2 Extrusion based bioprinting approaches for multi-biomaterial/cell manipulation

Bioprinting system	Materials	Cell types	References
Multi-head extrusion based bioprinting system (one head activated at a time)	Alginate Alginate/PCL Alginate/hyaluronic acid (HA)	Bone marrow stromal cells Chondrocytes Schwann cells	[22] [92] [50]
Multi-head extrusion based bioprinting system (two or more heads activated at a time)	Alginate/gelatin; Collagen/HA Gelatin/fibrinogen/HA/glycerol/tricalcium phosphate/PCL Matrigel Gelatin/alginate/fibrinogen Alginate/gelatin	Osteoblasts Human embryonic kidney cells Human amniotic stem cells Alveolar epithelial type II cells Hela cells	[48], [28] [59] [116] [73] [117] [61]

	Polyurethane/alginate/gelatin/fibrinogen	Porcine aortic valve interstitial cell/smooth muscle cells Adipose-derived stem cell	[118]
Multi-arm extrusion based bioprinting system	Alginate/PCL	Chondrocytes	[60]
Microfluidic system of co-axial capillaries	Alginate/gelatin methacroyl Alginate/carbon nanotube Alginate/PCL Alginate/collagen/fibrinogen Collagen/alginate	Endothelial cells Human coronary artery smooth muscle cells Fibroblasts Epithelial cells/nerve cells/fibroblasts Keratinocytes/fibroblasts	[100] [110] [101] [51] [71]
Microfluidics system of lab-on-a-chip	PEGDA Alginate/propylene glycol alginate Chitosan	Fibroblasts PC12 cells Schwann cells	[115] [103] [119]
Integrated system of multi-arm and microfluidics techniques	Alginate	Cartilage progenitor cells	[63]
Integrated system of extrusion based bioprinting and electrospinning	Alginate/gelatin/PCL Alginate/ PCL	Human adipose-derived stem cells Osteoblasts	[106] [105]
Integrated system of extrusion based and laser-based bioprinting	Gelatin methacrylamide Gelatin methacrylamide/HA/PCL PEGDA	HepG2 cells Articular cartilage cells Breast epithelial cells	[120] [45] [121]
Valve integrated bioprinting system	Alginate Culture medium	Human induced pluripotent stem cells Human embryonic kidney cell/RC-10 cells	[108] [109]

One typical example of multi-material/cell manipulation in extrusion based bioprinting is bioprinting micro- or macro-channels to form vasculatures. The literature reports two alternative approaches, direct and indirect bioprinting, that have been

developed to produce channels [110, 111]. In direct bioprinting, channels with smooth lumen are continually bioprinted with the assistance of lab-on-a-chip or co-axial capillaries (Figure 2.4A). Materials that have fast crosslinking speed are often used to build the channels, combined with supporting cell types such as endothelial cells. One major challenge of direct vessel bioprinting for vascularization is guiding angiogenesis in an expected path, which requires precise deposition of channels in designated regions [112]. Thus, bioprinters with high printing resolution and more precise robotic systems are needed. Indirect vasculature bioprinting normally uses several materials, including fugitive or sacrificial ones (Figure 2.4B) [62]. Generally, sacrificial and functional materials are deposited from different bioprinting heads in a designated pattern. After the formation of scaffolds, the sacrificial materials are de-crosslinked as triggered by special conditions such as temperature change. As such, channels can be formed while the functional parts of the scaffolds remain [113, 114]. Indirect bioprinting is good for ensuring the mechanical stability of channels as they are formed after the solidification of structures, but it is difficult to encapsulate supporting cells because the de-crosslinking removes the incorporated cells [115]. Therefore, additional manipulations, such as cell seeding after de-crosslinking, are required to facilitate vascularization.

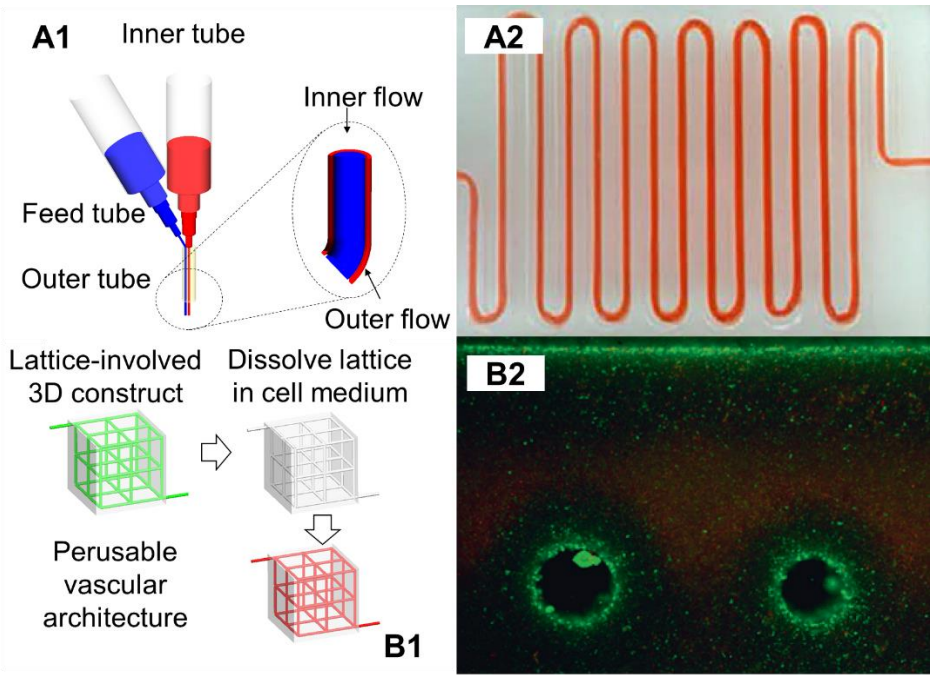

Figure 2. 4 Methods of vasculature bioprinting in tissue scaffolds. A1, schematic of the coaxial nozzle assembly for direct conduit printing; A2, printed meter-long conduit with successful medium perfusion. A2 is reused from [110]; B1, schematic of the interconnected lattice to serve as the sacrificial element for the indirect printing of vascular architectures; B2, primary rat hepatocytes and stabilizing stromal fibroblasts in agarose gels (slab versus channeled) after eight days. Cells survive at the gel perimeter and near perfused channels, but survival decays deeper in the gels. B2 is reused from [114].

2.4.3 Characterization of cell damage induced by the bioprinting process

Cells are subjected to stresses (e.g. shear stress, extensional stress) induced by the bioprinting process as they are forced to flow through the nozzle. Such stresses can elicit the deformation of cells and thus may breach the cell membrane [122]. Although cells can resist a certain level of these stresses, cell membranes may succumb to the stresses and lose the capacity to recover if the forces exceed a physiological threshold [123]. Cell membrane failure leads to cell dysfunction and damage, thus reducing the viability of cells. Therefore, investigation of the cell damage induced by the bioprinting process is important to understand how to preserve cell survival during the creation of tissue scaffolds.

Shear stress is believed to be one of the main factors that induces cell damage. Evidence shows that more cell damage occurs when higher dispensing pressures are applied, as they induce higher shear stress in extrusion based bioprinting [44, 124]. This result has been coincided by rheometer experiments in which cells are sheared under controllable stresses [125]. Experiments also demonstrate that exposure to shear stresses for longer durations greatly increases the number of damaged cells [126]. Compared to shear stress magnitude, cells seem more sensitive to exposure time given evidence that fewer cells are damaged under higher shear stress and limited shear time but more are damaged after longer shearing under low shear stress [120]. This observation is useful for determining the nozzle length, as it significantly affects the exposure time cells experience. Extensional stress is the other major factor that leads to cell damage in extrusion based bioprinting [52]. Extensional stress is generated due to the abrupt contraction in nozzle geometry as the materials/cells are forced through it, and has proven to be a more significant factor with respect to causing cell damage than shear stress [127]. Thus, reducing the extensional stress by modifying the nozzle shape is an important approach to reducing the number of damaged cells [58].

Maintaining high cell viability is one of the requirements set for the extrusion based bioprinting [59]. As mentioned above, using a low dispensing pressure can reduce the stresses induced by the bioprinting process but may not be appropriate for depositing viscous materials. One option to address this issue is the use of tapered nozzles in place of cylindrical ones [120]. Tapered nozzles have a relatively smooth contracting shape to achieve the flow of materials, and greatly reduce the effects of extensional stress on cells. Furthermore, the pressure to achieve the same volume flow rate can be much lower for a tapered nozzle than for a cylindrical nozzle, thus significantly reducing the shear stress [128]. The utilization of pre-crosslinked materials is another approach to protect cells from process-induced stresses. Gel particles can be formed after pre-crosslinking and used to isolate the encapsulated cells from the material solution. Therefore, they can be used as micro cell carriers to minimize induced stresses [52]. Pre-crosslinked materials with a viscosity that is too high or too low cannot affect the desired protection of cells, and determining the appropriate pre-crosslinked solutions often requires a series of tests [49].

Modeling is considered a feasible method to aid extrusion based bioprinting due to its ability to predict the physical and biological performance of printed materials and cells. Once validated by experiments, optimum designs and control based on the models can be achieved without the need for any extensive experiments. Several models have been developed to represent and predict cell damage in the bioprinting process. Because cell damage is associated with shear and extensional stresses, which are closely related to the dispensing pressure and nozzle diameter, empirical models have been established considering these two independent factors [129]. Although these models can predict the trend of cell damage, their feasibility might be limited because they do not consider cell damage mechanisms related to process-induced stresses. Directly selecting process-induced stresses and associated exposure times as factors when building cell damage models can be more effective, and before building the model, the theoretical range of cell damage should be considered, e.g. values cannot be less than 0% or over 100%.

Most existing models have been established based on the simplifying assumption that material/cell flows are fully developed as they flow through the nozzle, and only shear stress (and not extensional stress) is considered as the factor leading to cell damage. Computational fluid dynamics (CFD) has been developed to analyze the dynamic flow behavior and can be used to study the effect of extensional stress on cell damage in extrusion based bioprinting [130, 131]. Thus, a new model that considers the influence of both shear and extensional stresses on cell damage can be established to significantly improve the accuracy of cell damage representation and prediction.

2.5 Recommendations for future research

Despite all of the remarkable achievements in extrusion based tissue scaffold bioprinting technologies, many challenges still exist and prevent the realization of artificial tissue constructs. Therefore, more effort is required in the future to address these challenges and aid in the creation of tissue-like products for tissue regeneration.

2.5.1 Development of novel biomaterials for bioprinting

As materials play a central role in tissue scaffold bioprinting, the development of novel materials to overcome the limitations faced by current materials is of high priority.

Such materials should be biocompatible and bioprintable so they can faithfully represent the functions of complex tissue ECM. The use of a single material type may not be satisfactory to produce a suitable tissue environment for more than one functional cell type; therefore, using multiple materials in an organized pattern with associated cells would be more effective.

Decellularized ECM is a novel biomaterial derived from living tissue components, created by removing the resident cells and major histocompatibility complex but maintaining the major tissue structures [132]. Decellularized ECM has great potential to serve as a bioprinting material in tissue scaffold fabrication because it naturally satisfies the biocompatible requirement [15]. With the application of other bioprintable materials, a stable tissue scaffold can be created using decellularized ECM [54].

The utilization of programmable self-assembly materials that can be stimulated by cell growth or other specific cellular signals to transform into a desired pattern is another exciting option in tissue scaffold bioprinting. Using these kinds of materials for printing is also known as 4D printing [133]. In response to physiological cues or other external stimuli, the materials transform their morphology and functionality to adapt their physiological requirements according to pre-programmed properties. The development of such materials would significantly simplify the current bioprinting process and thus greatly enhance printing efficiency [134].

2.5.2 Development of novel bioprinting systems

The manipulation of multiple materials/cells in bioprinting is an efficient approach to produce tissue-like scaffolds. This approach has the potential to deposit different materials and cell types in a controllable manner to mimic tissue components [135]. Integrating rotational motion into existing linear motion bioprinting systems can greatly improve the efficiency and accuracy of manipulating materials and cells [10]. This method is versatile with respect to producing more complex 3D tissue scaffolds that have a composition and organization similar to tissues [60].

Developing a real-time control system to automatically monitor and adjust materials deposition during bioprinting can greatly improve the printing quality. In such systems, the deposited blocks can be detected, e.g. by a digital camera, and the achieved

visual information analyzed in time and subsequently sent back to the bioprinting system as a feedback signal. This signal is compared to the CAD model to produce an adjusted signal that can be used to control the bioprinting parameters to maintain the consistency of printed structures.

The utilization of nozzles in current extrusion based bioprinting limits the bioprinting resolution. Reducing the nozzle diameter is good in terms of resolution but can induce considerable cell damage. Therefore, nozzle-free bioprinting systems have great potential for improving resolution while maintaining cell viability. One existing option mentioned above to improve the resolution is to adopt micro-valve techniques in extrusion based bioprinting systems. In large-scale tissue scaffold bioprinting, the durability of valves should be carefully considered to maintain the accuracy and reproducibility of material/cell deposition.

2.5.3 Development of methods to create patterned vascular networks with bioprinted scaffolds

Although many studies have been performed, printing vascularized, metabolically active thick tissues such as lung or liver tissues still faces challenges. One approach to solve the problem of reproducing randomly distributed vasculature within a tissue is to ensure the interconnection of vascular networks by producing pre-patterned vasculatures [136]. With the assistance of microfluidic techniques, organized micro-channels can be created in scaffolds to form initial vascular networks. To avoid the collapse of bioprinted vasculatures, stiffer materials can be dispensed as a shell to protect soft inner channels. Therefore, co-axial vessels can consist of a hollow channel, a soft layer with cells, and a stiff shell from inner to outer, and can be used for later vascularization.

Growth factors are important regulators for angiogenesis. With the precise distribution of temporal or sequential growth factors in the tissue scaffolds, the formation of vasculatures including blood capillaries can be guided and facilitated. The maturation of vasculatures throughout the scaffold normally takes a long time, which introduces challenges with respect to maintaining the survival of other functional cells. One attempt to address this issue is using bioreactors. Bioreactors are engineered devices or systems that can provide a physiological environment to support the viability of cells while

facilitating biological structural fusion, remodeling, and maturation within a shorter time frame [137]. With the help of bioreactors, the viability of the encapsulated functional cells can be maintained during vascularization.

2.5.4 Representing and reducing process-induced cell damage

Developing comprehensive models that include factors such as extensional stress is recommended for accurately representing cell damage induced during the bioprinting process. These factors should also include cell-cell and cell-material interactions, which need to be considered when building cell damage models.

Modifying nozzle shape to reduce process-induced stresses has been attempted to reduce cell damage. Using tapered nozzles in place of cylindrical ones can greatly improve the survival of cells by alleviating stresses associated with extrusion [128]. Thus, designing and developing new nozzle types to further reduce process-induced stresses is an important future research direction aimed at minimizing cell damage and thereby optimizing cell viability.

2.6 Conclusions

Extrusion based bioprinting techniques have exhibited great versatility and feasibility in the fabrication of scaffolds for tissue engineering. For bioprinting a tissue scaffold, a typical procedure begins with scaffold design with appropriate structure and properties, followed by material/cell synthesis, scaffold bioprinting process, culturing of the printed scaffolds, and scaffold implantation for tissue repair or replacement. The implantation outcomes can be analyzed in terms of tissue regeneration and function restoration, and the result can also be further used as feedback to continuously improve the scaffold design and bioprinting process, and eventually the function restoration produced by the scaffolds. Over last decades, advances in both engineering techniques and life sciences have evolved extrusion based bioprinting from a simple technique to one able to create diverse tissue scaffolds from a wide range of biomaterials and cell types, significantly contributing to the advance of tissue engineering.

With encouraging results, current extrusion based bioprinting still faces challenges with respect to biomaterials for printing, manipulation of multi-materials/cells, vascular

networks within scaffolds, and cell-function preservation in scaffold bioprinting. The address of these challenges will significantly enhance the capability of extrusion based bioprinting so as to create scaffolds for various tissue engineering applications.

2.7 References

[1] Langer R., and Vacanti JP., Tissue engineering. *Science.* 1993, 260,920-26.

[2] Smetana Jr. K., Cell biology of hydrogels. *Biomaterials.* 1993, 14, 1046-50.

[3] Janmey PA., and McCulloch CA., Cell mechanics: integrating cell responses to mechanical stimuli. *Annu. Rev. Biomed. Eng.* 2007, 9, 1-34.

[4] Skardal A., and Atala A., Biomaterials for integration with 3-D bioprinting *Ann. Biomed. Eng*, 2015, 43, 730-46.

[5] Hollister SJ., Porous scaffold design for tissue engineering. *Nat. Mater.* 2005, 4, 518-24.

[6] Gunn JW., Turner SD., and Mann BK., Adhesive and mechanical properties of hydrogels influence neurite extension. *J. Biomed. Mater. Res. A* 2005, 72, 91-97.

[7] Zhang L., Yang X., Yue Y., Ye J., et al., Cyclic mechanical stress modulates neurotrophic and myelinating gene expression of Schwann cells. *Cell Prolif.* 2015, 48, 59-66.

[8] Larson C., and Shepherd R., *Microscale Technologies for Cell Engineering.* Switzerland Springer, 2016.

[9] Levato R., Visser J., Planell JA., Engel E., et al., Biofabrication of tissue constructs by 3D bioprinting of cell-laden microcarriers. *Biofabrication.* 2014, 6, 035020.

[10] Yeong WY., Chua CK., Leong KF., and Chandrasekaran M., Rapid prototyping in tissue engineering: challenges and potential. *Trends Biotechnol.* 2004, 22, 643-52.

[11] Landers R., Pfister A., Hübner U., John H., et al., Fabrication of soft tissue engineering scaffolds by means of rapid prototyping techniques. *J. Mater. Sci.* 2002, 37, 3107-16.

[12] Nakamura M., Kobayashi A., Takagi F., Watanabe A., et al., Biocompatible inkjet printing technique for designed seeding of individual living cells. *Tissue Eng.* 2005, 11, 1658-66.

[13] Hoque ME., Chuan YL., and Pashby I., Extrusion based rapid prototyping technique: an advanced platform for tissue engineering scaffold fabrication. *Biopolymers.* 2012, 97, 83-93.

[14] Ozbolat IT., and Hospodiuk M., Current advances and future perspectives in extrusion based bioprinting *Biomaterials* 2016, 76, 321-43.

[15] Harrison RH., St-Pierre JP., and Stevens MM., Tissue engineering and regenerative medicine: a year in review. *Tissue Eng. B* 2014, 20, 1-16.

[16] Chang Yan K., Nair K., and Sun W., Three-dimensional multi-scale modelling and analysis of cell damage in cell-encapsulated alginate constructs. *J. Biomech.* 2010, 43, 1031-38.

[17] Izadifar Z., Chapman LD., and Chen X., Computed tomography diffraction enhanced imaging for in situ visualization of tissue scaffolds implanted in cartilage. *Tissue Eng. C* 2013, 20, 140-48.

[18] Arai K., Iwanaga S., Toda H., Genci C., et al., Three-dimensional inkjet biofabrication based on designed images. *Biofabrication.* 2011, 3, 034113

[19] Coelho PG., Hollister SJ., Flanagan CL., and Fernandes PR., Bioresorbable scaffolds for bone tissue engineering: Optimal design, fabrication, mechanical testing and scale-size effects analysis. *Med. Eng. Phys.* 2015, 37, 287-96.

[20] Kantaros A., Chatzidai N., and Karalekas D., 3D printing-assisted design of scaffold structures *Int. J. Adv. Manuf. Tech.,* 2015, 1-13.

[21] Ferris CJ., Gilmore KG., and Wallace GG., Biofabrication: an overview of the approaches used for printing of living cells. *Appl. Microbiol. Biotechnol.* 2013, 97, 4243-58.

[22] Fedorovich NE,, Wijn JR., Verbout AJ., Alblas J., and Dhert WJ., Three dimensional fiber deposition of cell-laden, viable, patterned constructs for bone tissue printing. *Tissue Eng. A* 2008, 14, 127-33.

[23] Murphy SV., and Atala A., 3D bioprinting of tissues and organs. *Nat. Biotechnol.* 2014, 32, 773-85.

[24] Drury JL., and Mooney DJ., Hydrogels for tissue engineering: scaffold design variables and applications. *Biomaterials* 2003, 24, 4337-51.

[25] Ladet S., David L., and Domard A., Multi-membrane hydrogels *Nature* 2008, 452, 76-79.

[26] Augst AD., Kong HJ., and Mooney DJ., Alginate hydrogels as biomaterials *Macromol. Biosci.* 2006, 6, 623-33.

[27] Rickett TA., Amoozgar Z., Tuchek CA., Park J., et al., Rapidly photo-cross-linkable chitosan hydrogel for peripheral neurosurgeries. *Biomacromolecules.* 2010, 12, 57-65.

[28] Park JY., Choi JC., Shim JH., Lee JS., et al., A comparative study on collagen type I and hyaluronic acid dependent cell behavior for osteochondral tissue bioprinting. *Biofabrication.* 2014, 6, 035004.

[29] Bauer AJ., Liu J., Windsor LJ., Song F., and Li B., Current development of collagen-based biomaterials for tissue repair and regeneration. *Soft Mater.* 2014, 12, 359-70.

[30] Soman P., Kelber JA., Lee JW., Wright TN., et al., Cancer cell migration within 3D layer-by-layer microfabricated photocrosslinked PEG scaffolds with tunable stiffness. *Biomaterials.* 2012, 33, 7064-70.

[31] Geng L., Feng W., Hutmacher DW., San Wong Y., et al. Direct writing of chitosan scaffolds using a robotic system. *Rapid Prototyping J.* 2005, 11, 90-97.

[32] Mironov V., Reis N., and Derby B. Review: bioprinting: a beginning. *Tissue Eng.* 2006, 12, 631-34.

[33] Chen X., Schoenau G., and Zhang W., On the flow rate dynamics in time-pressure dispensing processes. *J. Dyn. Syst-T ASME.* 2002, 124, 693-708.

[34] Valkenaers H., Vogeler F., Voet A., and Kruth JP., Screw extrusion based 3D printing, a novel additive manufacturing technology. In COMA'13. Stellenbosch 2013. ISBN 978-0-7972-1405-7.

[35] Chen X., Modeling of rotary screw fluid dispensing processes. *J. Electron. Packaging.* 2007, 129, 172-78.

[36] Bian L., Hou C., Tous E., Rai R., et al., The influence of hyaluronic acid hydrogel crosslinking density and macromolecular diffusivity on human MSC chondrogenesis and hypertrophy. *Biomaterials.* 2013, 34, 413-21.

[37] Little CJ., Bawolin NK., and Chen X., Mechanical properties of natural cartilage and tissue-engineered constructs. *Tissue Eng. B* 2011, 17, 213-27.

[38] Wang X., Rijff BL., and Khang G., A building-block approach to 3D printing a multichannel, organ-regenerative scaffold. *J. Tissue Eng. Regen. Med*. 2015, DOI: 10.1002/term.2038.

[39] Nishiyama Y., Nakamura M., Henmi C., Yamaguchi K., et al., Development of a three-dimensional bioprinter: construction of cell supporting structures using hydrogel and state-of-the-art inkjet technology. *J. Biomech. Eng*. 2009, 131, 035001.

[40] Levental I., Georges PC., and Janmey PA., Soft biological materials and their impact on cell function. *Soft Matter.* 2007, 3, 299-306.

[41] Tallawi M., Rai R., Boccaccini AR., and Aifantis KE., Effect of substrate mechanics on cardiomyocyte maturation and growth. *Tissue Eng. B* 2014, 21, 157-65.

[42] Hennink W., and Van Nostrum C., Novel crosslinking methods to design hydrogels. *Adv. Drug Del. Rev.* 2012, 64, 223-36.

[43] Landers R., Hübner U., Schmelzeisen R., and Mülhaupt R., Rapid prototyping of scaffolds derived from thermos-reversible hydrogels and tailored for applications in tissue engineering. *Biomaterials.* 2002, 23, 4437-47.

[44] Desai ES., Tang MY., Ross AE., and Gemeinhart RA., Critical factors affecting cell encapsulation in superporous hydrogels. *Biomed. Mater.* 2012, 7, 024108.

[45] Schuurman W., Levett P A., Pot MW., van Weeren PR., et al., Gelatin-Methacrylamide Hydrogels as Potential Biomaterials for Fabrication of Tissue-Engineered Cartilage Constructs. *Macromol. Biosci.* 2013, 13, 551-61.

[46] Rajaram A., Chen XB., and Schreyer DJ., Strategic design and recent fabrication techniques for bioengineered tissue scaffolds to improve peripheral nerve regeneration. *Tissue Eng. B* 2012, 18, 454-67.

[47] Ahn S., and Kim G., Cell-encapsulating alginate microsized beads using an air-assisted atomization process to obtain a cell-laden hybrid scaffold. *J. Mater. Chem. B* 2015, 3, 9132-39.

[48] Zehnder T., Sarker B., Boccaccini AR., and Detsch R., Evaluation of an alginate–gelatine crosslinked hydrogel for bioplotting. *Biofabrication.* 2015, 7, 025001.

[49] Lee H., Ahn S., Chun W., and Kim G., Enhancement of cell viability by fabrication of macroscopic 3D hydrogel scaffolds using an innovative cell dispensing technique supplemented by preosteoblast-laden micro-beads. *Carbohydr. Polym.* 2014, 104, 191-98.

[50] Rajaram A., Schreyer D., and Chen D., Bioplotting alginate/hyaluronic acid hydrogel scaffolds with structural integrity and preserved schwann cell viability. *3D Printing and Additive Manuf.* 2014, 1, 194-203.

[51] Onoe H., Okitsu T., Itou A., Kato-Negishi M., et al., Metre-long cell-laden microfibers exhibit tissue morphologies and functions. *Nat. Mater.* 2013, 12, 584-90.

[52] Aguado BA., Mulyasasmita W., Su J., Lampe KJ., and Heilshorn SC., Improving viability of stem cells during syringe needle flow through the design of hydrogel cell carriers. *Tissue Eng. A* 2011, 18, 806-15.

[53] Knowlton S., Onal S., Yu CH., Zhao J., and Tasoglu S., Bioprinting for cancer research. *Trends Biotechnol.* 2015, 33, 504-13.

[54] Pati F., Jang J., Ha DH., Kim SW., et al., Printing three-dimensional tissue analogues with decellularized extracellular matrix bioink. *Nat. Commun.* 2014, 5, 1-11.

[55] Skoog SA., Goering PL., and Narayan RJ., Stereolithography in tissue engineering. *J. Mater. Sci. Mater. Med.* 2014, 25, 845-56.

[56] Ovsianikov A., Gruene M., Pflaum M., Koch L., et al., Laser printing of cells into 3D scaffolds. *Biofabrication.* 2010, 2, 014104.

[57] Chiono V., Pulieri E., Vozzi G., Ciardelli G., Genipin-crosslinked chitosan/gelatin blends for biomedical applications. *J. Mater. Sci. Mater. Med.* 2008, 19, 889-98.

[58] Tanzeglock T., Soos M., Stephanopoulos G., and Morbidelli M., Induction of mammalian cell death by simple shear and extensional flows. *Biotechnol. Bioeng.* 2009, 104, 360-70.

[59] Ouyang L., Yao R., Chen X., Na J., and Sun W., 3D printing of HEK 293FT cell-laden hydrogel into macroporous constructs with high cell viability and normal biological functions. *Biofabrication.* 2015, 7, 015010.

[60] Schuurman W., Khristov V., Pot M., Van Weeren P., et al., Bioprinting of hybrid tissue constructs with tailorable mechanical properties. *Biofabrication.* 2011, 3, 021001.

[61] Duan B., Hockaday LA., Kang KH., and Butcher JT., 3D bioprinting of heterogeneous aortic valve conduits with alginate/gelatin hydrogels. *J. Biomed. Mater. Res. A* 2013, 101, 1255-64.

[62] Bertassoni LE., Cardoso JC., Manoharan V., Cristino AL., et al., Direct write bioprinting of cell-laden methacrylated gelatin hydrogels. *Biofabrication.* 2014, 6, 024105.

[63] Ozbolat IT., Chen H., and Yu Y., Development of 'Multi-arm Bioprinter' for hybrid biofabrication of tissue engineering constructs. *Robot. Com-Int. Manuf.* 2014, 30, 295-304.

[64] Hsieh FY., Lin HH., and Hsu Sh., 3D bioprinting of neural stem cell-laden thermos responsive biodegradable polyurethane hydrogel and potential in central nervous system repair. *Biomaterials.* 2015, 71, 48-57.

[65] Gao G., Yonezawa T., Hubbell K., Dai G., and Cui X., Inkjet-bioprinted acrylated peptides and PEG hydrogel with human mesenchymal stem cells promote robust bone and cartilage formation with minimal printhead clogging. *Biotech. J.* 2015, 10, 1568-77.

[66] Nishiyama Y., Henmi C., Iwanaga S., Nakagawa H., et al., Ink jet three-dimensional digital fabrication for biological tissue manufacturing: analysis of alginate microgel beads produced by ink jet droplets for three dimensional tissue fabrication. *J. Imaging Sci. Technol.* 2008, 52, 60201-1.

[67] Chan V., Zorlutuna P., Jeong JH., Kong H., and Bashir R., Three-dimensional photopatterning of hydrogels using stereolithography for long-term cell encapsulation. *Lab Chip.* 2010, 10, 2062-70.

[68] Melchels FP., Feijen J., and Grijpma DW., A review on stereolithography and its applications in biomedical engineering. *Biomaterials.* 2010, 31, 6121-30.

[69] Melissinaki V., Gill A., Ortega I., Vamvakaki M., et al., Direct laser writing of 3D scaffolds for neural tissue engineering applications. *Biofabrication.* 2011, 3, 045005.

[70] Castilho M., Rodrigues J., Pires I., Gouveia B., et al., Fabrication of individual alginate-TCP scaffolds for bone tissue engineering by means of powder printing. *Biofabrication.* 2015, 7, 015004.

[71] Kim G., Ahn S., Kim Y., Cho Y., and Chun W., Coaxial structured collagen–alginate scaffolds: fabrication, physical properties, and biomedical application for skin tissue regeneration. *J. Mater. Chem.* 2011, 21, 6165-72.

[72] Kundu J., Shim JH., Jang J., Kim SW., and Cho DW., An additive manufacturing-based PCL–alginate–chondrocyte bioprinted scaffold for cartilage tissue engineering. *J. Tissue Eng. Regen. Med.* 2013, 9, 1286-97.

[73] Horváth L., Umehara Y., Jud C., Blank F., et al., Engineering an in vitro air-blood barrier by 3D bioprinting. *Sci. Rep.* 2015, 5, 1-8.

[74] Choi YJ., Kim TG., Jeong J., Yi JJ., et al., 3D Cell Printing of Functional Skeletal Muscle Constructs Using Skeletal Muscle. *Adv. Healthc. Mater.* 2016, 5, 2636-45.

[75] Wang X., Yan Y., and Zhang R., Rapid prototyping as a tool for manufacturing bioartificial livers. *Trends Biotechnol.* 2007, 25, 505-13.

[76] Struzyna LA., Katiyar K., and Cullen DK., Living scaffolds for neuro regeneration. *Curr. Opin. Solid State Mater. Sci.* 2014, 18, 308-18.

[77] Dimri GP., Lee X., Basile G., Acosta M., A biomarker that identifies senescent human cells in culture and in aging skin in vivo. *Proc. Nati. Acad. Sci.* 1995, 92, 9363-67.

[78] Mehrban N., Teoh GZ., and Birchall MA., 3D bioprinting for tissue engineering: Stem cells in hydrogels. *Int. J. Bioprinting* 2016, 1, 1-14.

[79] Takahashi K., and Yamanaka S., Induction of pluripotent stem cells from mouse embryonic and adult fibroblast cultures by defined factors. *Cell* 2006, 126, 663-76.

[80] Lee VK., Lanzi AM., Ngo H., Yoo SS., et al., Generation of multi-scale vascular network system within 3D hydrogel using 3D bioprinting technology. *Cell. Mol. Bioeng.* 2014, 7, 460-72.

[81] Murr LE., *Handbook of Materials Structures, Properties, Processing and Performance.* Switzerland Springer, 2015.

[82] Wüst S., Godla ME., Müller R., and Hofmann S., Tunable hydrogel composite with two-step processing in combination with innovative hardware upgrade for cell-based three-dimensional bioprinting. *Acta Biomater.* 2014, 10, 630-40.

[83] Ning L., Xu Y., Chen X., and Schreyer DJ., Influence of mechanical properties of alginate-based substrates on the performance of Schwann cells in culture. *J. Biomater. Sci. Polym. Ed.* 2016, 27, 898-915.

[84] Carrow JK., and Gaharwar AK., Bioinspired polymeric nanocomposites for regenerative medicine. *Macromol. Chem. Phys.* 2015, 216, 248-64.

[85] Zeng Q., Han Y., Li H., and Chang J., Bioglass/alginate composite hydrogel beads as cell carriers for bone regeneration. *J. Biomed. Mater. Res. B* 2014, 102, 42-51.

[86] Xu M., Wang X., Yan Y., Yao R., and Ge Y., An cell-assembly derived physiological 3D model of the metabolic syndrome, based on adipose-derived stromal cells and a gelatin/alginate/fibrinogen matrix. *Biomaterials* 2010, 31, 3868-77.

[87] Grigore A., Sarker B., Fabry B., Boccaccini AR., and Detsch R., Behavior of encapsulated MG-63 cells in RGD and gelatine-modified alginate hydrogels. *Tissue Eng. A* 2014, 20, 2140-50.

[88] Rowley JA., Madlambayan G., and Mooney DJ., Alginate hydrogels as synthetic extracellular matrix materials. *Biomaterials.* 1999, 20, 45-53.

[89] Yu TT., and Shoichet MS., Guided cell adhesion and outgrowth in peptide modified channels for neural tissue engineering. *Biomaterials.* 2005, 26, 1507-14.

[90] Jeon O., Song SJ., Lee KJ., Park MH., et al. Mechanical properties and degradation behaviors of hyaluronic acid hydrogels cross-linked at various cross-linking densities. *Carbohydr Polym*. 2007, 70, 251-57.

[91] Zhu N., Li M., Cooper D., and Chen X., Development of novel hybrid poly (L-lactide)/chitosan scaffolds using the rapid freeze prototyping technique. *Biofabrication.* 2011, 3, 034105.

[92] Izadifar Z., Chang T., Kulyk WM., Chen X., and Eames BF., Analyzing biological performance of 3D-printed, cell-impregnated hybrid constructs for cartilage tissue engineering. *Tissue Eng.* 2015, 22, 173-188.

[93] Zhao X., Liu L., Wang J., Xu Y., et al., *In vitro* vascularization of a combined system based on a 3D printing technique. *J. Tissue Eng. Regen. Med*. 2014, 10, 833-42.

[94] Tan EY., and Yeong WY., Concentric bioprinting of alginate-based tubular constructs using multi-nozzle extrusion based technique. *Int. J. Bioprinting* 2015, 1, 49-56.

[95] Park S., Kim S., and Choi J., Development of a multi-nozzle bioprinting system for 3D tissue structure fabrication. *Control, Automation and Systems (ICCAS), 2015 15th International Conference on IEEE* 2015, 1874-77.

[96] Lee BR., Lee KH., Kang E., Kim DS., and Lee SH., Microfluidic wet spinning of chitosan-alginate microfibers and encapsulation of HepG2 cells in fibers. *Biomicrofluidics.* 2011, 5, 022208.

[97] Gao Q., He Y., Fu J., Liu A., and Ma L., Coaxial nozzle-assisted 3D bioprinting with built-in microchannels for nutrients delivery. *Biomaterials.* 2015, 61, 203-15.

[98] Jung JH., Choi CH., Chung S., Chung YM., and Lee CS., Microfluidic synthesis of a cell adhesive Janus polyurethane microfiber. *Lab Chip.* 2009, 9, 2596-602.

[99] Zhang Y., Yu Y., and Ozbolat IT., Direct Bioprinting of Vessel-Like Tubular Microfluidic Channels. *J. Nanotechnol. Eng. Med.* 2013, 4, 020902.

[100] Colosi C., Shin SR., Manoharan V., Massa S., et al., Microfluidic Bioprinting of Heterogeneous 3D Tissue Constructs Using Low-Viscosity Bioink. *Adv. Mater.* 2015, 28, 677-84.

[101] Cornock R., Beirne S., Thompson B., and Wallace G., Coaxial additive manufacture of biomaterial composite scaffolds for tissue engineering. *Biofabrication.* 2014, 6, 025002.

[102] Li PC., *Microfluidic lab-on-a-chip for chemical and biological analysis and discovery.* CRC Boca Raton Taylor & Francis 2005.

[103] Kitagawa Y., Naganuma Y., Yajima Y., Yamada M., and Seki M., Patterned hydrogel microfibers prepared using multilayered microfluidic devices for guiding network formation of neural cells. *Biofabrication.* 2014, 6, 035011.

[104] Zhang L., Huang J., Si T., and Xu RX., Coaxial electrospray of microparticles and nanoparticles for biomedical applications. *Expert Rev. Med. Devices.* 2012, 9, 595-612.

[105] Lee H., and Kim G., Enhanced cellular activities of polycaprolactone/alginate based cell-laden hierarchical scaffolds for hard tissue engineering applications. *J. Colloid Interface Sci.* 2014, 43, 315-25.

[106] Yu YZ., Zheng LL., Chen HP., Chen WH., and Hu QX., Fabrication of hierarchical polycaprolactone/gel scaffolds via combined 3D bioprinting and electrospinning for tissue engineering. *Adv. Manuf.* 2014, 2, 231-38.

[107] Balčiūnas E., Lukoševičius L., Mackevičiūtė D., Rekštytė S., et al., Combination of thermal extrusion printing and ultrafast laser fabrication for the manufacturing of 3D composite scaffolds. *International Society for Optics and Photonics* 2014, 201489721N-N-10.

[108] Faulkner-Jones A., Fyfe C., Cornelissen DJ., Gardner J., et al., Bioprinting of human pluripotent stem cells and their directed differentiation into hepatocyte-like cells for the generation of mini-livers in 3D. *Biofabrication.* 2015, 7, 044102.

[109] Faulkner-Jones A., Greenhough S., King JA., Gardner J., et al., Development of a valve-based cell printer for the formation of human embryonic stem cell spheroid aggregates. *Biofabrication.* 2013, 5, 015013.

[110] Dolati F., Yu Y., Zhang Y., De Jesus AM., et al., In vitro evaluation of carbon-nanotube-reinforced bioprintable vascular conduits. *Nanotech.* 2014, 25, 145101.

[111] Min Z., Shichang Z., Chen X., Yufang Z., and Changqing Z., 3D-printed dimethyloxallyl glycine delivery scaffolds to improve angiogenesis and osteogenesis. *Biomat. Sci.* 2015, 3, 1236-44.

[112] Sarker M., Chen X., and Schreyer D., Experimental approaches to vascularisation within tissue engineering constructs. *J. Biomater. Sci. Polym. Ed.* 2015, 26 683-734.

[113] Zhao L., Lee V K., Yoo SS., Dai G., and Intes X., The integration of 3-D cell printing and mesoscopic fluorescence molecular tomography of vascular constructs within thick hydrogel scaffolds. *Biomaterials.* 2012, 33, 5325-32.

[114] Miller JS., Stevens KR., Yang MT., Baker BM., et al., Rapid casting of patterned vascular networks for perfusable engineered three-dimensional tissues. *Nat. Mater.* 2012, 11, 768-74.

[115] Yue T., Nakajima M., Takeuchi M., Hu C., et al., On-chip self-assembly of cell embedded microstructures to vascular-like microtubes. *Lab Chip.* 2014, 14, 1151-61.

[116] Kang HW., Lee SJ., Ko IK., Kengla C., et al., A 3D bioprinting system to produce human-scale tissue constructs with structural integrity. *Nat. Biotechnol.* 2016, 34, 312-19.

[117] Zhao Y., Yao R., Ouyang L., Ding H, et al., Three-dimensional printing of Hela cells for cervical tumor model in vitro. *Biofabrication.* 2014, 6, 035001.

[118] Huang Y., He K., and Wang X., Rapid prototyping of a hybrid hierarchical polyurethane-cell/hydrogel construct for regenerative medicine. *Mat. Sci. Eng C.* 2013, 33. 3220-29.

[119] Yeh CH., Lin PW., and Lin YC., Chitosan microfiber fabrication using a microfluidic chip and its application to cell cultures. *Microfluid. Nanofluid.* 2010, 8, 115-21.

[120] Billiet T., Gevaert E., De Schryver T., Cornelissen M., and Dubruel P., The 3D printing of gelatin methacrylamide cell-laden tissue-engineered constructs with high cell viability. *Biomaterials.* 2014, 35, 49-62.

[121] Shim JH., Lee JS., Kim JY., and Cho DW., Bioprinting of a mechanically enhanced three-dimensional dual cell-laden construct for osteochondral tissue engineering using a multi-head tissue/organ building system. *J. Micromech. Microeng.* 2012, 22, 085014.

[122] Gupta R., Truong L., Bear D., Chafik D., et al., Shear stress alters the expression of myelin-associated glycoprotein (MAG) and myelin basic protein (MBP) in Schwann cells. *J. Orth. Res.* 2005, 23, 1232-39.

[123] Fletcher DA., and Mullins RD., Cell mechanics and the cytoskeleton. *Nature.* 2010, 463, 485-92.

[124] Chang R., Nam J., and Sun W., Effects of dispensing pressure and nozzle diameter on cell survival from solid freeform fabrication-based direct cell writing. *Tissue Eng. A* 2008, 14, 41-48.

[125] Ning L., Guillemot A., Zhao J., Kipouros G., and Chen X., Influence of flow behavior of alginate-cell suspensions on cell viability and proliferation. *Tissue Eng. C* 2016, 22, 652-62.

[126] Li M., Tian X., Zhu N., Schreyer DJ., and Chen X., Modeling process-induced cell damage in the biodispensing process. *Tissue Eng. C* 2009, 16, 533-42.

[127] Lee SS., Yim Y., Ahn KH., and Lee SJ., Extensional flow-based assessment of red blood cell deformability using hyperbolic converging microchannel. *Biomed. Microdevices* 2009, 11, 1021-27.

[128] Li M., Tian X., Schreyer DJ., and Chen X., Effect of needle geometry on flow rate and cell damage in the dispensing-based biofabrication process. *Biotechnol. Prog.* 2011, 27, 1777-84.

[129] Nair K., Gandhi M., Khalil S., Yan KC., et al., Characterization of cell viability during bioprinting processes. *Biotech. J.* 2009, 4, 1168-77.

[130] Vitale F., Nam J., Turchetti L., Behr M., et al., A multiscale, biophysical model of flow-induced red blood cell damage. *AICHE J.* 2014, 60, 1509-16.

[131] Down LA., Papavassiliou DV., and Edgar A., Significance of extensional stresses to red blood cell lysis in a shearing flow. *Ann. Biomed. Eng.* 2011, 39, 1632-42.

[132] Song J., Guyette JP., Gilpin SE., Gonzalez G., et al., Regeneration and experimental orthotopic transplantation of a bioengineered kidney. *Nat. Med.* 2013, 19, 646-51.

[133] Tibbits S., 4D Printing: Multi-Material Shape Change. *Archit. Design* 2014, 84, 116-21.

[134] An J., Chua CK., and Mironov V., A perspective on 4D bioprinting. *Int. J. Bioprinting.* 2016, 2, 3-5.

[135] Billiet T., Vandenhaute M., Schelfhout J., Van Vlierberghe S., and Dubruel P., A review of trends and limitations in hydrogel-rapid prototyping for tissue engineering. *Biomaterials.* 2012, 33, 6020-41.

[136] Norotte C., Marga FS., Niklason LE., and Forgacs G., Scaffold-free vascular tissue engineering using bioprinting. *Biomaterials.* 2009, 30, 5910-17.

[137] Stephens J., Cooper J., Phelan F., and Dunkers J., Perfusion flow bioreactor for 3D in situ imaging: investigating cell/biomaterials interactions. *Biotechnol. Bioeng.* 2007, 97, 952-61.

CHAPTER 3

Influence of Mechanical Properties of Alginate-based Substrates on the Performance of Schwann Cells in Culture

This chapter has been published as "Liqun Ning, Yitong Xu, Xiongbiao Chen and David J. Schreyer, Influence of mechanical properties of alginate-based substrates on the performance of Schwann cells in culture. *Journal of Biomaterials Science, Polymer Edition*. 2016, 27, 898-915." According to the Copyright Agreement, "the authors retain the right to include the journal article, in full or in part, in a thesis or dissertation".

3.1 Abstract

In tissue engineering, artificial tissue scaffolds containing living cells have been studied for tissue repair and regeneration. Notably, the performance of these encapsulated-in-scaffolds cells in terms of cell viability, proliferation and expression of function during and after the scaffold fabrication process, has not been well documented because of the influence of mechanical, chemical, and physical properties of the scaffold substrate materials. This chapter presents our study on the influence of mechanical properties of alginate-based substrates on the performance of Schwann cells, which are the major glial cells of peripheral nervous system. Given the fact that alginate polysaccharide hydrogel has poor cell adhesion properties, in this study we examined several types of cell-adhesion supplements and found that alginate covalently-modified with RGD peptide provided improved cell proliferation and adhesion. We prepared alginate-based substrates for cell culture using varying alginate concentrations for altering their mechanical properties, which were confirmed by compression testing. Then, we examined the viability, proliferation, morphology, and expression of the extracellular matrix protein laminin of Schwann cells that were seeded on the surface of alginate-based substrates (or 2D culture) or encapsulated within alginate-based substrates (3D cultures), and correlated the examined cell performance to the alginate concentration (or mechanical properties) of hydrogel substrates. Our findings suggest that covalent attachment of RGD peptide can improve the success of Schwann cell encapsulation within alginate-based scaffolds, and provide

guidance for regulating the mechanical properties of alginate-based scaffolds containing Schwann cells for applications in peripheral nervous system regeneration and repair.

3.2 Introduction

Tissue engineering is an interdisciplinary field, wherein both biological and engineering techniques are used to fabricate appropriate tissue scaffolds to restore and repair tissues or organs [1-3]. To mimic native tissue structures, various advanced fabrication techniques have been developed to create tissue scaffolds from biomaterials and living cells [4]. Among these techniques, 3D bioprinting, by which the solution of biomaterial(s) with living cells is continuously applied, has shown the most promising due to its ability to apply a variety of biomaterial solutions and cells with a high printing resolution, layer-by-layer to form 3D constructs [5-7]. Notably, the success of scaffolds fabrication based on the 3D bioprinting technique depends on if the scaffold-encapsulated cells can survive during the fabrication process and retain the cell functions in the following tissue or organ repair process [8].

Biomaterials serve as a synthetic ECM to support cells during and after biofabrication of tissue scaffolds and as such, they must be chosen to be biocompatible and amenable to the process of scaffold biofabrication. Among various biomaterials, hydrogels have been widely used in tissue repair and drug delivery since they can provide adjustable physical and chemical properties [9]. Alginate, a naturally derived polysaccharide extracted from seaweed, has been used in the 3D bioprinting based fabrication for decades because of its good biocompatibility and convenient gelation process achieved by crosslinking with calcium ions at mild physiological conditions [10]. The use of alginate as an artificial substrate for culturing different types of cells like Schwann cells [11], myoblasts [12], chondrocytes [13], endothelial cells [14], and fibroblasts [15] has been reported in previous studies.

In nerve tissue engineering, Schwann cells play an important role in promoting axonal regeneration [16-18]. Our previous study illustrate Schwann cells can be incorporated in the biofabrication process to create scaffolds from alginate [19]. Meanwhile, it is also noticed that alginate hydrogels are hydrophilic and have limited capability to provide cues for cell attachment. For improvement, several approaches have

been reported in the literature and the most common method is simply mixing the alginate solution with such proteins as laminin and fibronectin prior to its gelation by calcium crosslinking [20-23]. Alternatively, isolated peptides derived from these proteins such as RGD from fibronectin, YIGSR and IKVAV from laminin can be covalently bound to alginate to improve cell adhesion *in vitro* [24]. Although physically mixing peptides or proteins with alginate is quite simple and has been achieved with certain degrees of success, the improvement in cell functions is limited because lower and less stable concentrations of peptide and protein are achieved [25]. In the other hand, the effects of relatively higher concentration of adhesion peptide and protein added to alginate on the cell adhesion and proliferation have not been well documented.

Previous studies have shown that the interactions of cells with artificial scaffolds/substrates can be influenced by the mechanical properties of scaffolds/substrates [26]., and that mechanical cues can be further used to regulate cell behaviors such as cell migration, proliferation and differentiation [27]. Two types of mechanical cues that cells experience when cultured on or within hydrogels are the resistance from the hydrogel itself, and applied external forces to the hydrogel constructs [24, 27]. The resistance due to hydrogel stiffness is the most common mechanical cue that greatly influences the fate of both surface-seeded cells and cells encapsulated within gels. Cells can respond differently based on the substrate stiffness and it is believed that cell behavior can be improved if cultured in a mechanically-favor environment [28-30]. This raises a need to control the mechanical properties of substrate for improved cell performance.

The present study aims to investigate the influence of the stiffness of biomaterial substrates on viability, proliferation, morphology indicative of adhesion, and protein expression of Schwann cells as a prelude to the development of tissue scaffolds for nerve tissue engineering. In two-dimensional (2D) culture experiments, immortalized rat Schwann cells were seeded onto the surface of alginate hydrogels, and their morphology and viability were examined when the hydrogels were supplemented with the cell adhesion enhancing materials fibronectin, PLL and RGD peptide. For RGD peptide, both physically mixed RGD-alginate and RGD covalently modified alginate substrates were employed for examination. Then, cell adhesion peptide modified alginate hydrogels with different levels of stiffness were prepared using various alginate concentrations from 1.0% to 2.5% (w/v),

and the influence of the mechanical properties of alginate on the performance of both surface-seeded cells (2D culture) and encapsulated cells (3D culture) were investigated, in term of Schwann cell viability, proliferation, adhesion, and protein expression.

3.3 Materials and methods

3.3.1 Cell culture

An immortalized rat Schwann cell line (RSC96), provided by American Type Culture Collection (Manassas, VA, USA), was cultured in standard Dulbecco's Modified Eagle's Medium (DMEM) (Sigma-Aldrich, Oakville, ON, Canada) supplemented with 10% fetal bovine serum (FBS) (GIBCO, Life Technologies, Burlington, ON, Canada), in a humidified incubator at 37°C with a 5% CO_2 atmosphere. For the 2D cell culture, suspension of Schwann cells with a density of 4×10^4 cells/mL were added onto the surface of pre-gelled alginate (see below) in 24- or 96-well plates. For the 3D culture, Schwann cells were added into alginate solution to form the cell suspension with a density of 4×10^4 cells/mL, which was then pipetted into 24-well plates and gelled by calcium crosslinking.

3.3.2 Materials

Low viscosity sodium alginate with a molecular weight of 12,000 - 80,000 Da was obtained from Sigma-Aldrich, Canada. Standard DMEM and calcium-free DMEM cell culture media were obtained from GIBCO Life Technologies (Burlington, ON, Canada). Calcium chloride ($CaCl_2$), sodium chloride (NaCl), sodium hydroxide (NaOH), PEI (polyethyleneimine), BSA (Bovine Serum Albumin), Tween 20, EDC (N-(3-Dimethylaminopropyl)-N'-ethylcarbodiimide hydrochloride), NHS (N-Hydroxysuccinimide), MES, poly-L-lysine (PLL), DAPI fluorescent dye, fibronectin, primary rabbit anti-laminin antibody, and secondary AF 488 anti-rabbit IgG and AF 555 anti-rabbit IgG antibodies were purchased from Sigma-Aldrich, Canada. Primary rabbit anti-S100 was purchased from Abcam (Eugene, OR, USA). RGD peptide (GGGGRGDS), calcein-AM, and propidium iodide were purchased from AnaSpec (Freemont, CA, USA).

3.3.3 Hydrogel substrate preparation

Low viscosity sodium alginate (Sigma-Aldrich) with a molecular weight of 12,000 - 80,000 Da was dissolved in deionized water to form a 0.5% (w/v) solution. A 0.22 μm bottle-top filter (Thermo Scientific, Ann Arbor, MI, USA) was used to filter sterilize the alginate solution. The filtered alginate solution was frozen (-40° C) for 24 hours and dried in a FreeZone Freeze Dryer (Labconco, USA) under sterile conditions. A 5% (w/v) alginate stock solution was made by dissolving sterile, freeze-dried alginate in the calcium-free DMEM. In our first experiment, alginate solutions (1.0%, 1.5%, 2.0% and 2.5% w/v) were used to form gels by ionic crosslinking after submersion in 100 mM $CaCl_2$ for 5 min.

In other experiments, alginate containing additives to promote cell adhesion were prepared and used. Specifically, PLL was mixed into 1.5% (w/v) alginate, forming solutions with concentrations of 50, 100, 200, and 500 μg/mL, respectively. Fibronectin was added to form solutions with concentrations of 100, 250, and 500 μg/mL. RGD peptide was added to obtain a final peptide concentration of 50 and 100 μg/mL. The aforementioned process of mixing was performed gently using a pipette to ensure the homogenous distribution within the solution.

RGD peptide was also covalently bound to alginate in solution as per the previous study [12], with the weight ratio of 1:100 and 1:250 (w/w) compared to alginate. Briefly, 305 mM EDC, 115 mM NHS and 300 mM NaCl were dissolved in 100 mM MES buffer, and 10 N NaOH was dropped into the solution to adjust the pH value near to 6.5; RGD solution and alginate solution with designed concentrations were mixed in and rotated over 48 hours for reaction at a room temperature and then dialyzed for 3 days at 4°C to remove all small and unreacted reagents; the obtained solution was eventually lyophilized and dissolved in calcium-free DMEM to obtain the RGD modified alginate solution at concentrations of 1.0%, 1.5%, 2.0% and 2.5% w/v, respectively. 300 μL of each alginate solution was loaded into the wells of 24-well plates, or 50 μL to each well of 96-well plates. 100 mM $CaCl_2$ of the double volume of alginate was layered over the alginate solution, allowing for crosslinking for 5 minutes [31]. Then, the medium was aspirated and the resultant alginate gels were washed using 10 mM PBS and then DMEM (normal calcium concentration). Plastic wells coated with 50 μg/mL PLL (24 hours at 37 °C) were used as a positive control. Five samples were prepared for each material (n=5).

To investigate the influence of hydrogel stiffness on the 2D cell culture, RGD modified alginate at various concentrations (1.0%, 1.5%, 2.0% and 2.5% w/v) was tested. Alginate solution was dropped onto glass coverslips coated with 0.1% w/v PEI solution, and gelled in a 24-well plate before cell seeding. For the 3D cell culture, the same concentrations of RGD modified alginate (1.0%, 1.5%, 2.0% and 2.5% w/v) was used to form gels; a suspension of Schwann cells was added in each alginate solution prior to crosslinking; 50 µl of alginate containing Schwann cells was then loaded onto glass coverslip coated with 0.1% w/v PEI solution and crosslinked using 100 mM $CaCl_2$ for 5 min in 24-well plates.

3.3.4 Evaluation of hydrogel mechanical properties

The alginate hydrogels formed with different concentrations of alginate solution were tested using a compressive testing instrument (Texture Technologies Corp., USA), to evaluate the hydrogel mechanical properties. Alginate at various concentrations (1.0%, 1.5%, 2.0% and 2.5% w/v) was pipetted into cylindrical molds with a diameter 7 mm and a height of 12 mm. Gelation was initially obtained by immersing the molds into 100 mM calcium ion solution for 24 hours. Then the samples were removed from the molds and soaked in calcium solution again for another 24 hours. In the compressive tests, a speed of 0.1 mm/s was applied to move a total distance of 10.5 mm and data were collected at a sampling rate of 50 Hz. The compressive modulus (or the Young's modulus) for each gel sample was calculated from the linear section of the measured stress-strain curve, or before the gel yields. In each test, four samples were compressed and their compressive moduli were averaged for evaluation.

3.3.5 Evaluation of Schwann cell morphology

To investigate the effects of the alginate substrates on cell spreading and extension, morphological observation of cells was performed using an optical microscope (Zeiss Axiovert). One mL cell suspension (2×10^4 cells/mL) was seeded, respectively, onto pure alginate hydrogels; alginate hydrogels containing PLL, RGD, and fibronectin; and alginate hydrogel modified/bound with RGD. After culturing for 2 days and 7 days, respectively,

images were randomly captured from three areas of each sample to observe cell morphology in 2D culture.

The circularity analysis tool of ImageJ was used to provide a quantitative index of cell shape, where a cell with a perfectly circular outline was assigned a circularity level of 1.0. In each image, individual cells were identified, their shapes were manually traced, and their calculated circularity values were averaged for evaluation.

3.3.6 Evaluation of Schwann cell viability

Schwann cells were added into varying concentrations of RGD-modified alginate hydrogels (1.0%, 1.5%, 2.0% and 2.5%) for both 2D and 3D culture. A Live/dead assay was used to measure cell viability by manually counting the live and dead cells after staining cells with the fluorescent dyes, calcein-AM and propidium iodide, which selectively stain live or dead cells, respectively. A solution of DMEM containing calcein-AM (1 μg/mL) and propidium iodide (10 μg/mL) was added to each well and incubated for, respectively, 20 min in 2D culture and 40 min in 3D culture, both at 37°C. Viability was assessed by counting stained cells on images randomly taken from samples observed with a fluorescence microscope (Carl Zeiss Axiovert 100). For each sample, three random images were taken and analyzed using ImageJ (National Institutes of Health, Bethesda, Maryland, USA), and viability was calculated as a percent of live cells among the total number of live and dead cells.

3.3.7 Evaluation of Schwann cell proliferation

An MTT [3-(4,5-Dimethylthiazol-2-yl)-2,5-diphenyltetrazolium bromide] assay was performed to measure cell number and evaluate cell proliferation [32]. For the cell cultures grown in 96-well plates without hydrogel, 10 μL MTT solution (5 mg/mL) was added to the cell medium and incubated for 3 hours at 37°C; the medium was removed and dimethyl sulfoxide (DMSO) solution (100 uL) was then added to dissolve the formazan precipitate. Absorbance was measured at 555/650 nm using a microplate reader (SpectraMax 250, Molecular Devices, USA).

Before the MTT tests of Schwan cells on or in hydrogels, the relationship between Schwann cell number and MTT absorbance was identified. Briefly, for 96-well plates (100 μL DMSO), cell numbers of 1×10^3, 2×10^3, 4×10^3, 8×10^3, 1.6×10^4 and 3.2×10^4 cells per well were examined, and the correlated average MTT absorbance values were found around 0.05, 0.10, 0.14, 0.22, 0.43, and 0.83 respectively. For 24-well plates (1 mL DMSO), cell numbers of 4×10^3, 8×10^3, 1.6×10^4, 3.2×10^4, 6.4×10^4 and 1.2×10^5 cells per well were checked, and the correlated average MTT absorbance values were found around 0.06, 0.11, 0.21, 0.49, 1.02, and 2.44 respectively. These results showed the linear relation between MTT absorbance and cell numbers, which were used to relate the MTT absorbance to the cell number in the following MTT tests.

MTT assay was applied to measure the cell numbers on Day 1 and Day 2 for cells seeded on alginate-based hydrogels in 96-well plates with different additives. Also, it was used to check the cell proliferation by measuring the cell numbers on Day 2 and Day 7 for both seeded (or 2D) and encapsulated (or 3D) Schwann cell cultures with RGD-modified alginate hydrogels. For the 2D culture, the MTT tests had the same procedure as described above, but was scaled up since the cells were cultured in 24-well plates, where 100 μL MTT reagent was loaded to each well and 1 mL DMSO was added after removing the culture medium 3 hours later. For the 3D culture, modified MTT tests based on the previous study were conducted [32]. Briefly, 100 μL MTT reagent (5 mg/mL) was added to the hydrogels in each well; the medium was aspirated after five hours; and the gels were frozen at -40°C for 24 hours and then freeze-dried for another 24 hours. Upon the completion of dehydration of the alginate gels, 1 mL of DMSO was added to dissolve the formazan precipitate; and absorbance was measured at 555/650 nm using the microplate reader.

3.3.8 Evaluation of Schwann cell protein expression

Immunocytochemistry was employed to investigate cell phenotype with regard to S100 and laminin protein expression at Day 2 and Day 7 in the 2D and 3D Schwann cell cultures. Briefly, cell cultures were rinsed twice with 10 mM TBS (Tris-buffered saline) plus 10 mM calcium chloride, then fixed in 100% methanol (Sigma) for 1 hour. Blocking solution (10 mM TBS + 0.05% Tween 20 + 1% BSA + 3% horse serum + 10 mM calcium chloride) was then added to each well for another 2 hours. After that, primary anti-S100 or

anti-laminin (1:500) was dropped into each well for 2 hours staining for the 2D culture, or 5 hours for the 3D culture. After the primary antibody, samples were washed overnight in 10 mM TBS plus 10 mM calcium chloride plus 0.05% Tween 20 at 4°C. Secondary antibodies AF 488 anti-rabbit IgG or AF 555 anti-rabbit IgG (1:500) with DAPI (1:10,000) were then added for 2 hours (2D) or 5 hours (3D) staining. After another overnight washing, the coverslips were mounted on glass slides using Fluoromount G. Cell circularity was assessed on anti-S100 stained images randomly taken from samples observed with a fluorescence microscope (Zeiss Axioimager M1). For the 3D culture, 5-6 images of the same field were z-stacked for clarity. Fluorescent intensity was measured from anti-laminin stained cells. For each alginate concentration, three samples were prepared, and three random images were taken and analyzed from each sample using ImageJ.

3.3.9 Statistical analysis

The mean values and standard error of the mean (SEM) of all data were calculated. The statistical significance of experimental data was determined by one-way analysis of variance (ANOVA), and pairwise comparisons were performed by the Tukey's test using Graphpad Prism (GraphPad Software, San Diego, CA, USA) with an acceptable significance level of $P < 0.05$.

3.4 Results

The morphology and proliferation of RSC96 immortalized Schwann cells in 2D culture on various alginate-based substrates after 48 hours were examined, with the results presented in Figure 3.1. It is seen that cells seeded on the surface of pure alginate hydrogels were spherical and clustered (Figure 3.1A), which is due to the lack of cell adhesion, as compared the ones on the more adhesive substrate (Figure 3.1B). With the addition of PLL or fibronectin (50 μg/mL for each type), fewer clusters were observed and the quantitative measurement of average cell circularity was found about 0.8 in average (Figures 3.1C and 3.1E), which suggests most of the cells remained nearly spherical. Figure 3.1D and 3.1F show no significant change of cell morphology if a higher concentration (500 μg/mL) of fibronectin or PLL was used. In contest, for the alginate hydrogels with RGD peptide, either mixed or covalently modified, less clustering of cells and more cells with stretched

morphology are seen in the imagines (Figures 3.1G and 3.1H), suggesting that both physically mixed or chemically bonded RGD can promote the cell adhesion.

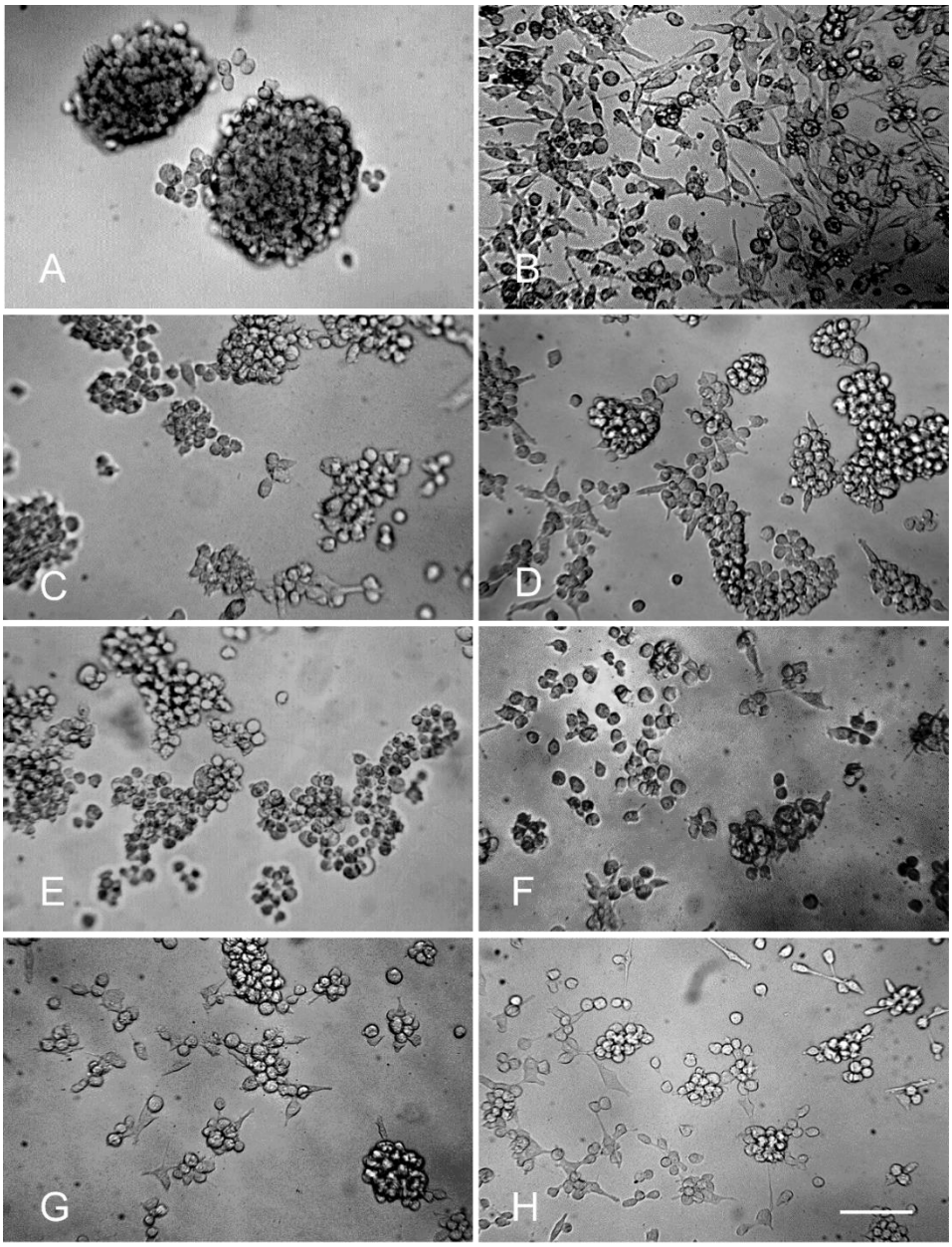

Figure 3. 1 Morphology of RSC96 cells cultured on 2D alginate substrates with different additives after 48 hours. A, negative control (1.5% w/v alginate only); B, positive control (no alginate, PLL coating); C, alginate mixed with 50 μg/mL PLL; D, alginate mixed with 500 μg/mL PLL; E, alginate mixed with 50 μg/mL fibronectin; F, alginate mixed with 500 μg/mL fibronectin; G, alginate mixed with 50 μg/mL RGD peptide; H, RGD-modified alginate (1:250). Scale bar represent 50 μm.

MTT is a colorimetric assay for accessing metabolic activity of cells and thus the number of living cells. With the linear relationship between absorbance and the number of living cells, the reading of absorbance is used for the presentation of living cells in the following. In our study, 2000 cells and 8000 cells were added to each well of a 96-well plate and a 24-well plate, respectively, and the MTT assay was used to evaluate the number of Schwann cells cultured on the hydrogel substrates with the addition PLL, fibronectin, and RGD peptide of varying concentrations. The results illustrate that with the addition of PLL (Figure 3.2B), the peak MTT absorbance takes place at a concentration of 100 and 200 μg/mL among the four concentrations examined; and with addition of fibronectin (Figure 3.2C), the absorbance shows increasing with its concentration varying from 50 to 500 μg/mL; and that with the addition of RGD peptide, the influence of concentration on absorbance is mixed although the four concentrations examined all increases the readings of absorbance of Day 2 as compared to Day 1.

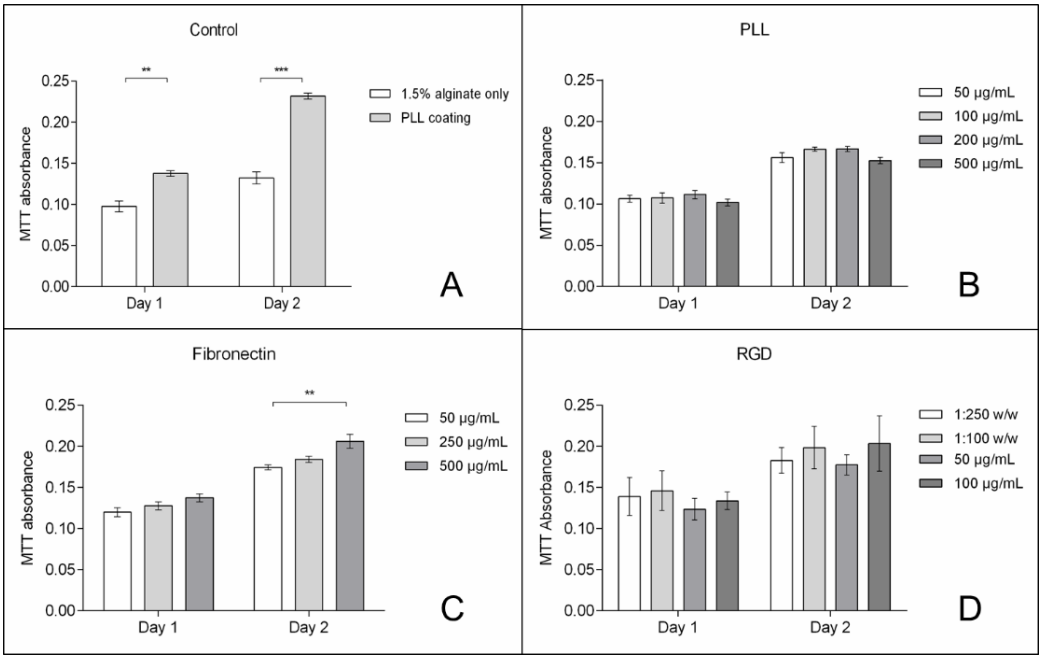

Figure 3. 2 MTT assay for RSC96 cell proliferation with different cell adhesion materials. A, negative control (1.5% alginate only) and positive control (no alginate, PLL coating); B, alginate including PLL; C, alginate including fibronectin; D, alginate including RGD peptide. One-way ANOVA, ∗∗represents $P < 0.01$ and ∗∗∗represents $P < 0.001$

The use of RGD peptide as a cell adhesion additive to alginate hydrogel was further examined by culturing Schwann cells on alginate gels with RGD either mixed or covalently bound, for a time period of 7 days, with the result shown in Figure 3.3. It is seen that most of cells on RGD-mixed alginate after 7 days became more spherical again (Figure 3.3A), while the cells on RGD-modified alginate continued to be of spindle shape (Figure 3.3B). The results of cell circularities (Figure 3.3C) shows that at Day 2, they are at the similar level, around 0.65, for both RGD-mixed and RGD-bound alginate hydrogels, and that at Day 7, however, the cell circularities become much different, with a value of 0.78±0.05 for the RGD-mixed alginate and 0.44±0.03 for RGD-modified alginate. On this basis, RGD-modified alginate hydrogels were selected for the Schwann cell culture in the experiments presented in the following.

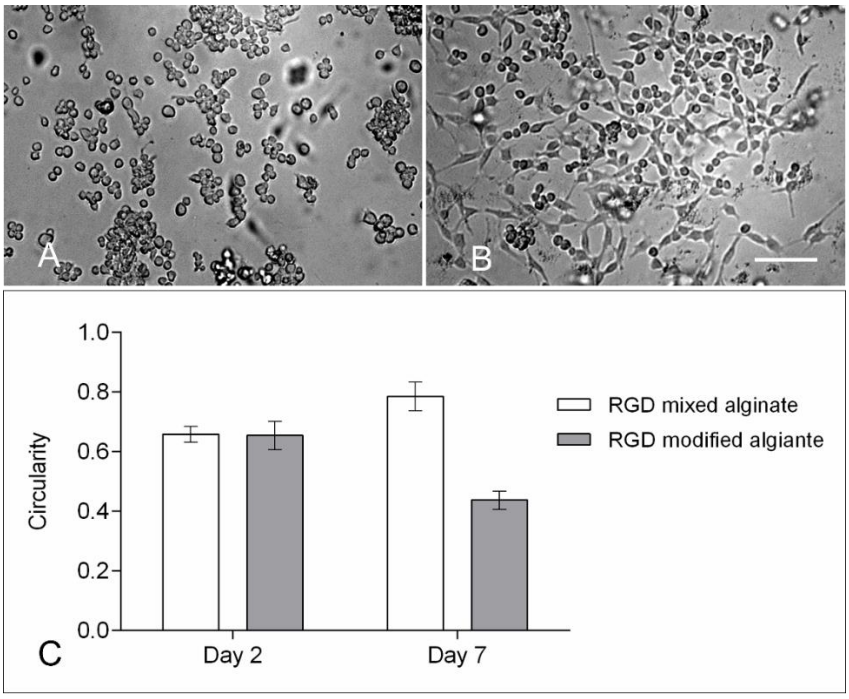

Figure 3. 3 Morphology of RSC96 cells cultured on 2D alginate substrates including RGD peptide after 7 days. A, alginate hydrogel mixed with 100 μg/mL RGD peptide; B, alginate hydrogel covalently modified by RGD peptide (250:1 w/w); C, cell circularity on two different alginate substrates. Scale bar represent 50 μm.

From the compression tests, the curves of strain vs. strain of hydrogels with different concentrations of alginate are presented in Figure 3.4A, which is reproduced in Figure 3.4B for zoomed region to evaluate the Young's moduli. For 1.0%, 1.5%, 2.0%,

and 2.5% alginate hydrogels, the Young's moduli were determined as 1.17±0.48 KPa, 2.62±0.77 KPa, 9.54±1.93 KPa, and 12.53±2.57 KPa, respectively. The result also indicate that Young's modulus increases with the alginate concentration.

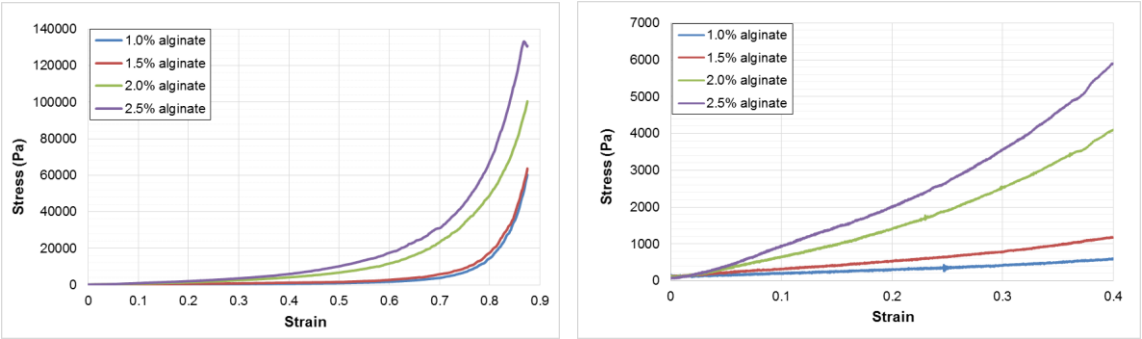

A B

Figure 3. 4 Stress-strain curve of alginate hydrogel with different concentrations. B is reproduced from A with a changed range of strain.

We investigated the performance of Schwann cells seeded on RGD-modified alginate hydrogels with varying stiffness. A live/dead assay was applied to examine the viability of Schwann cells attached to the surface of alginate hydrogel formulated with different concentrations (thus mechanical properties) at Days 1, 2 and 7. Figures 3.5A and 3.5B are the images showing live cells (green) and dead cells (red) on the 1.5 % and 2.5% alginate hydrogels, respectively, suggesting that the most cells survives, and that the number of living cells decreases with the alginate concentration. Live/dead cell counts (Figure 3.5C) shows that the cell viabilities of four alginate groups was all greater than 90%. To examine the cell proliferation, cell number was assessed in 2D cultures using the MTT assay at Day 2 and Day 7 (Figure 3.5D). The readings of MTT absorbance were at the similar level for hydrogels with 1.0% or 1.5% alginate, and since then decreased as the concentration of alginate was increased. This result illustrates that the cell proliferation would prefer on the softer substrates. Also, the lowest absorbance reading was observed from the negative control group (1.5% alginate without RGD peptide), suggesting the positive influence of RGD peptide on the cell proliferation.

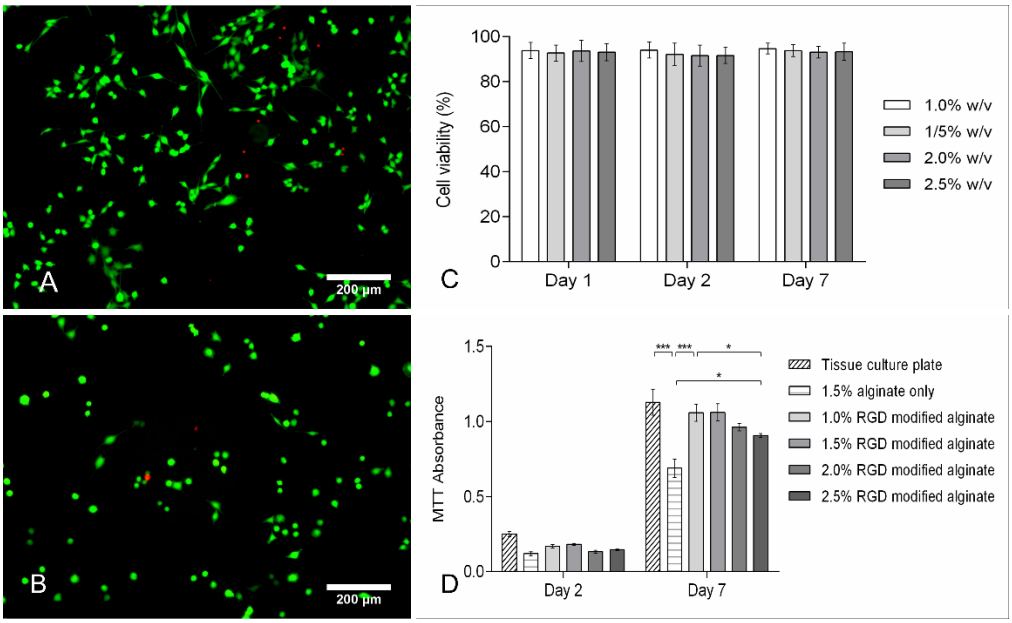

Figure 3. 5 Viability and proliferation of RSC96 seeded on alginate substrates with different stiffness, where a live/dead assay was used to identify live cells by calcein-AM staining (green) and dead cells by propidium iodide staining (red). A, cells on 1.5% alginate hydrogel at Day 2; B, cells on 2.5% alginate hydrogel at Day 2; C, live/dead quantification of cell viability; D, MTT assay of cell proliferation. One-way ANOVA, ∗represents $P < 0.05$ and ∗∗∗represents $P < 0.001$

Immunocytochemical staining was employed to quantitatively investigate cellular performance of Schwann cells in 2D culture on the alginate-based substrates, in terms of their morphological circularity and expression of the ECM protein laminin. The results of of S100 labeled cells (Figures 3.6A, 3.6B and 3.6C) revealed that circularity values were increased as the alginate hydrogel became stiffer. For example, the average cell circularity values on 1.5% and 2.5% alginate surface were 0.72±0.08 and 0.81±0.05 at Day 2, and were 0.65±0.05 and 0.73±0.04 at Day 7, respectively. The statistical result confirmed that spreading of Schwann cells can be altered by regulating the mechanical stiffness of alginate substrates, and that cells preferred soft alginate hydrogels with a Young's modulus in a range from 1.17 to 2.62 KPa.

Analysis of protein expression of anti-laminin stained cells (Figures 3.6D, 3.6E and 3.6F) showed that at both Days 2 and 7, the expression of laminin intensity decreases as the alginate concentration increases in a nonlinear pattern. It is also noticed that at the

alginate concentration of 2.5%, the laminin expression by cells decreases to a level that is significantly lower than the one of other concentrations. Overall, the result suggested a negative effect of higher stiffness on the Schwann cells' expression of the ECM protein laminin.

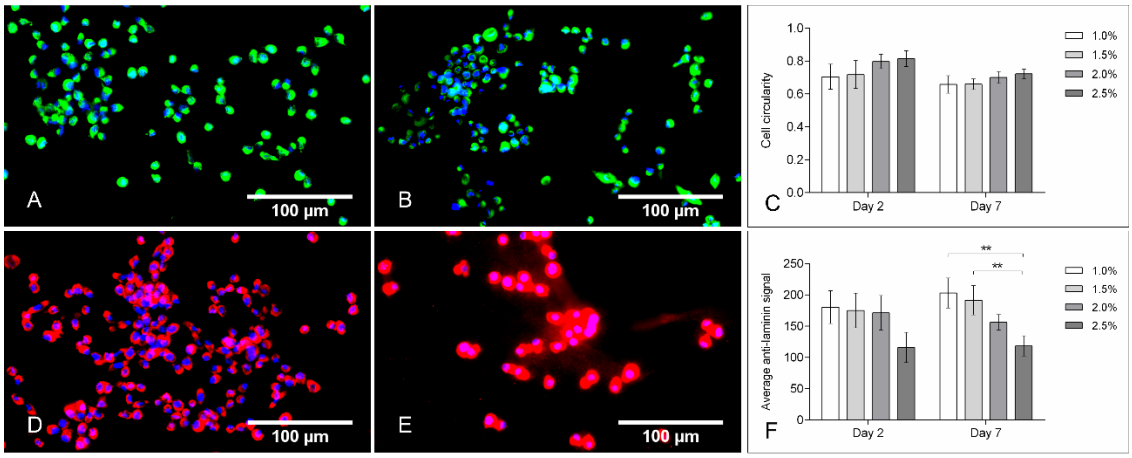

Figure 3. 6 Immunocytochemical staining for RSC96 cells seeded on alginate hydrogels in 2D culture. A and B, cells on 1.5% and 2.5% alginate hydrogels stained by anti-S-100 after 2 days; C, cell circularity analysis of S100 stained cells; D and E, RSC96 cells seeded on 1.5% and 2.5% alginate hydrogels stained by anti-laminin after 2 days; F, quantitative analysis of laminin expression. One-way ANOVA, ∗∗represents $P < 0.01$.

Through 3D culture, we also examined the performance of Schwann cells that were encapsulated within alginate hydrogels. The viability of cells in 3D culture was investigated at Days 1, 2 and 7 (Figures 3.7A, 3.7B and 3.7C). Microscopic observation revealed that propidium iodide-labeled dead cells were fewer in 3D culture, at all alginate concentrations tested over 7 days (Figure 3.7C), and the percentage of cell viability for all four alginate groups was all greater than 90%. From images 3.7A and 3.7B it was noticed that many cells clustered in 3D culture, which differed from the observations in 2D culture. Furthermore, cell clustering became more prominent as the concentration of alginate increased.

We investigated cell proliferation in 3D culture as a function of gel stiffness using the modified MTT assay. Cell-number changes in 3D culture shared a similar trend with those in 2D culture, i.e., decreasing with the concentration in a nonlinear pattern (Figure 3.7D). It is also noticed that a significant decrease takes place if the concentrations is

changed from 1.5% to 2.0% (Figure 3.7D), indicating better cell proliferation taken place in softer gels. Figure 3.7D also demonstrates that Schwann cells were quite sensitive to the covalent-bound RGD peptide, since the cell number in 1.5% pure alginate hydrogel was much less than the one in the RGD-bound alginate hydrogels after 7 days. Compared with 2D culture (Figure 3.5), the values of MTT absorbance for 3D culture were similar at 1.0% and 1.5% alginate hydrogels (Figure 3.7), however the values for 2D seeded cells was much higher than those for 3D encapsulated cells after 7 days, at the alginate concentration of 2.5%. Taken together, these results illustrate the negative effect of cell substrate stiffness on cell proliferation is stronger if Schwann cells are encapsulated within the hydrogel as compared to those seeded on the surface of hydrogel.

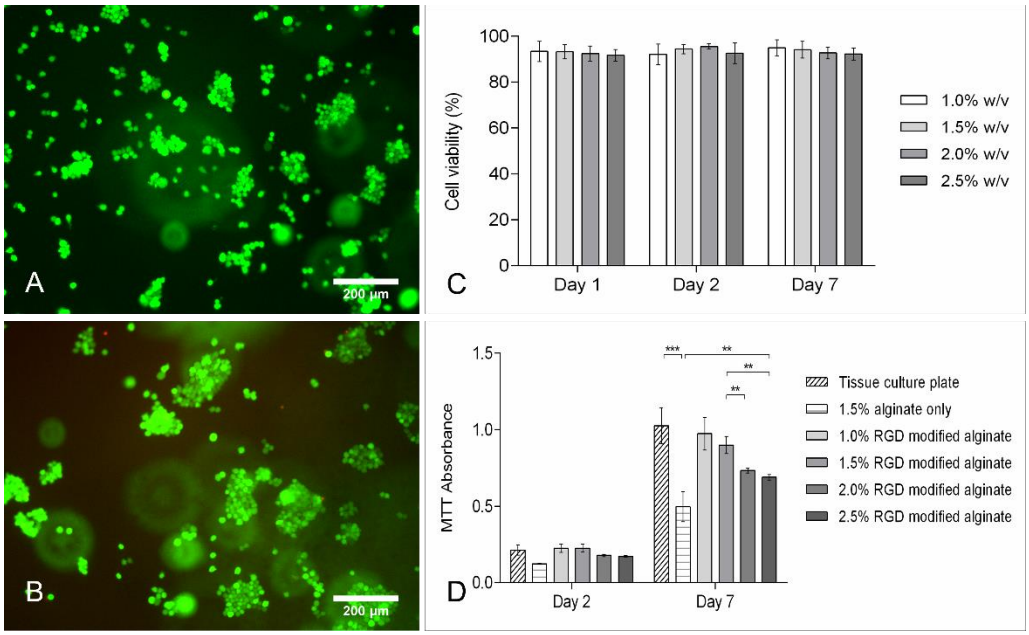

Figure 3. 7 Viability and proliferation of RSC96 encapsulated in alginate substrates with different stiffness. A live/dead assay was used to identify live cells by calcein-AM staining (green) and dead cells by propidium iodide staining (red). A, cells in 1.5% alginate hydrogel after 7 days; B, cells in 2.5% alginate hydrogel after 7 days; C, live/dead quantification of cell viability; D, MTT assay of cell proliferation. One-way ANOVA, ∗∗represents $P < 0.01$ and ∗∗∗represents $P < 0.001$

Anti-S100 staining and measurement of Schwann cell circularity in 3D culture was conducted at Days 2 and 7. A more spherical morphology was observed in 3D culture in the images (Figures 3.8A and 3.8B) as compared in 2D culture (Figure 3.6A and 3.6B),

which is also seen from the calculated cell circularity (Figures 3.8C and 3.6C). Furthermore, it was noticed that higher alginate concentration led to bigger and more cell clusters (Figure 3.8C), indicating that cell extension within the hydrogel can also be affected by the stiffness of gel.

The analysis of protein expression (Figures 3.8D, 3.8E, and 3.8F) demonstrated the same trend of laminin intensity in 3D culture as seen in 2D culture at Day 2 and 7 (Figure 3.6F). The laminin staining intensity was stronger if cells were cultured in 1.0% and 1.5% alginate hydrogels, then sharply decreased as alginate concentration further increased. For example, from Figure 3.8F, the value of laminin staining intensity per cell in 2.5% alginate hydrogel was 47.72% less than that seen in 1.0% alginate at Day 7, suggesting a negative effect of higher stiffness on the extracellular deposition of laminin by encapsulated cells.

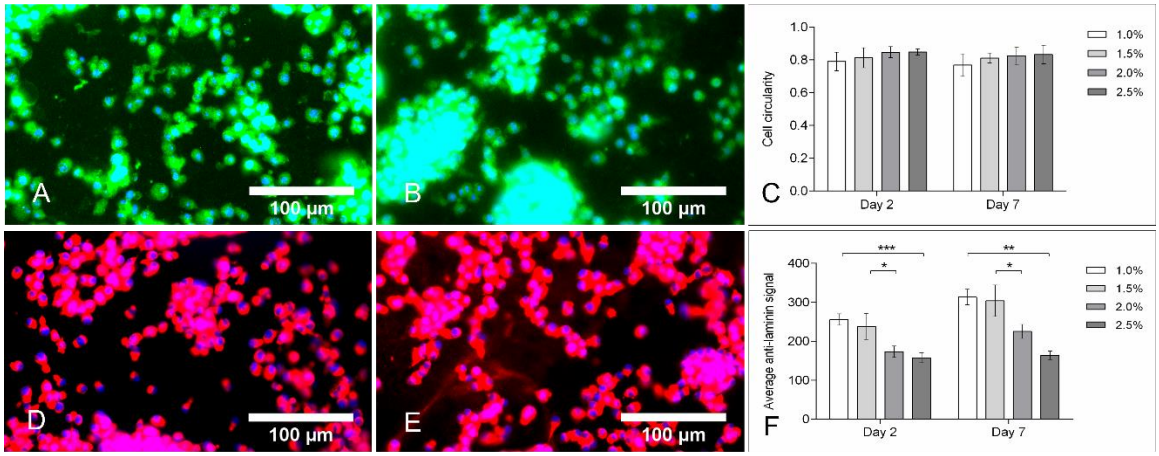

Figure 3. 8 Immunocytochemical staining for RSC96 cells encapsulated in alginate hydrogels in 3D culture. A and B, cells on 1.5% and 2.5% alginate hydrogels stained by anti-S100 after 7 days; C, cell circularity analysis of S100 stained cells; D and E, RSC96 cells encapsulated in 1.5% and 2.5% alginate hydrogels stained by anti-laminin after 7 days; F, quantitative analysis of laminin expression. One-way ANOVA, ∗represents $P < 0.05$, ∗∗represents $P < 0.01$ and ∗∗∗represents $P < 0.001$

3.5 Discussion

Recent sophisticated strategies such as 3D bio-printing enable fabrication of tissue scaffolds with incorporated living cells to more closely resemble tissues or organs, since high cell density with controlled distributions in biomaterials can be achieved in the

printing process [32-35]. Bio-fabrication of tissue scaffolds that contain living cells is a complex undertaking with many parameters to harmonize, such as the type of biomaterial, crosslinking technique, cell type, and fabrication process. Appropriate biomaterials are fundamental for tissue scaffolds to provide cells with an appropriate microenvironment containing cell-specific cues to promote cell health and function [36-38]. In addition to biochemical factors, these cues can include physical properties such as adhesive cues and mechanical stimuli, both of which can affect cell survival and regeneration significantly [39-41].

Schwann cells, the major glial cells for peripheral nervous system, have been widely used for nerve repair and regeneration [42, 43]. In the intact nerve, they wrap myelin around the axons, and provide other supportive roles. Following injury, they become mobilized to produce ECM and various growth factors to promote axonal growth. Spindle-like stretched Schwann cells in shape with high proliferation rates are sought in culture or implantation, which can improve their *in vivo* behavior to produce such ECM proteins as laminin and neural growth factors for promoting axon growing. Because of source tissue and tissue culture heterogeneity in the isolation of primary Schwann cells, a clearer understanding of Schwann cell biology might be obtained from an immortalized Schwann cell line that can be cultured more consistently [44]. Thus, the immortalized Schwann cell line RSC96 was selected for this study. Alginate was applied as the main cell substrate biomaterial because of its fast gelation ability during scaffold fabrication, which provides the mechanical support to ensure the integrity of produced constructs. However, alginate alone is not suitable for Schwann cells as it lacks biochemical cell adhesive properties. In order to improve alginate adhesion characteristics, PLL, fibronectin, and RGD peptide were examined as additives to alginate in the present study.

The mechanical properties of hydrogels have significant impact on cell behavior, including the extension of axons [24], Schwann cell proliferation and the expression of cellular proteins [25]. The stiffness of hydrogels can be tuned by adjusting its concentration and the molecular weight, or the density of crosslinking agent [27]. For alginate hydrogel, more alginate-calcium bonds are formed if alginate concentration became higher, which would reduce the porosity and diffusion of alginate hydrogel structure and thus increase its stiffness. In this study, compressive tests were used to evaluate the elasticity of the

substrates of varying alginate concentrations, from 1.0% to 2.5%. It is noted that in our scaffold fabrication, if the concentration of alginate is lower 1.0%, it is hard to fabricate scaffolds with the structure integrity. Thus, 1.0% alginate was used here as the lowest concentration. In this study, RCS96 Schwann cells were cultured on either the surface or inside of the alginate substrates; and cell viability, proliferation and phenotype were investigated using the live/dead assay, the MTT assay, and morphological and immunocytochemical analysis, respectively. Our studies of Schwann cells indicated that softer alginate hydrogels (Young's modulus range from 1.17 to 2.62 KPa) with covalently-bound RGD peptide promoted good cell performance and could be selected as suitable substrates for bio-printing peripheral nerve repair scaffolds.

For analysis of cells in 3D cultures, the standard MTT assay has an issue given that the hydrogel structure could impede reagent availability and thus affect the results. In order to address this issue, ethylenediaminetetraacetic acid (EDTA) or sodium citrate solution have been used previously to dissolve alginate hydrogels so as to release cells [12, 45]. However, these chemical components may stimulate reactions and change the color of cell suspensions. In this study, we modified MTT method for 3D cell culture as follows. Cell substrates were lyophilized, during which the formazan produced by cells was kept the same as the one before lyophilization; and then the formazan was dissolved using DMSO, leaving the dried and porous alginate behind.

RGD peptide, corresponding to integrin recognition sites in fibronectin [25], was first simply mixed into alginate in our experiments. The result showed that most cells had spindle-like shapes in the presence of 100 μg/mL RGD after 2 days, similar to Schwann cells cultured on tissue culture treated surfaces. This indicated that addition of RGD peptide promotes cell adhesion. However, when the culture period was extended to 7 days, most of cells became more spherical again. This is probably caused by the leaking of RGD peptide from hydrogel due to the daily medium changes. Previous study showed extensive myoblast spreading if cultured on the surface of RGD covalently-modified alginate hydrogel [12]. The highest efficiency of RGD-alginate bond formation was found when the pH of the reaction solution was around 6.5. Compared with the RGD mixing alginate, chemically-modified alginate by RGD peptide in this study appeared to be much better for promoting Schwann cell phenotype. As a result, RGD-modified alginate was selected as

cell the substrate in our experiments to test the influence of mechanical properties on cell performance.

Results in this study confirmed that more Schwann cells are generated if more fibronectin was added. However most of the cells remained spherical and did not exhibit their expected bipolar morphology. This is probably because of the inherent hydrophilicity of alginate hydrogels that prevents the attachment of Schwann cells [46]. Increased density of fibronectin in alginate is believed to have positive effects on Schwann cells stretching, because more integrin binding sites are involved [31]. However, since the amount of RGD sequence in fibronectin is much lower than derived RGD peptide solution at the same density, a significantly higher concentration of fibronectin would be needed for improvement of cell adhesion, increasing the cost. Some studies also show that it is more favorable to apply cell adhesion ligands rather than a whole protein because smaller peptides can sustain their bioactivities in the harsh processing conditions [24]. The artificial polypeptide PLL is commonly used to promote cell attachment in culture due to its positive charge property. Mixing PLL in alginate hydrogels showed limited improvement of cell proliferation, and even a negative effect was found as the concentration of PLL reached 500 μg/mL. This may be due to the toxicity of PLL itself for cells.

To explore the effects of hydrogel stiffness on Schwann cell, the performance of cell in both 2D and 3D cultures was examined by varying the concentration of alginate. It was found that alginate hydrogels with relatively low Young's modulus (1.17 KPa to 2.62 KPa) led to higher Schwann cell proliferation, good cell morphology and protein expression, showing the consistency with the previous study [46]. The viabilities of Schwann cells for both 2D and 3D culture are consistently high in our study, demonstrating that alginate hydrogel is compatible with cell survival. Proliferation analysis shows that no significant difference between 2D and 3D cell cultures if the elasticity of substrate is less than 2.62 KPa, and that the cell proliferation becomes less active in 3D culture at Day 7 as more alginate is included.

Cell circularity values of S100 stained cells increased as alginate hydrogels became stiffer in both 2D and 3D cultures. Interestingly, the values of cell circularity from optical microscopic examination are less than those from florescent immunocytochemical analysis for the same samples, which is likely due to the different operating processes of these two

tests. For optical images, cells were alive in culture medium with a temperature of around 37°C, while for florescent pictures, cells were rinsed in buffer at room temperature then chemically fixed, which would cause cells to shrink and increase their circularity.

Expression of ECM protein laminin by Schwann cells shares a similar trend in both 2D and 3D cultures, i.e., the florescent intensity rapidly goes down as the stiffness exceeds 2.62 KPa. It is likely that Schwann cells are able to sense the elasticity of their substrates through their adhesion receptors during growth, and that relatively high stiffness may restrict laminin expression capacity [31]. Cell metabolism and protein expression can be influenced by signals that they receive from each other and from the ECM. As higher concentrations of alginate are used, more alginate/calcium crosslinking occurs, leading to lower porosity and lower diffusion within the alginate hydrogel, which may block signal transmission to cells.

Unexpectedly cell clusters were found after 2 days and 7 days in all 3D cultures using both the live/dead assay and immunocytochemical visualization. The situation was improved as less alginate was used, suggesting that lower alginate concentration may be more beneficial for cell spreading. Similarly, proliferation was higher in softer gels used for 3D culture. However, alginate solutions of less than 1% cannot easily be printed into well-defined structures using the post-extrusion calcium gelation technique based on our preliminary bioprinting experiences. On the other hand, when the substrate is too stiff, cells experience higher mechanical restriction leading to lower metabolic performance. Thus a trade-off between the structural stable and Schwann cell performance should be carefully considered in the design of tissue scaffolds for peripheral nerve regeneration. Taken together, our present results suggest that 1.0 – 1.5% alginate solutions may be the best for the fabrication of scaffolds under the light of aforementioned trade-off consideration.

3.6 Conclusions

This chapter presents our study on the influence of mechanical properties on the Schwann cell performance including cell, viability, proliferation, morphology and cellular protein expression and further illustrates that the Schwann cell performance can be regulated by the tunable stiffness of alginate-hydrogel substrates. Several cell adhesive additives including PLL, fibronectin, and RGD peptides with various concentrations were

investigated and among them, alginate hydrogels covalently-modified with RGD peptide were determined to be the most appropriate substrate for promoting Schwann cell attachment and proliferation due to the level of cell spreading. The influence of the mechanical properties of alginate-based hydrogel on cell performance was evaluated and a suitable range of concentration of alginate with the associated stiffness was suggested for used in tissue repair scaffolds with living Schwann cells. Our results illustrate cell survival and phenotype can be controlled and promoted by appropriate biological and mechanical properties of substrates. The data collected in this study also provide useful specific information for future design of Schwann cell encapsulated scaffolds for nerve tissue engineering.

3.7 References

[1] Langer R, Vacanti JP. Tissue engineering. *Science.* 1993;260:920-926.

[2] Drury JL, Mooney DJ. Hydrogels for tissue engineering: scaffold design variables and applications. *Biomaterials.* 2003;24:4337-4351.

[3] Griffith LG, Naughton G. Tissue engineering--current challenges and expanding opportunities. *Science.* 2002;295:1009-1014.

[4] Murphy SV, Atala A. 3D bioprinting of tissues and organs. *Nat Biotechnol.* 2014;32:773-785.

[5] Bajaj P, Schweller RM, Khademhosseini A, et al. 3D biofabrication strategies for tissue engineering and regenerative medicine. *Annu Rev Biomed Eng*. 2014;16:247-276.

[6] Lu T, Li Y, Chen T. Techniques for fabrication and construction of three-dimensional scaffolds for tissue engineering. *Int J Nanomedicine*. 2013;8:337-350.

[7] Hoque ME, Chuan YL, Pashby I. Extrusion based rapid prototyping technique: an advanced platform for tissue engineering scaffold fabrication. *Biopolymers*. 2012;97:83-93.

[8] Li M, Tian X, Chen X. A brief review of dispensing-based rapid prototyping techniques in tissue scaffold fabrication: role of modeling on scaffold properties prediction. *Biofabrication*. 2009;1:032001.

[9] Murphy SV, Skardal A, Atala A. Evaluation of hydrogels for bio-printing applications. *J Biomed Mater Res A*. 2013;101:272-284.

[10] Christensena BE. Alginates as biomaterials in tissue engineering. Carbohydrate Chemistry: *Chemical and Biological Approaches*. 2011;37:227-258.

[11] Mosahebi A, Simon M, Wiberg M, et al. A novel use of alginate hydrogel as Schwann cell matrix. *Tissue Eng*. 2001;7:525-534.

[12] Rowley JA, Madlambayan G, Mooney DJ. Alginate hydrogels as synthetic extracellular matrix materials. *Biomaterials*. 1999;20:45-53.

[13] Kundu J, Shim JH, Jang J, et al. An additive manufacturing−based PCL-alginate-chondrocyte bioprinted scaffold for cartilage tissue engineering. *J Tissue Eng Regen Med.* 2013.

[14] Sapir Y, Cohen S, Friedman G, et al. The promotion of in vitro vessel-like organization of endothelial cells in magnetically responsive alginate scaffolds. *Biomaterials*. 2012;33:4100-4109.

[15] Hunt NC, Shelton RM, Henderson DJ, et al. Calcium-alginate hydrogel-encapsulated fibroblasts provide sustained release of vascular endothelial growth factor. *Tissue Eng Part A*. 2012;19:905-914.

[16] Macaya D, Spector M. Injectable hydrogel materials for spinal cord regeneration: a review. *Biomed Mater*. 2012;7:012001.

[17] Struzyna LA, Katiyar K, Cullen DK. Living scaffolds for neuroregeneration. *Curr Opin Solid State Mater Sci.* 2014;18:308-318.

[18] Siriwardane M, DeRosa K, Pfister B. Collagen-based fiber-gel constructs engineered for schwann cell guidance and adult axon growth. *Bioengineering Conference (NEBEC)*, IEEE 37th Annual Northeast; 2011 Apr 1-3; NY, USA.

[19] Rajaram A, Schreyer D, Chen D. Bioplotting alginate/hyaluronic acid hydrogel scaffolds with structural integrity and preserved schwann cell viability. *3D Print Addit Manuf*. 2014;1:194-203.

[20] Comisar WA, Hsiong SX, Kong HJ, et al. Multi-scale modeling to predict ligand presentation within RGD nanopatterned hydrogels. *Biomaterials.* 2006;27:2322-2329.

[21] Yu TT, Shoichet MS. Guided cell adhesion and outgrowth in peptide-modified channels for neural tissue engineering. *Biomaterials.* 2005;26:1507-1514.

[22] Kuzmenko V, Sämfors S, Hägg D, et al. Universal method for protein bioconjugation with nanocellulose scaffolds for increased cell adhesion. *Mater Sci Eng C*. 2013;33:4599-4607.

[23] Ricks CB, Shin SS, Becker C, et al. Extracellular matrices, artificial neural scaffolds and the promise of neural regeneration. *Neural Regener Res*. 2014;9:1573-1577.

[24] Gunn JW, Turner SD, Mann BK. Adhesive and mechanical properties of hydrogels influence neurite extension. *J Biomed Mater Res A*. 2005;72:91-97.

[25] Novikova LN, Mosahebi A, Wiberg M, et al. Alginate hydrogel and matrigel as potential cell carriers for neurotransplantation. *J Biomed Mater Res A*. 2006;77:242-252.

[26] Even-Ram S, Artym V, Yamada KM. Matrix control of stem cell fate. *Cell*. 2006;126:645-647.

[27] Huang G, Wang L, Wang S, et al. Engineering three-dimensional cell mechanical microenvironment with hydrogels. *Biofabrication.* 2012;4:042001.

[28] Discher DE, Janmey P, Wang Yl. Tissue cells feel and respond to the stiffness of their substrate. *Science.* 2005;310:1139-1143.

[29] Shim JH, Lee JS, Kim JY, et al. Bioprinting of a mechanically enhanced three-dimensional dual cell-laden construct for osteochondral tissue engineering using a multi-head tissue/organ building system. *J Micromech Microeng*. 2012;22:085014.

[30] Schuurman W, Khristov V, Pot M, et al. Bioprinting of hybrid tissue constructs with tailorable mechanical properties. *Biofabrication.* 2011;3:021001.

[31] Cao N, Chen XB, Schreyer DJ, Influence of calcium ions on cell survival and proliferation in the context of an alginate hydrogel. *ISNR Chem Eng*. 2012;2012:1-9

[32] van Meerloo J, Kaspers GJ, Cloos J. Cell sensitivity assays: the MTT assay. *Cancer Cell Culture.* Springer; 2011. p. 237-245.

[33] Orive G, Hernández RM, Gascón AR, et al. Cell encapsulation: promise and progress. *Nat Med.* 2003;9:104-107.

[34] Chang Yan K, Nair K, Sun W. Three dimensional multi-scale modelling and analysis of cell damage in cell-encapsulated alginate constructs. *J Biomech.* 2010;43:1031-1038.

[35] Kang A, Park J, Ju J, et al. Cell encapsulation via microtechnologies. Biomaterials. 2014;35:2651-2663.

[36] Park JY, Choi JC, Shim JH, et al. A comparative study on collagen type I and hyaluronic acid dependent cell behavior for osteochondral tissue bioprinting. *Biofabrication.* 2014;6:035004.

[37] Xu B, Chow M-J, Zhang Y. Experimental and modeling study of collagen scaffolds with the effects of crosslinking and fiber alignment. *Int J Biomater.* 2011;2011:172389.

[38] Dash M, Chiellini F, Ottenbrite R, et al. Chitosan-A versatile semi-synthetic polymer in biomedical applications. *Prog Polym Sci.* 2011;36:981-1014.

[39] Lee H, Kim G. Enhanced cellular activities of polycaprolactone/alginate-based cell-laden hierarchical scaffolds for hard tissue engineering applications. *J Colloid Interface Sci.* 2014;430:315-325.

[40] Little CJ, Bawolin NK, Chen X. Mechanical properties of natural cartilage and tissue-engineered constructs. *Tissue Eng Part B Rev.* 2011;17:213-227.

[41] Pulieri E, Chiono V, Ciardelli G, et al. Chitosan/gelatin blends for biomedical applications. *J Biomed Mater Res A*. 2008;86:311-322.

[42] Kijeńska E, Prabhakaran MP, Swieszkowski W, et al. Interaction of Schwann cells with laminin encapsulated PLCL core-shell nanofibers for nerve tissue engineering. *Eur Polym J*. 2014;50:30-38.

[43] Goto E, Mukozawa M, Mori H, et al. A rolled sheet of collagen gel with cultured Schwann cells: model of nerve conduit to enhance neurite growth. *J Biosci Bioeng.* 2010;109:512-518.

[44] Ji Y, Shen M, Wang X, et al. Comparative proteomic analysis of primary schwann cells and a spontaneously immortalized schwann cell line RSC 96: a comprehensive overview with a focus on cell adhesion and migration related proteins. *J Proteome Res.* 2012;11;3186-3198.

[45] Tritz J, Rahouadj R, de Isla N, et al. Designing a three-dimensional alginate hydrogel by spraying method for cartilage tissue engineering. *Soft Matter.* 2010;6:5165-5174.

[46] Gu Y, Ji Y, Zhao Y, et al. The influence of substrate stiffness on the behavior and functions of Schwann cells in culture. *Biomaterials.* 2012;33:6672-6681.

CHAPTER 4

Characterization of Flow Behavior of Alginate-Cell Suspensions and the Influence of Shear Stress on Cell Viability and Proliferation

This chapter has been published as "Liqun Ning, Arther Guillemot, Jingxuan Zhao, Georges Kipouros, and Xiongbiao Chen, Influence of flow behavior of alginate-cell suspensions on cell viability and proliferation. *Tissue Engineering, Part C Method. 2016, 22, 652-662*" According to the Copyright Agreement, "the authors retain the right to include the journal article, in full or in part, in a thesis or dissertation".

4.1 Abstract

Tissue scaffolds with living cells fabricated by three-dimensional bioprinting/plotting techniques are becoming more prevalent in tissue repair and regeneration. In the bioprinting process, cells are subject to process-induced stresses (such as shear stress) that can result in cell damage and loss of cell function. The flow behavior of the biomaterial solutions that encapsulate living cells in this process plays an important role. This study used a rheometer to examine the flow behavior of alginate solution and alginate-Schwann cell (RSC96), alginate-fibroblast (NIH-3T3), and alginate-myoblast (L8) suspensions during shearing with respect to effects on cell viability and proliferation. The flow behavior of all the alginate-cell suspensions varied with alginate concentration and cell density and had a significant influence on the viability and proliferation of the cells that exposed to shear stress as well as on the recovery of cells. These findings provide a mean to preserve cell viability and/or retain cell proliferation function in the bioprinting process by regulating the flow behavior of cell-biomaterial suspensions and process parameters.

4.2 Introduction

Biomimic scaffolds have emerged as a method for tissue repair and regeneration in tissue engineering [1-3]. Among the techniques for fabricating these biomimic scaffolds, 3D bioprinting/plotting is promising due to its versatile features that can be used to generate organized living tissue constructs in a controllable and repeatable manner [4-6], which would be impossible using traditional approaches [7-9]. Dispensing-based bioprinting, in

which a pneumatic or other volumetrically driven extruder is used to apply biomaterials or biomaterial-cell mixtures, is one of the most promising methods due to its efficient material manipulation with high printing resolution [10-12]. The mild conditions used in dispensing-based bioprinting also enable cells to be incorporated within the biomaterial solutions for scaffold fabrication [13-15]. However, dispensing-based bioprinting still faces several challenges, such as achieving the scaffold structures as designed [16,17], promoting the formation of artificial vascularization within scaffolds [18,19], manipulating multi materials/cells for mimicking natural tissues [20–23], and retaining the function of the cells incorporated or encapsulated during scaffold fabrication [24,25]. Understanding the flow behavior of biomaterial solutions and how it influences the bioprinting process is essential to address these issues [26,27].

In the bio-printing process, the biomaterials selected for cell encapsulation facilitate the transport of necessary nutrients without causing an immunoreaction from the host after implantation [28]. However, encapsulating cells into biomaterials in the bio-printing process is challenging because the cells are subjected to process-induced stresses, such as shear stress, that may cause cell damage and thus loss of cell functions [29]. Billiet et al. report that printing pressure and needle geometry used in a cell-laden scaffold fabrication process play important roles in the viability of blended cells (hepatocarcinoma cells) because both factors affect the shear stress induced as well as the time period that cells are exposed to shearing (i.e., the exposure time) [30]. They also noticed that the density of blended cells affects the apparent viscosity of the medium, but unfortunately were not able to quantitatively examine the relationship between shear stress/exposure time and cell viability or the influence of cell density on cell viability. While previous investigations show that cell damage occurring in printing/plotting depends upon cell manipulation parameters, temperature, and needle geometry [31-33], a comprehensive investigation into cell viability and proliferation as well as their correlation to the flow behavior of biomaterial solutions has yet to be conducted.

Process-induced stresses that cells experience in bio-printing cause the deformation of the cell structure and, as a result, can rupture the cell membrane or cytoskeleton if the stress and/or expose time exceed certain thresholds [34]. Following bio-printing, some cells have the ability to recover from the damage caused by process-induced

stresses [35,36]. However, most investigations have focused on cell survival in the bio-printing process [37-39] with few reports on cell recovery thereafter. In addition, the process-induced stresses can affect cell growth or proliferation even after they are removed; this is of importance for the ensuing tissue repair and regeneration and highlights the need to investigate cell viability and proliferation subsequent to the bio-printing process.

This chapter presents a comprehensive study of cell viability and proliferation during and after the shear stress that cells experience during bio-printing. Alginate was chosen as the biomaterial for cell encapsulation and three different types of cells, Schwann cell line RSC96, fibroblast cell line, NIH-3T3, and myoblast cell line L8 were selected due to their common use in tissue engineering. Experiments to examine flow behavior were designed and conducted using alginate solutions of varying concentrations and featuring varying cell types and densities. Experiments aimed at examining the effects of shear stress on cell damage were also carried out, with the percent cell damage measured and quantified as a function of shear stress, exposure time, and cell density. Cells from both sheared and non-sheared suspensions were cultured and their ability to recover and proliferate over a 48 h time frame was evaluated. The results of this study inform methodologies for regulating the flow behavior of biomaterial solutions to preserve cell viability and/or retain cell function during and after the bio-printing process.

4.3 Methods

4.3.1 Cell culture

The Schwann cell line (RSC96), fibroblast cell line (NIH-3T3), and myoblast cell line (L8) purchased from American Type Culture Collection (Manassas, VA, USA) were maintained in a humidified incubator at 37 °C, with a 5% CO_2 atmosphere and standard Dulbecco's Modified Eagle's Medium (DMEM) (Sigma-Aldrich, Oakville, ON, Canada) supplemented with 10% fetal bovine serum (FBS) (GIBCO, Life Technologies, Burlington, ON, Canada) for culturing.

4.3.2 Materials

Sodium alginate of medium viscosity (Sigma-Aldrich, Alginic acid sodium salt from brown algae, A2033, Canada) was thoroughly dissolved in calcium-free DMEM

(Gibco, Thermo Fisher Scientific, USA) to create a 4.0% w/v alginate stock solution for the flow behavior tests. To prepare alginate solutions for the cell recovery tests, sodium alginate was first dissolved in deionized water to form a 0.2% w/v solution. A 0.22 μm bottle-top filter (Thermo Scientific, Ann Arbor, MI, USA) was used to sterilize the alginate solution. The filtered medium was then removed to a -40 °C freezer for 24 h and later freeze-dried (FreeZone freeze dryer, Labconco, USA) under sterile conditions for 72 h. The freeze-dried alginate was dissolved again in calcium-free DMEM with 1.0% anti-biotic (Penicillin 100x, Sigma-Aldrich, Canada) to achieve a 2.5% w/v alginate stock solution. MTT [3-(4,5-dimethylthiazol-2-yl)-2,5-diphenyltetrazolium bromide] powder purchased from Sigma-Aldrich (Canada) was dissolved and filter sterilized to obtain a 5 mg/mL solution in 10 mM PBS. Calcein-AM, propidium iodide, and Hoechst stain were purchased from AnaSpec (Freemont, CA, USA). Trypan blue was purchased from Sigma-Aldrich (Canada).

4.3.3 Characterization of flow behavior

4.3.3.1 Influence of alginate concentration and temperature on flow behavior

Alginate solution flow behavior was characterized on a rheometer with a cone-and-plate geometry and a CP-41 spindle (RVDV-III, Brookfield, USA) (Figure 4.1A). For each test, 2 mL of alginate solution of various concentrations (1.0, 2.0, 3.0, and 4.0% w/v, respectively) were loaded into the gap between the cone and plate (Figure 4.1B). During the shear process, the cone is programmed to rotate at preset speeds and the shear stress applied to the sample is recorded. To evaluate the influence of temperature on the flow behavior, shearing experiments for all alginate solutions were conducted at temperatures of 15, 20, 25, 30, 35, and 40 °C controlled using a water bath (TC-102 calculating water bath, Brookfield, USA). For each condition, five samples were sheared and the average thereof is reported herein.

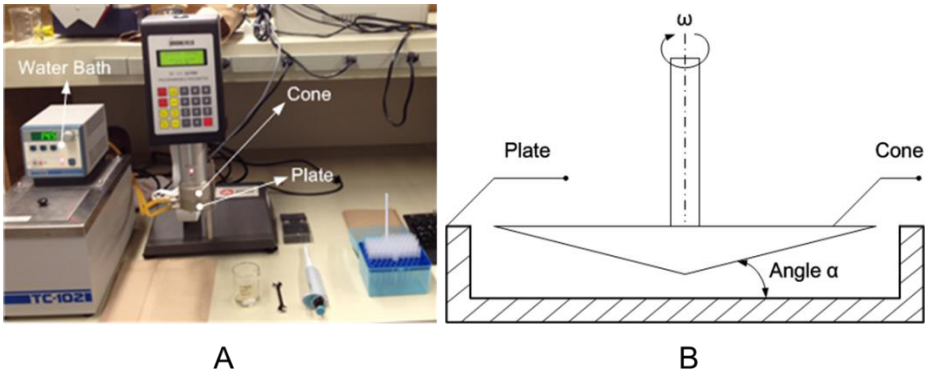

Figure 4. 1 Schematic of rheometer. A, the device and tools; B, applied cone and plate of rheometer

4.3.3.2 Influence of cell densities on flow behavior

RSC96, NIH-3T3, and L8 cells were each mixed by pipette with a 1.0% alginate solution to obtain uniform cell suspensions with cell densities of 5×10^5, 1×10^6, 5×10^6, and 1×10^7 cells/mL. Before this step, detached cells in a 50 mL plastic tube were centrifuged for 5 min and the standard DMEM with 10% FBS was then replaced by calcium-free DMEM so as to avoid gelation of alginate by calcium ions. A 2 mL alginate-cell suspension was loaded into the rheometer to test the flow behavior at different shear rates. For all three kinds of cells, the experiment for each cell density was repeated five times at room temperature.

4.3.4 Characterization of cell damage under shearing

4.3.4.1 Influence of alginate concentration on cell damage

For shearing, 2 mL cell-alginate mixtures with a cell density of 1×10^6 cells/mL were loaded into the rheometer, which was rotated at a speed of 40 rpm. Cell suspensions with varying alginate concentrations (1.0, 1.5, 2.0, and 2.5% w/v) were sheared for 10 s at room temperature (~21 °C) and the cell viability examined. To ensure a sterile experimental environment, the rheometer was placed underneath a hood that had been cleaned three times with 70% ethanol. The parts of the rheometer to be in immediate contact with cells, including the plate and cone, were immersed in 70% ethanol for 10 min and then dried for more than 15 min in the hood prior to use. To examine cell damage, 100 µL of cell suspension after shearing were transferred to a plate, 30 µL of 0.2% Trypan blue (a dye

used to stain damaged cells) were added, and the number of damaged or dead cells then counted and recorded with the help of an optical microscope (Leica Microsystems, Germany). The examination of cell damage was repeated on five cell suspension samples sheared by the rheometer. As a positive control, a group of cell-alginate suspensions were retained in tubes and not sheared. The difference in cell damage (calculated as a percent) between the sheared and control groups was attributed to the corresponding shear stress.

4.3.4.2 Influence of exposure time on cell damage

A 2% cell-alginate suspension with a cell density of 1×10^6 cells/mL was loaded into the rheometer, which was set at a speed of 40 rpm. Shearing periods of 10, 30, 60, and 120 s were examined to evaluate the influence of exposure time on cell damage. The same procedure using Trypan blue and a microscope as described above was conducted for cell damage examination. Each test was repeated five times for each of the three cell types.

4.3.4.3 Influence of cell density on cell damage

2.0% alginate-cell suspensions with cell densities of 5×10^5, 1×10^6, 5×10^6, or 1×10^7 cells/mL were prepared using a pipette to ensure a homogenous distribution of cells. For each test, a 2 mL cell suspension was delivered to the rheometer, which was set as a speed of 40 rpm for suspensions with a low cell density (5×10^5 or 1×10^6 cells/mL) and 45 rpm for suspensions with a high cell density (5×10^6 or 1×10^7 cells/mL). This test was repeated five times for each cell density.

4.3.5 Evaluation of cell recovery and proliferation after shearing

4.3.5.1 Live/dead assay for cell viability evaluation

To investigate the recovery of cells after experiencing shear stress, a live/dead assay was performed to evaluate the viability of the three cell types 3, 6 and 48 h later after the removal of shear stress. An alginate-cell suspension with a cell density of 1×10^6 cells/mL was loaded into the rheometer and sheared at a speed of 40 rpm. After shearing, 100 uL of the cell suspension were transferred into a well of a 12-well plate, to which 900 μL of cell culture medium (calcium-free DMEM, 10% FBS, and 1% antibiotic) were then added. After placing the plate into a cell culture incubator for 3 h, a DMEM solution containing

0.5 μg/mL calcein-AM and 25 μg/mL propidium iodide (PI), which selectively stain live and dead cells, respectively, was added to the well. The plate was incubated for an additional 30 min at 37° C before examination using a fluorescent microscope (Carl Zeiss Axiovert 100). Both live and dead cell numbers were manually counted and analyzed using ImageJ (National Institutes of Health, Bethesda, Maryland, USA) from six images randomly taken from the cell suspension well, and the viability of cells was calculated as the percentage of live cells among the total cells. The same evaluation was conducted after 6 and 48 h. The shearing test and subsequent examination of cell viability were repeated three times. As a positive control, the cell viability of cell suspensions retained in the tube without shearing was examined. The recovered cell numbers were then obtained by comparing the observations made at different time points.

The influence of exposure time on viability and recovery of the three types of cells was subsequently examined. Alginate-cell suspensions with an alginate concentration of 2% and a density of 1×10^6 cells/mL were sheared for time periods of 60 or 120 s using the rheometer. The cell viability assay described above was utilized at 3, 6, and 48 h later upon removal of shear stress. To investigate the effect of cell density, 2% alginate-cell suspensions with cell densities of 1×10^5 or 1×10^7 cells/mL were sheared at either low speed (40 rpm) or high speed (45 rpm), respectively, for 60 s. Then, 10 μL of the high cell density suspension and 200 μL of the low cell density suspension were transferred into the 12-well plate and the viability assay conducted as described above.

4.3.5.2 MTT assay for cell proliferation evaluation

The influence of shear stress, exposure time, and cell density on the proliferation of cells was analyzed using an MTT assay. Suspensions of the three cell types were prepared as before, and delivered into 12-well plates after being sheared in the rheometer. To determine the effect of shear stress and exposure time on cell proliferation, 100 μL cell suspensions were pipetted into each well of the 12-well plate, to which 700 μL of cell culture medium (calcium free DMEM with 10% FBS and 1% antibiotic) were then added. To determine the effect of cell density on cell proliferation, 10 μL of the high density (1×10^7 cells/mL) cell suspension or 200 μL of the low density (5×10^5 cells/mL) cell

suspension were delivered into wells of the 12-well plate. Alginate-cell suspensions not subject to shear stress were treated as positive controls, and alginate solutions with no cells were prepared as the negative control.

An MTT assay was performed to evaluate cell proliferation. Cell suspensions (including positive and negative controls) in the 12-well plates were treated with 80 μL MTT reagent (5 mg/mL) and incubated for 3 h at 37 °C in a 5% CO_2 atmosphere. The culture medium was then carefully removed and replaced by a dimethyl sulfoxide (DMSO) solution (800 μL per well) to dissolve the formazan precipitate. After incubating for another 15 min, the uniformly dissolved formazan precipitate medium was transferred to 96-well plates (100 μL per well) and read by a microplate reader (SpectraMax 190, Molecular Devices, USA) at 555/650 nm at room temperature. Absorbance was read after 3, 6, and 48 h of incubation time. Each test was repeated three times of individual cell types.

Because MTT absorbance values can be significantly disturbed if alginate gels form in the medium, it is essential to eliminate the formation of alginate hydrogels before the MTT assay. A test used to examine the gelation of alginate triggered by FBS was conducted due to the minute amount of calcium ions present in the FBS. A 900 μL pure FBS solution was delivered into a micro-tube that contained 100 μL of 2.5% alginate solution. Alginate gelation was examined after 30 min, 2 h, and 24 h of uniform mixing at room temperature. Three micro-tubes were prepared to ensure the reliability of the result.

4.3.5.3 Hoechst/PI staining for cell viability and proliferation evaluations

Hoechst/PI staining for cell viability and proliferation evaluations was also performed to verify the recovery ability of cells after experiencing shear stress. Fluorescent Hoechst and PI dyes were used to selective stain live and dead cells (Hoechst) and dead cells only (PI). Solutions including alginate-NIH-3T3 suspensions with a fixed cell density (1×10^6 cells/mL) but different alginate concentrations (1.5 and 2.5%), 2% alginate-L8 suspensions with a fixed cell density (1×10^6 cells/mL), and 2% alginate-RSC96 suspensions with varying cell densities (5×10^5 and 1×10^7 cells/mL) were prepared and sheared using the rheometer. Cell suspensions were then cultured in 96-well plates (special plates for fluorescent plate reader, 100 μL per well) in an incubator after the shear stress was removed. Before observation, cells were stained using Hoechst (1 μg/mL) and PI (25

μg/mL) for 20 min in the incubator, and the culture medium with fluorescent dyes then transferred into micro-tubes to centrifuge for 10 min at 800 rpm. After aspirating the old medium and adding fresh DMEM to the micro-tubes, the retained cells (including live and dead cells) were delivered back to the same 96-well plates with 100 μL per well. The fluorescent absorbance was obtained at an excitation/emission wavelength of 355/460 nm for Hoechst and 520/617 nm for PI using a fluorescent microplate reader (SpectraMax M2e, Molecular Devices, USA) after the cells were cultured for 3, 6, and 48 h. This entire evaluation was conducted three times.

4.3.6 Statistical analysis

Mean values and standard error of the mean (SEM) of all data were calculated. Statistical significance was determined by ordinary one-way analysis of variance (ANOVA) and multiple comparisons were performed using Tukey's test and Graphpad Prism (GraphPad Software, San Diego, CA, USA) with an acceptable significance level of $P < 0.05$.

4.4 Results

Figure 4.2 illustrates the effect of temperature and alginate concentration on measured shear stresses applied to an alginate solution. The shear stress decreases with temperature for all alginate concentrations, which suggests the alginate solution becomes less viscous as the temperature increases. The shear stress also increases with alginate concentration for any given temperature, which suggests the alginate solution becomes more viscous as the alginate concentration increases. The 3 and 4% alginate solutions were observed during these experiments to be much more viscous than the 1 and 2% solutions. Due to limits in the shear stress that could be measured by the rheometer, shearing experiments were performed at a lower shear rate of 5 s^{-1} for 3 and 4% solutions (Figure 4.2A) and a higher shear rate of 100 s^{-1} for 1 and 2% solutions (Figure 4.2B).

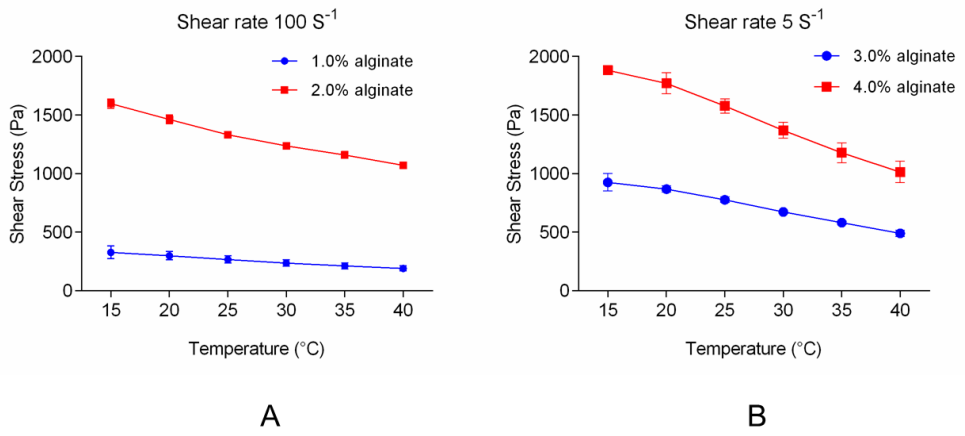

Figure 4. 2 Influence of temperature and alginate concentration on flow behavior of alginate solution. A, 1 and 2% alginate solution under shear rate of 100 S^{-1}; B, 3 and 4% alginate solution under shear rate of 5 S^{-1}.

Figure 4.3 depicts the influence of cell density on the flow behavior of 1% alginate solutions mixed with three kinds of cells. Similar to the alginate only solution, the alginate-cell suspensions responded to shear in a non-linear fashion. The solution without cells experienced the highest shear stress compared to the alginate-cell suspensions for the same shear rate. As cell density increased the shear stress decreased, and the change in shear stress depended on the both the type of cells and the number of cells added. At a shear rate of 400 s^{-1}, for example, the shear stress was reduced by 7.73, 6.19, and 10.83% with the addition of 5×10^5 RSC96 (Figure 4.3A), L8 (Figure 4.3B), and NIH-3T3 (Figure 4.3C) cells/mL, respectively, as compared to the solutions without cells. If the cell density increased to 1×10^7 cells/mL, the shear stress was reduced by 36.21% for RSC96 cells, 40.08% for NIH-3T3, and 32.35% L8 cells.

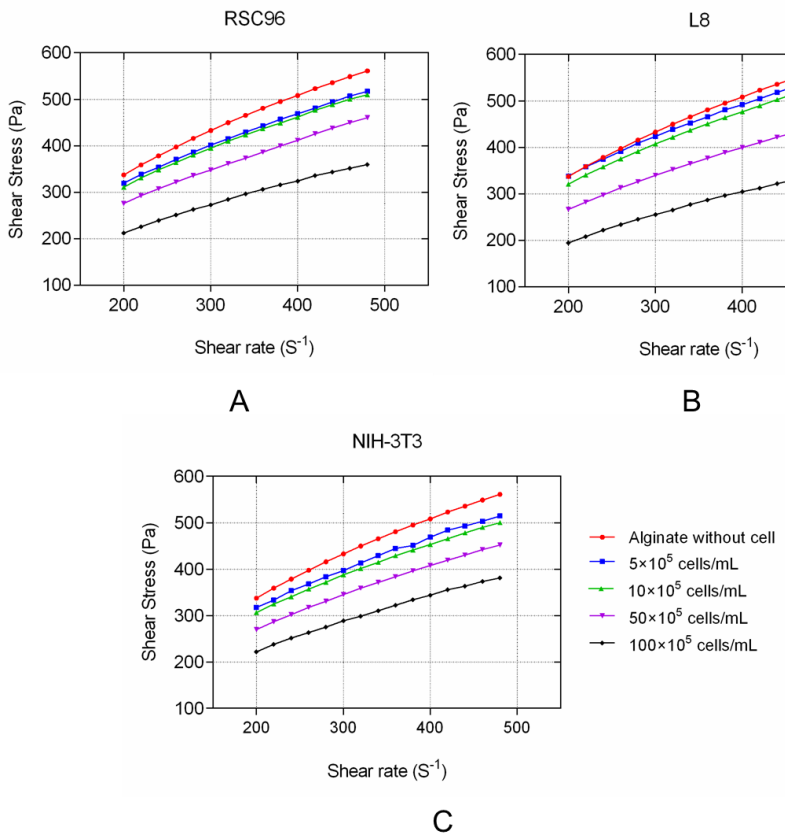

Figure 4. 3 Influence of cell type and density on flow behavior of alginate-cell suspension. A, RSC96; B, L8; C, NIH-3T3.

Figure 4.4 shows the cell damage measured after cells were exposed to varying shear stresses for 10 s. For all cell types, the damage not surprisingly worsened as the shear stress increased. For example, Figure 4.4A shows that 4.89±0.89% and 5.21±0.74% of RSC96 cells were damaged after being sheared at 300 Pa (1.0% alginate solution) and 600 Pa (1.5% alginate solution), respectively; these percentages increased to 10.73±0.80% and 21.36±2.39% for shear stresses of 1100 Pa (2.0% alginate solution) and 1700 Pa (2.5% alginate solution), respectively. The same cell damage trends were also observed for L8 and NIH-3T3 cells (Figures 4.4B and 4.4C). Low levels of damage (2.62±0.30% for L8 and 2.94±1.26% for NIH-3T3) were induced by a low shear stress of 300 Pa (1.0% alginate solution), but increased with the shear stress applied. For a shear stress of 1700 Pa (2.5% alginate solution), the percent cell damage rose to 13.87±1.65% and 14.10±2.79% for L8 and NIH-3T3 cells, respectively, both of which are lower than corresponding data for RSC96 cells.

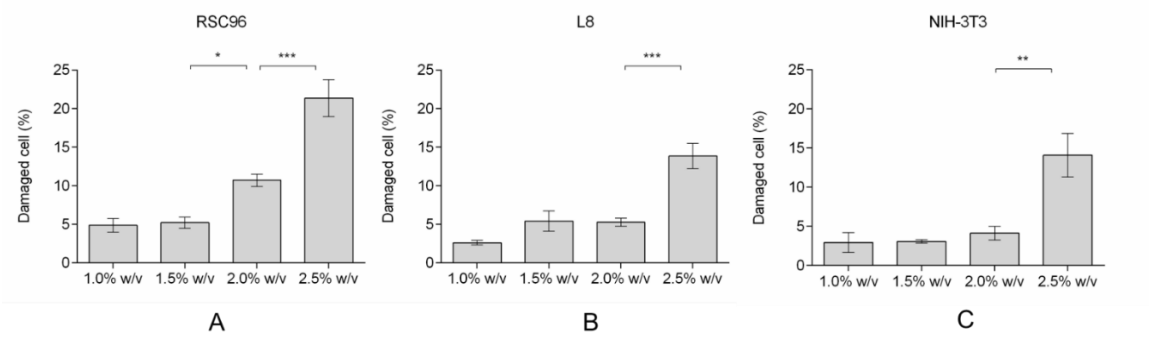

Figure 4. 4 Percentage of damaged cells in alginate-cell suspension at varying shear stress from 300 Pa to 1700 Pa. A, RSC96; B, L8; C, NIH-3T3. One-way ANOVA,* represent $P < 0.05$, ** represents $P < 0.01$ and *** represents $P < 0.001$

Figure 4.5 exhibits the effects of shear period on cell damage for the three cell types. It is clear from figures that the number of damaged cells increased with shear time. In Figure 5A, for example, the percent damaged RSC96 cells slowly grew from 10.73±0.80% to 12.64±1.01% as the shear period extended from 10 and 60 s, and then rapidly increased to 28.50±1.63% after cell were exposed to shear stress for 120 s. Damage to NIH-3T3 cells (Figure 4.5C) follows a similar trend, and reached 25.97±0.29% after being sheared for 120 s. In contrast, damage to L8 cells increased slowly and steadily as the shear period increased to 120 s (Figure 4.5B), with a consequent lower percent damaged cells (15.76±2.15%) than observed for either RSC96 or NIH-3T3 cells.

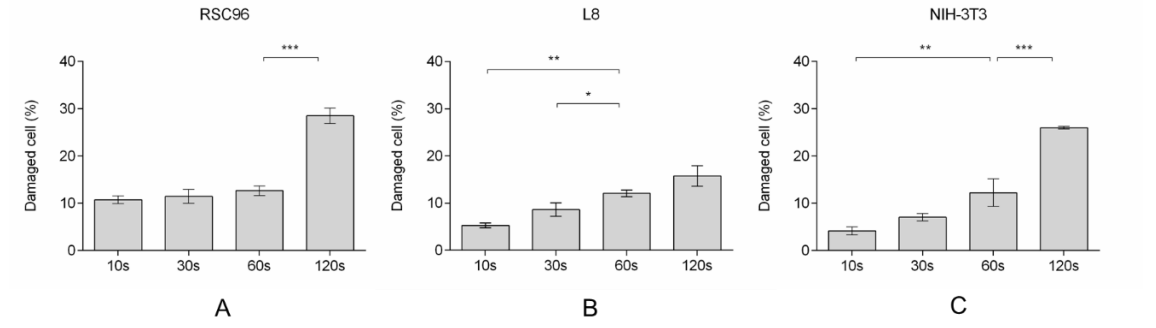

Figure 4. 5 Percentage of damaged cells in alginate-cell suspension at varying shear time. A, RSC96; B, L8; C, NIH-3T3. One-way ANOVA,* represent $P < 0.05$, ** represents $P < 0.01$ and *** represents $P<0.001$

Figure 4.6 shows the effect of cell density on cell damage after the shearing process. Overall, cell damage for the three cell types for a fixed shear period declined as cell density

increased. Figures 4.6A and 4.6C show that 12.21±1.94% and 12.64±1.01% of RSC96 cells were damaged and 12.59±2.81% and 12.20±2.91% of NIH-3T3 cells were damaged for densities of 5×10^5 and 1×10^6 cells/mL, respectively. The L8 cell damage rate was higher (18.67±3.09%; Figure 4.6B) for the low density cell suspension (5×10^5 cells/mL). Notably, the percent damage for all cell types decreased when cell densities increased to 1×10^7 cells/mL, at 4.03±1.22%, 4.82±0.86%, and 4.62±0.76% for RSC96, L8, and NIH-3T3 cells respectively.

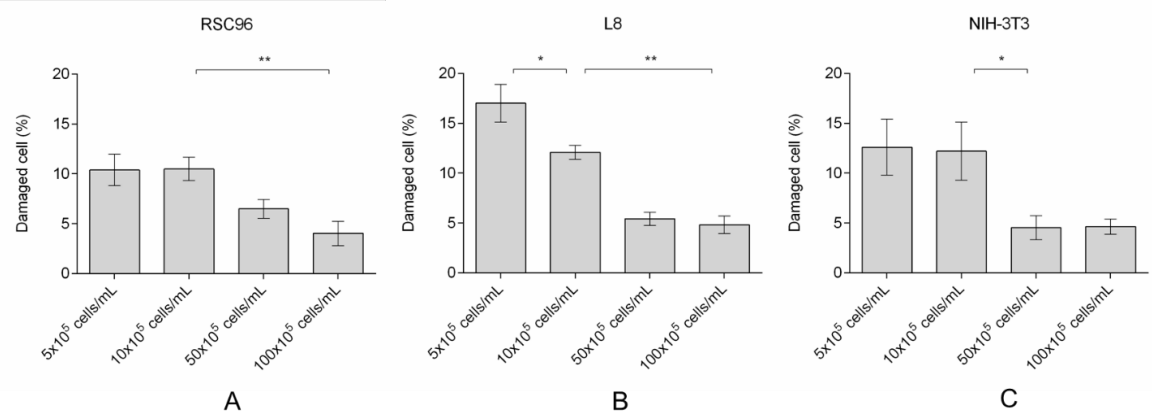

Figure 4. 6 Percentage of damaged cells in alginate-cell suspension affected by cell density. A, RSC96; B, L8; C, NIH-3T3. One-way ANOVA,* represent $P < 0.05$, and ** represents $P < 0.01$

Microscopic observations of live and dead cells at 3, 6, and 48 h for the three tested cell types indicate greater cell death was induced by higher shear stress (Figures 4.7A-4.7C), longer exposure time (Figures 4.7D-4.7F), and lower cell density (Figures 4.7G-4.7I). After the cells were sheared at controlled shear stresses of 600 Pa (1.5% alginate) or 1700 Pa (2.5% alginate), cell viabilities for NIH-3T3 cells (Figure 7J) were 93.29±1.37% and 82.99±1.85% after 3 h and 95.50±1.37% and 87.71±3.64% after 48 h, respectively. The comparable viabilities of L8 cells (Figure 7K) were 91.27±1.83% and 81.27±3.09% after 3 h and 95.42±0.60% and 89.45±1.82% after 48 h. Figure 4.7L shows the effect of cell density on the viability of RSC96 cells. Cell viability values were 93.82±1.62% (1×10^7 cells/mL) and 87.03±2.75% (5×10^5 cells/mL) after 3 h but, as observed for the other two cell types, grew to 95.19±1.26% and 91.11±2.24% after 48 h. There is very little change in cell viability for all cell types between 3 and 6 h of culture time, which suggests that only a few cells die during this period.

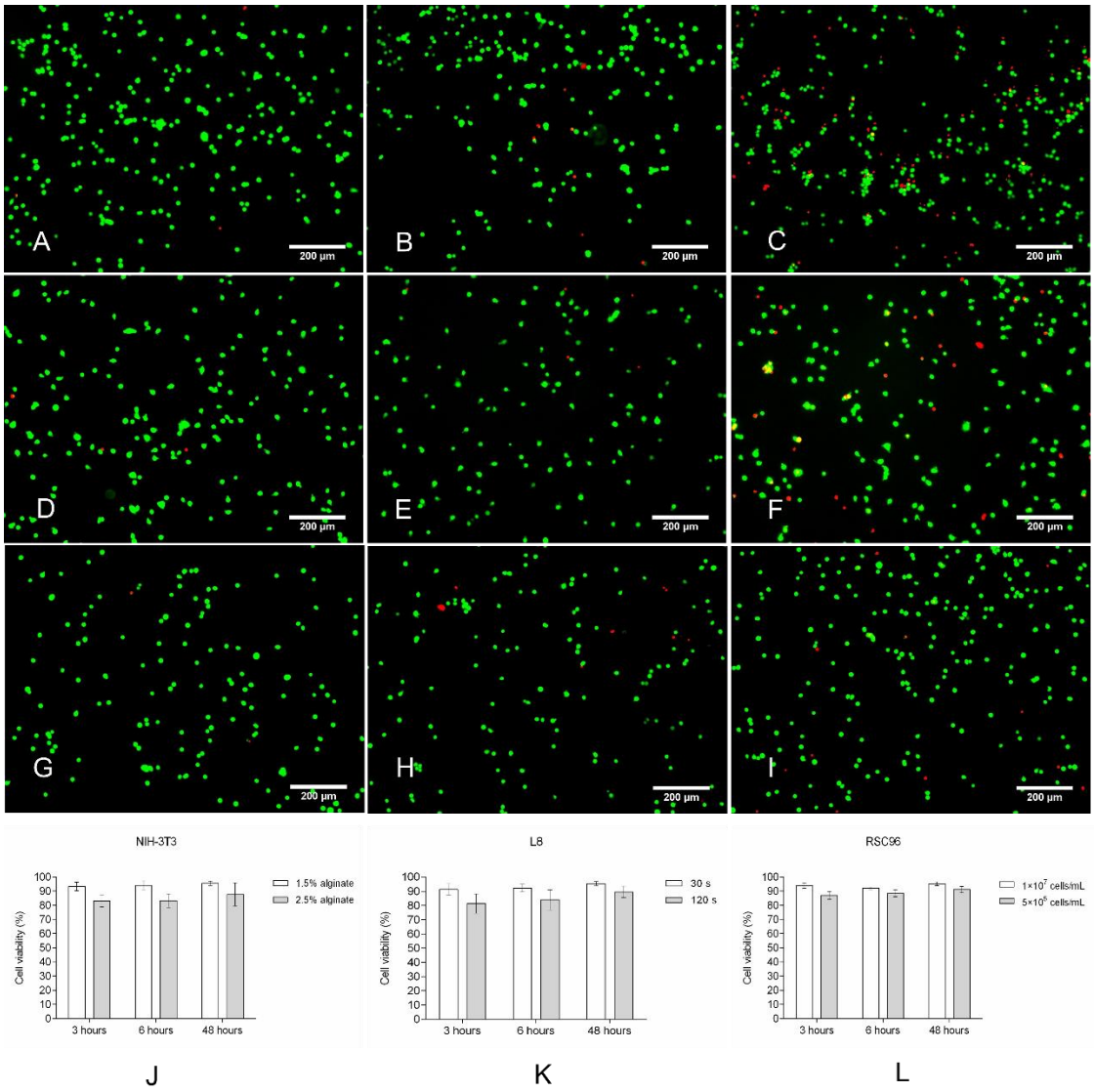

Figure 4. 7 Cell viability upon removal of the shear stress. A, D and G, non-sheared suspensions of NIH-3T3, L8 and RSC 96, respectively; B and C, sheared NIH-3T3 at different shear stress (600 Pa and 1700 Pa respectively); E and F, sheared L8 at different shear time (30 seconds and 120 seconds respectively); H and I, sheared RSC 96 affected by cell density (10×10^5 and 100×10^5 cell/mL). All the images were taken at 6 hours of cell culture; J-L, analysis of the viabilities of NIH-3T3, L8 and RSC96 respectively.

An MTT assay was performed to evaluate the proliferation and recovery properties of three cell types 3, 6, and 48 h after shear stress was removed. As our methods indicated that gel was seldom formed by FBS, the effect of alginate hydrogel on the MTT assay was considered insignificant. Figure 4.8 shows the effect of shear stress on cell proliferation.

The absorbance values of all sheared cell suspensions were less than for non-sheared cells after 6 h, which verifies that cells are damaged during shearing. The two positive controls (1.5 and 2.5% alginate-cell suspensions) had close absorbance values, so data for only the 1.5% alginate non-sheared cell suspensions are presented. The absorbance values of sheared RSC96 cells after 6 hours in culture were 90.32% (1.5% alginate) and 82.58% (2.5% alginate) of those of non-sheared controls (Figure 4.8A); corresponding data for L8 were 95.97% and 86.29% (Figure 4.8B) and 99.46% and 85.94% for NIH-3T3 (Figure 4.8C). After 48 h, the MTT absorbance for sheared cells decreased compared to non-sheared cells, specifically to 83.96% and 72.61% for RSC96 cells, 89.50% and 82.22% for L8 cells, and 90.77% and 85.27% for NIH-3T3 cells respectively, suggesting that the proliferation rate of cells slowed after they were disturbed by shear stress.

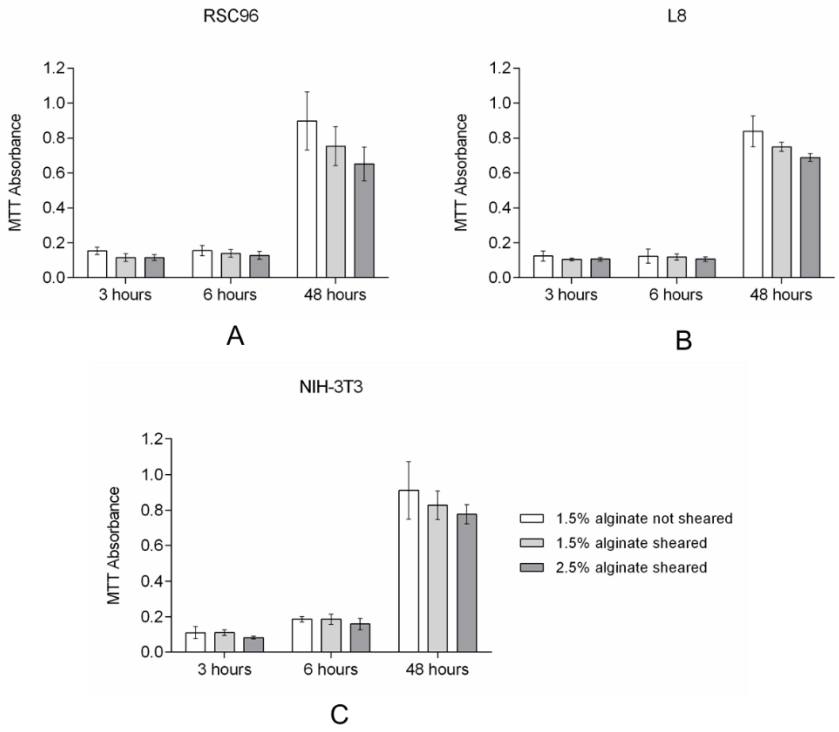

Figure 4. 8 MTT absorbance of cells affected by varying shear stress. A, RSC96; B, L8; C, NIH-3T3.

Figure 4.9 shows the effect of shear period on cell proliferation. Similar to the effect of shear stress, cell proliferation as indicated by MTT absorbance for cell suspensions 6 h post-shearing was less than for corresponding non-sheared cell suspensions. For instance, the MTT absorbance values of RSC96 cells (Figure 4.9A) were 93.85% (30 s) and 86.15%

(120 s) that of non-sheared cell suspensions; corresponding values for L8 and NIH-3T3 cells were 92.63 and 86.32% (Figure 4.9B) and 94.48 and 84.83% (Figure 4.9C), respectively. These results verify observations from the cell damage tests that indicate a longer shear period leads to greater cell death, but compared to non-damaged cell percentages indicated from Figure 4.5, the percentages of MTT absorbance are higher. Damage to sheared RSC96 cells decreased after 48 h to 92.83 and 81.73% after being sheared for 30 or 120 s, respectively, with the same decreasing trends found for both L8 cells (90.72 and 82.02%) and NIH-3T3 cells (92.42 and 82.53%).

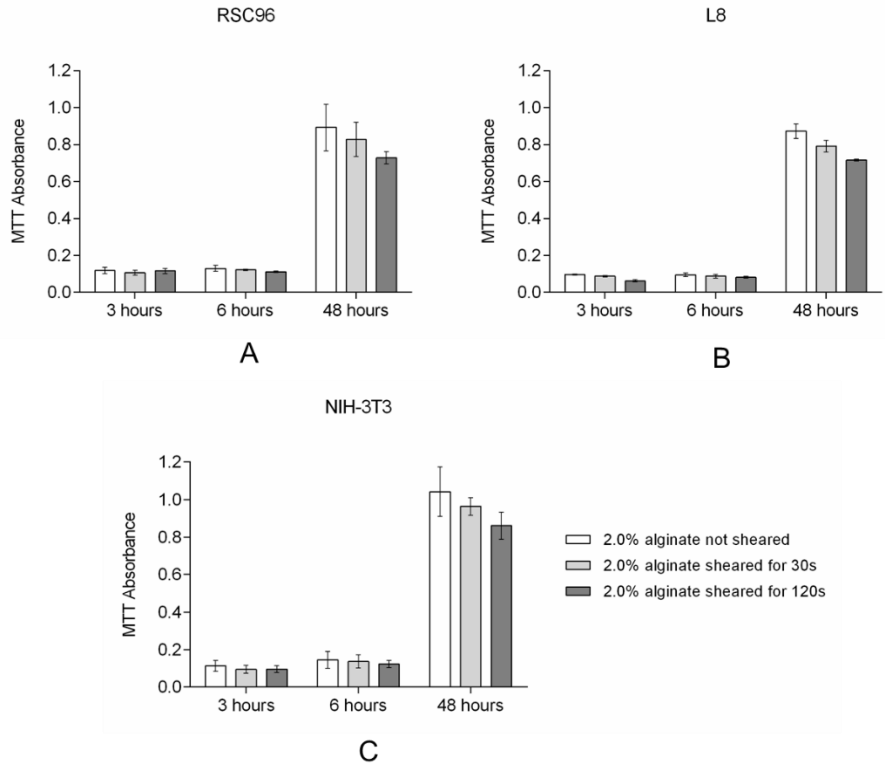

Figure 4. 9 MTT absorbance of cells affected by varying shear time. A, RSC96; B, L8; C, NIH-3T3.

The influence of cell density on the proliferation of different types of cells was also evaluated. Absorbance values after 6 h suggest fewer living cells in the sheared cell suspensions than in the non-sheared cell suspensions (Figure 4.10). Specifically, the absorbance of sheared RSC96 cells with high cell density (1×10^7 cells/mL) was 93.33% of that for non-sheared cells after 6 h; the percentage decreased to 91.00% for the low cell density (5×10^5 cells/mL) cell suspension (Figure 4.10A). The absorbances of L8 cells

(Figure 4.10B) were 96.97 and 90.91% of the positive control for high and low cell density cell suspensions, respectively. The response of NIH-3T3 cells to shear stress shares (Figure 4.10C) the same trend as the other two cell types, at 94.74% (1×10^7 cells/mL) and 88.42% (5×10^5 cells/mL), respectively. The percentages for all cell types were decreased at 48 h compared to the values at 6 h, and more decrease was observed for the sheared suspensions with low cell density which suggests that the proliferating rate of sheared cells is further reduced if fewer cells are included in the suspension.

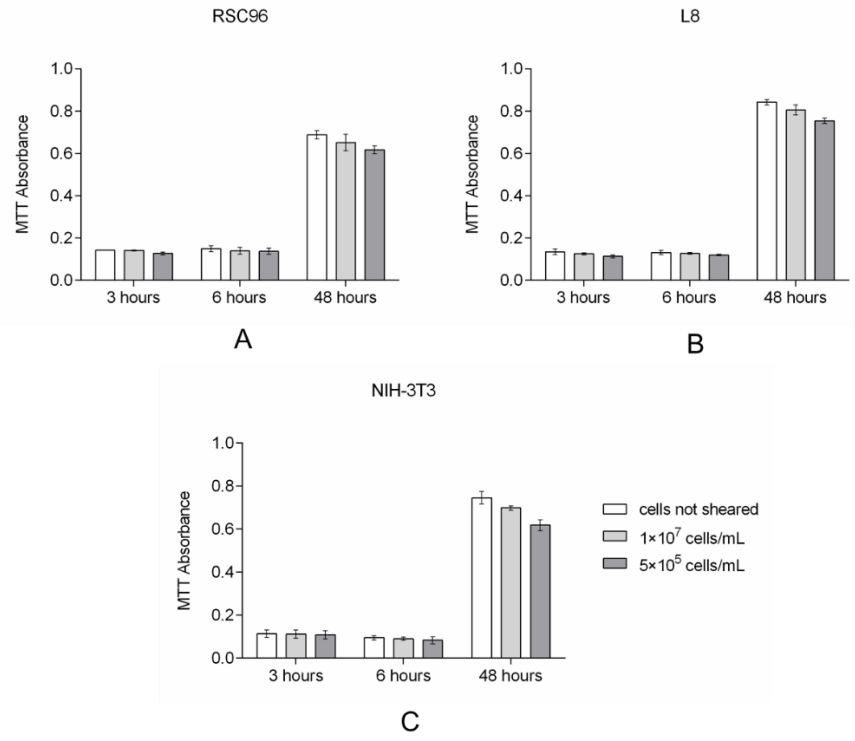

Figure 4. 10 MTT absorbance of cells affected by cell density. A, RSC96; B, L8; C, NIH-3T3.

The results of the Hoechst/PI staining assay are presented in Figures 4.11 and 4.12, with absorbance values of the cell suspensions presented as a percent of that for non-sheared controls. For each cell type under different shear conditions, only a slight change of fluorescent absorbance occurred from 3 to 6 h, while the distinctions became obvious after 48 h (Figures 4.11A to 4.11C). Compared to non-sheared cells, the absorbance of sheared cells decreased as cell culture time extended to 48 h for all conditions evaluated. Overall, increasing shear stress or shear time, or decreasing cell density, adversely affected cell proliferation. The results from PI staining confirm the results of the cell viability tests,

i.e., that more cells were damaged with higher shear stress, longer exposure time, or lower cell density (Figures 4.12A to 4.12C). The figure also shows that the absorbance percentages of sheared cells were relatively steady across the different time points, which suggests that the number of dead cells did not change much within the first 48 h after shearing.

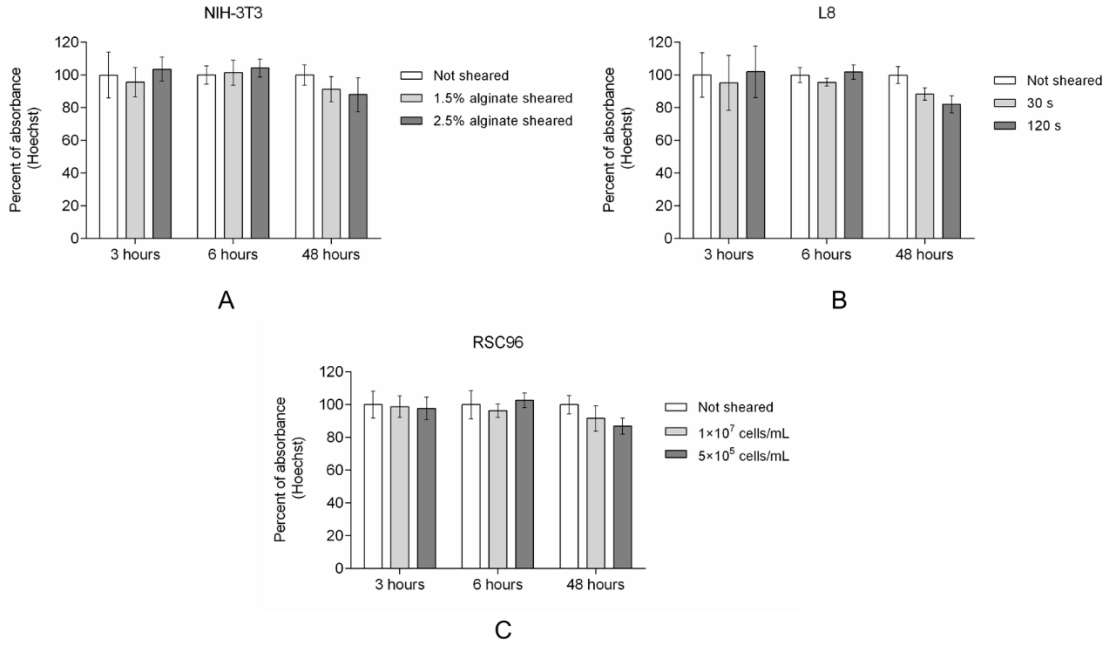

Figure 4. 11 Absorbance of cells stained by Hoechst. A, NIH-3T3; B, L8; C, RSC96.

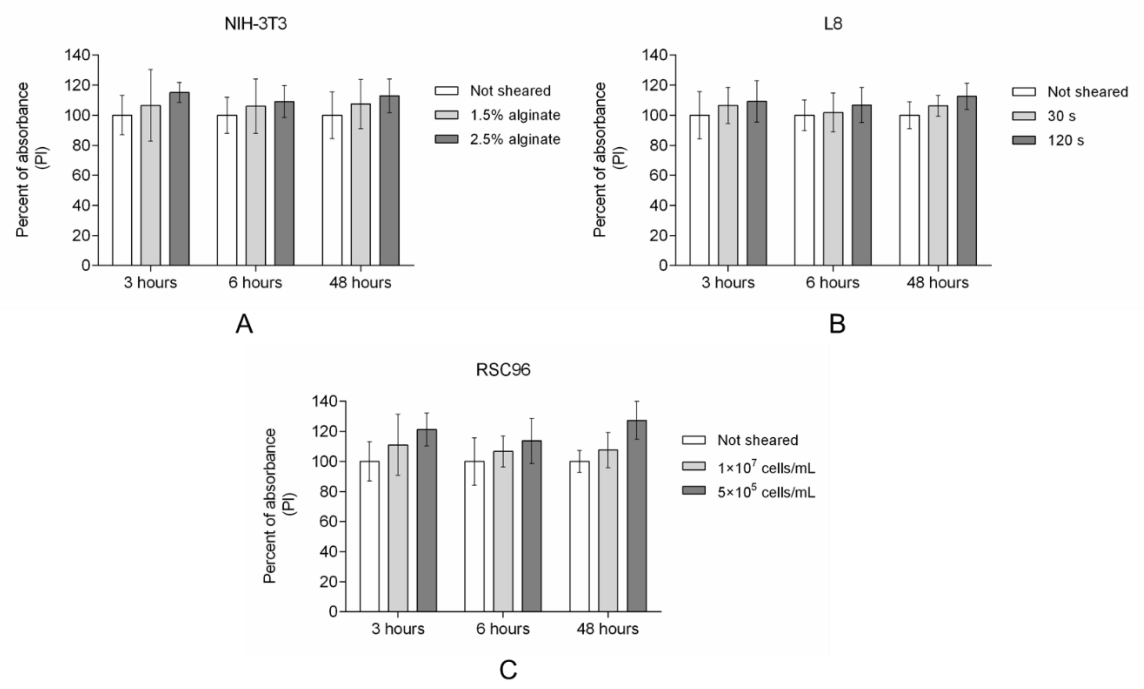

Figure 4. 12 Absorbance of cells stained by PI. A, NIH-3T3; B, L8; C, RSC96.

4.5 Discussion

3D bio-printing/plotting techniques for tissue scaffold fabrication have become popular due to their ability to manipulate biomaterial-cell suspensions with a high density of living cells. Cells in suspensions for tissue scaffold fabrication can be protected from immunoreactions by the biomaterials or the later-formed gels once the scaffolds are implanted into hosts [7,40,41]. However, the performance of the cells can be significantly affected by the flow behavior of the cell suspensions in the printing process. Thus, the present study evaluated the flow behavior of cell-alginate suspensions as expressed by stress-strain curves. The collected data demonstrate that the flow behavior of the suspensions can be notably altered by the concentration of alginate, the environmental temperature, or the incorporated cells type and number.

Our results agree with conclusions that more incorporated cells reduce the shear stress of suspensions [32]. This phenomenon is likely due to cell-cell and cell-biomaterial solution interactions, because the flow behavior of the single-phase alginate solution changes as it becomes a two-phase solution as cells are encapsulated [30]. One percent alginate solution was used to form the cell suspensions evaluated for flow behavior using

a rheometer. This is because cell suspensions in a high alginate concentration solution would significantly increase the viscosity, which introduces the potential errors in suspension delivery. Therefore, the lowest alginate concentration among the four concentrations considered at the outset of the present study was employed for the remainder of the experiments to ensure the accuracy of the transferred volume and the reliability of the results obtained.

Cells are subjected to shear stress in the bio-printing process when the cell suspensions are forced to flow through the nozzle tip. The shear stress applied to the cells is not only determined by the properties of the suspension but also by the dispensing pressure and nozzle size [31]. The elastic capability of cells normally allows them to withstand deformation induced by shear stress and recover to their original shape once the stress is removed [42]. However, cell damage caused by structural failure occurs when the stresses applied to the cells exceeds their tolerance limits [34]. In the present study, over 15% of cells were damaged when a shear stress of 1700 Pa was applied for just 10 s. This demonstrates the negative effects of shear stress on the cells, and informs the choice of appropriate values of dispensing pressures and nozzle diameters in scaffold bio-printing to ensure high cell viability. The effect of exposure time on cell viability suggests that cell manipulations should not exceed 2 min at a shear stress of 1100 Pa or the percent damaged cells climbs above 15%. This result informs nozzle selection for scaffold bio-printing, because the shear time cells experience may exceed the threshold of cell toleration and lead to significant cell death if the nozzle tip is too long.

Different types of cells in various organs and tissues have different physical, chemical, and biological properties [43]. Cells in either soft or mineralized tissues subject to uniform situations of mechanical stress transmission and sensation would have various responses the external stimulation. Estimates of mechanical properties of cells using a wide range of methods indicates that the measured elastic modulus of isolated cells generally ranges from 0.1 kPa (alveolar epithelial) to an approximate upper limit of 40 kPa (myocytes) [44]. The magnitude of the elastic properties is believed to be determined by diverse molecular structures, such as the cell membrane and cytoskeleton, which can distinguish the abilities of diverse cell types to withstand forces and recover to their normal phenotype [45]. In this study, Schwann cells were the weakest of the three cell types with respect to

the applied shear stress because more cells were damaged when the shear stress or exposure time increased. This can be explained by the inherent elastic ability of cells themselves. Schwann cells are the major glial cells in the peripheral nervous system and have inherently weak mechanical properties compared to other tissues such as skeletal muscles or bones [46-48]. Thus, the ability of Schwann cells to endure external stresses would be limited by their intrinsic characteristics, which makes them more susceptible damage.

The results of this study also demonstrate that increasing cell density has a positive effect on protecting cell viability. For all three cell types tested, the number of damaged cells decreased with increasing cell density (Figure 4.6). When the cell density reached a relatively high level (e.g., 1×10^7 cells/mL), less than 5% of the cells were damaged after being subjected to 1100 Pa of shear stress for 60 s. This indicates that interactions between cells likely protect them from damage caused by shearing, and greater cell numbers heighten this protection.

An evaluation of cell recovery and proliferation was carried out using multiple methods, including an MTT assay, a live/dead assay, and Hoechst/PI staining, to ensure the reliability of results. We expected our results to reflect the existence of three distinct cell states after shearing: unchanged cells with regular phenotypes, cells that survived but are damaged or quiescent, and dead cells. Cells that are damaged but still alive may have the ability to recover their regular functions, or may remain quiescent without any cellular expression and slowly die. With the assistance of the live/dead assay (Figure 4.7), an increase in live cell numbers for all cell types was observed after culturing the sheared cells for 6 h as compared with results from cell damage tests (Figures 4.4-4.6). This can be explained by the recovery of damaged cells after a certain period of time in culture. The assumption is supported by the steady number of living non-sheared cells, which changed only slightly after 6 h, indicating that the increase in the viability of sheared cells represents the recovery of injured cells. Moreover, the MTT assay results indicate similar absorbance values after 3 and 6 h for all examined cells; this suggests that cell proliferation does not occur within this short period and supports the premise that the increase in cell viability is due to the recovery of damaged cells. Cell proliferation continued to 48 h as confirmed by the results of both the live/dead assay and MTT assay; absorbance values kept increasing while a relatively constant number of dead cell were found under the fluorescent

microscope, which indicates the increasing cell numbers are due to cell regeneration. Hoechst/PI staining results also verify the occurrence of cell proliferation because the absorbance of Hoechst stained cells continued to increase while values from PI staining remained constant.

Alginate solution can gel upon encountering calcium ions, which would affect the accuracy of absorbance values for the MTT assay when utilized for cell proliferation tests. To avoid this complication, the present study used calcium-free DMEM and confirmed that gelation was insignificant. Irregular MTT values for sheared and non-sheared cells were noted for the 3 h samples wherein the absorbance of non-sheared cells was lower than sheared cells in some cases (Figures 4.8-4.10). This was attributed to the loss of poorly attached cells when the culture mediums were aspirated out (MTT protocol) just 3 h after cell suspensions were delivered into 12-well plates [49]. To address this issue, Hoechst/PI staining tests were applied and special manipulations in the examining process were conducted. The results of the Hoechst/PI staining assay agree with observations from the cell damage testing, and the absorbance values at 6 and 48 h concur with results from both the live/dead and MTT assays. After 48 h, results from the MTT assay and Hoechst/PI staining indicated a significant increase in cell numbers for all samples although the absorbances of the sheared cell suspensions were less than for corresponding control samples. However, cell proliferation of sheared cells was less than controls, especially for cells subjected to a higher shear stress or a longer shear period. Thus, the selection of dispensing pressure and nozzle size in tissue scaffold bio-printing is important because the related shear stress and shear time not only lead to cell damage but also significantly reduced cell proliferation if improper parameters are utilized. Our results also indicate that cell density plays an important role in preserving cell proliferation because cell suspensions with high cell densities were able to better maintain their proliferation capacity after shearing compared to those with low cell densities.

The combined results of the cell damage test, live/dead assay, MTT assay, and Hoechst/PI staining from the present study show relatively constant dead cell numbers for all of the sheared cell suspensions, indicating that few living cells died within the first 48 h in culture. The proliferation rate of sheared cells was lower than for non-sheared cells,

which demonstrates that some sheared cells might have still been alive after 48 h but had lost their proliferation capacity.

4.6 Conclusions

This chapter presents our investigations into the flow behavior of biomaterial-cell suspensions and the impact of shear stress on cell viability and proliferation, as exemplified using alginate-Schwann cell, alginate-fibroblast, and alginate-myoblast suspensions. The examination of flow behavior extends previous studies and demonstrates that not only temperature and biomaterial concentration but also cell density can significantly alter the flow behavior of cell suspensions. Furthermore, data for all cell suspensions examined in this study indicate that increasing the cell density can reduce the shear stress for a given shear rate. Moreover, our results show cell viability and proliferation can be affected by shear stress, shear time, and cell density. These findings provide a means to preserve the cell viability and/or to retain cell proliferation function in the bio-printing process by regulating the flow behavior of cell-biomaterial suspensions and process parameters. Also, the data and results of this study provide useful information for future characterization of the cell damage in 3D printing processes using mathematical models to predict the viability and proliferation of cells encapsulated in biomaterials/scaffolds.

4.7 References

[1] Drury, J.L., and Mooney, D.J. Hydrogels for tissue engineering: scaffold design variables and applications. *Biomaterials* 24, 4337, 2003.

[2] Langer, R., and Vacanti, J.P. Tissue engineering. *Science* 260, 920, 1993.

[3] Coelho, P.G., Hollister, S.J., Flanagan, C.L., et al. Bioresorbable scaffolds for bone tissue engineering: optimal design, fabrication, mechanical testing and scale-size effects analysis. *Med Eng Phys* 37, 287, 2015.

[4] Goncalves, E.M., Oliveira, F.J., Silva, R.F., et al. Three-dimensional printed PCL-hydroxyapatite scaffolds filled with CNTs for bone cell growth stimulation. *J Biomed Mater Res Part B* 104, 1210, 2016.

[5] Pfister, A., Landers, R., Laib, A., et al. Biofunctional rapid prototyping for tissue-engineering applications: 3D bioplotting versus 3D printing. *J Polym Sci Part A Polym Chem* 42, 624, 2004.

[6] Castilho, M., Rodrigues, J., Pires, I., et al. Fabrication of individual alginate-TCP scaffolds for bone tissue engineering by means of powder printing. *Biofabrication* 7, 015004, 2015.

[7] Kang, A., Park, J., Ju, J., et al. Cell encapsulation via micro-technologies. *Biomaterials* 35, 2651, 2014.

[8] Shim, J.H., Lee, J.S., Kim, J.Y., et al. Bioprinting of a mechanically enhanced three-dimensional dual cell-laden construct for osteochondral tissue engineering using a multi-head tissue/organ building system. *J Micromech Microeng* 22, 085014, 2012.

[9] Sachlos, E., and Czernuszka, J. Making tissue engineering scaffolds work. Review: the application of solid freeform fabrication technology to the production of tissue engineering scaffolds. *Eur Cell Mater* 5, 39, 2003.

[10] Li, M., Tian, X., and Chen, X. A brief review of dispensing-based rapid prototyping techniques in tissue scaffold fabrication: role of modeling on scaffold properties prediction. *Biofabrication* 1, 032001, 2009.

[11] Murphy, S.V., and Atala, A. 3D bioprinting of tissues and organs. *Nat Biotechnol* 32, 773, 2014.

[12] Bajaj, P., Schweller, R.M., Khademhosseini, A., et al. 3D biofabrication strategies for tissue engineering and regenerative medicine. *Annu Rev Biomed Eng* 16, 247, 2014.

[13] Draget, K.I., Skjak-Bræk, G., and Smidsrød, O. Alginate based new materials. *Int J Biol Macromol* 21, 47, 1997.

[14] Lee, K.Y., and Mooney, D.J. Hydrogels for tissue engineering. *Chem Rev* 101, 1869, 2001.

[15] Nicodemus, G.D., and Bryant, S.J. Cell encapsulation in biodegradable hydrogels for tissue engineering applications. *Tissue Eng Part B Rev* 14, 149, 2008.

[16] Li, M., Tian, X., and Chen, X. Modeling of flow rate, pore size, and porosity for the dispensing-based tissue scaffolds fabrication. *J Manuf Sci Eng* 131, 034501, 2009.

[17] Zhu, N., Li, M., Cooper, D., et al. Development of novel hybrid poly (l-lactide)/chitosan scaffolds using the rapid freeze prototyping technique. *Biofabrication* 3, 034105, 2011.

[18] Zhang, Y., Yu, Y., and Ozbolat, I.T. Direct bioprinting of vessel-like tubular microfluidic channels. *J Nanotechnol Eng Med* 4, 020902, 2013.

[19] Min, Z., Shichang, Z., Chen, X., et al. 3D-printed dimethyloxallyl glycine delivery scaffolds to improve angiogenesis and osteogenesis. *Biomater Sci* 3, 1236, 2015,

[20] Onoe, H., Okitsu, T., Itou, A., et al. Metre-long cell-laden microfibres exhibit tissue morphologies and functions. *Nat Mater* 12, 584, 2013.

[21] Cornock, R., Beirne, S., Thompson, B., et al. Coaxial additive manufacture of biomaterial composite scaffolds for tissue engineering. *Biofabrication* 6, 025002, 2014.

[22] Kim, G., Ahn, S., Kim, Y., et al. Coaxial structured collagen– alginate scaffolds: fabrication, physical properties, and biomedical application for skin tissue regeneration. *J Mater Chem* 21, 6165, 2011.

[23] Mironov, V., Kasyanov, V., and Markwald, R.R. Organ printing: from bioprinter to organ biofabrication line. *Curr Opin Biotechnol* 22, 667, 2011.

[24] Orive, G., Herna´ndez, R.M., Gasco´n, A.R., et al. Cell encapsulation: promise and progress. *Nat Med* 9, 104, 2003.

[25] Rajaram, A., Schreyer, D., and Chen, D. Bioplotting alginate/hyaluronic acid hydrogel scaffolds with structural integrity and preserved Schwann cell viability. *3D Print Addit Manuf* 1, 194, 2014.

[26] Chang Yan, K., Nair, K., and Sun, W. Three-dimensional multi-scale modelling and analysis of cell damage in cell-encapsulated alginate constructs. *J Biomech* 43, 1031, 2010.

[27] Tallawi, M., Rai, R., Boccaccini, A.R., et al. Effect of substrate mechanics on cardiomyocyte maturation and growth. *Tissue Eng Part B Review* 21, 157, 2014.

[28] Desai, E.S., Tang, M.Y., Ross, A.E., et al. Critical factors affecting cell encapsulation in superporous hydrogels. *Biomed Mater* 7, 024108, 2012.

[29] Nair, K., Gandhi, M., Khalil, S., et al. Characterization of cell viability during bioprinting processes. *Biotechnol J* 4, 1168, 2009.

[30] Billiet, T., Gevaert, E., De Schryver, T., et al. The 3D printing of gelatin methacrylamide cell-laden tissue engineered constructs with high cell viability. *Biomaterials* 35, 49, 2014.

[31] Li, M., Tian, X., Schreyer, D.J., et al. Effect of needle geometry on flow rate and cell damage in the dispensing-based biofabrication process. *Biotechnol Prog* 27, 1777, 2011.

[32] Li, M.G., Tian, X.Y., and Chen, X. Temperature effect on the shear-induced cell damage in biofabrication. *Artif Organs* 35, 741, 2011.

[33] Ozbolat, I.T., Chen, H., and Yu, Y. Development of 'Multiarm Bioprinter' for hybrid biofabrication of tissue engineering constructs. *Robot Comput Integr Manuf* 30, 295, 2014.

[34] Tian, X.Y., Li, M.G., and Chen, X.B. Bio-rapid-prototyping of tissue engineering scaffolds and the process-induced cell damage. *J Biomim Biomater Biomedical Eng* 17, 1, 2013.

[35] Chang,R.,Nam, J., and Sun,W. Effects of dispensing pressure and nozzle diameter on cell survival from solid freeform fabrication-based direct cell writing. *Tissue Eng PartA* 14, 41, 2008.

[36] Gupta, R., Truong, L., Bear, D., et al. Shear stress alters the expression of myelin-associated glycoprotein (MAG) and myelin basic protein (MBP) in Schwann cells. *J Orthop Res* 23, 1232, 2005.

[37] Ouyang, L., Yao, R., Chen, X., et al. 3D printing of HEK 293FT cell-laden hydrogel into macroporous constructs with high cell viability and normal biological functions. *Biofabrication* 7, 015010, 2015.

[38] Li, M., Tian, X., Zhu, N., et al. Modeling process-induced cell damage in the biodispensing process. *Tissue Eng Part C Methods* 16, 533, 2009.

[39] Tirella, A., and Ahluwalia, A. The impact of fabrication parameters and substrate stiffness in direct writing of living constructs. *Biotechnol Prog* 28, 1315, 2012.

[40] Zehnder, T., Sarker, B., Boccaccini, A.R., et al. Evaluation of an alginate–gelatin crosslinked hydrogel for bioplotting. *Biofabrication* 7, 025001, 2015.
[41] Lee, H., Ahn, S., Chun, W., et al. Enhancement of cell viability by fabrication of macroscopic 3D hydrogel scaffolds using an innovative cell-dispensing technique supplemented by preosteoblast-laden micro-beads. *Carbohydr Polym* 104, 191, 2014.
[42] Secomb, T. Red blood cell mechanics and capillary blood rheology. *Cell Biophys* 18, 231, 1991.
[43] Hall, P.A., and Woods, A.L. Immunohistochemical markers of cellular proliferation: achievement, problems and prospects. *Cell Proliferation* 23, 505, 1990.
[44] Levental, L., Georges, P., and Janmey, P. Soft biological materials and their impact on cell function. *Soft Matter* 3, 299, 2007.
[45] Janmey, P., and Mcculloch, C. Cell mechanics: integrating cell responses to mechanical stimuli. *Annu Rev Biomed Eng* 9, 1, 2007.
[46] Gu, Y., Ji, Y., Zhao, Y., et al. The influence of substrate stiffness on the behavior and functions of Schwann cells in culture. *Biomaterials* 33, 6672, 2012.
[47] Close, R. Dynamic properties of mammalian skeletal muscles. *Physiol Rev* 52, 129, 1972.
[48] Martin, R.B. Determinants of the mechanical properties of bones. *J Biomech* 24, 79, 1991.
[49] van Meerloo, J., Kaspers, G.J., and Cloos, J. *Cell sensitivity assays: the MTT assay.* Cancer Cell Culture. Hatfield, United Kingdom: Humana Press, 2011, pp. 237–245.

CHAPTER 5

Characterization of Cell Damage and Proliferative Ability during and after Bioprinting

This chapter has been submitted as "Liqun Ning, Nicholas Betancourt, David J. Schreyer, and Xiongbiao Chen, Characterization of cell damage and proliferative ability during and after bioprinting. *Biofabrication*". It is under reviewing. According to the Copyright Agreement, "the authors retain the right to include the journal article, in full or in part, in a thesis or dissertation".

5.1 Abstract

When a fluid containing living cells is subject to bioprinting, the cells experience process-induced stresses including shear and extensional stresses. These process-induced stresses breach cell membranes and can lead to cell damage, thus reducing cell viability and functioning within the printed constructs. Several studies have been conducted to determine the influence of shear stress on cell damage; however, the effect of extensional stress has been typically ignored in the literature despite recent evidence of its importance. This chapter examines the influence of both extensional and shear stress on cell damage and, on this basis, a novel method to characterize the cell damage that occurs during bioprinting is developed. In this method, cell damage caused by shear stress is evaluated with a rheometer while cell damage caused by extensional stress is inferred from the difference between the total cell damage that occurs throughout the bioprinting process and the cell damage attributed to shear stress. From the results, a relationship between cell damage and shear and extensional stresses in bioprinting is established. The proliferative ability of cells in the first 72 h after bioprinting is also investigated with the results illustrating that the process-induced stresses affect not only cell viability but also their proliferative ability after bioprinting. The method developed and the study results provide insight into the cell damage that occurs during bioprinting and the effect on proliferative ability thereafter, and can be used to optimize the bioprinting process so as to preserve cell viability and function.

5.2 Introduction

3D bioprinting techniques have been extensively utilized for the fabrication of viable, artificial biological constructs such as tissue scaffolds [1-5]. The key features of 3D bioprinting include the ability to print viable cells suspended in a biomaterial solution and deposit the biomaterial-cell suspensions in a spatially-controlled manner [6-8]. During the bioprinting process, the biomaterial-cell suspensions are loaded into the syringe of a bio-printer, then extruded or dispensed through a needle by force (e.g., applied pressure) to build 3D constructs. This printing force can induce sustained shear and extensional stresses on the cells, which can breach the cell membranes and damage the cells [9]. The resulting cell damage can significantly reduce cell viability and functioning within the printed structures [10, 11]. Thus, knowledge regarding the factors that influence process-induced cell damage is of importance as it can be used to guide the design and optimization of the printing process so as to preserve cell viability and functioning.

The shear stress cells experience during the bioprinting process, which mainly occurs as the cell/biomaterial suspension is forced to flow through the narrow needle tip, is considered to be the major factor causing cell damage [12]. To measure this effect, experiments have examined cell damage in cell suspensions subjected to shearing stresses using a plate-and-cone rheometer to provide uniform and controllable shear stress on cells suspended in a solution; and the results illustrate that cell damage is associated with the level of shear stress and shearing or exposure time for a given type of cells [11, 12]. A relationship between cell damage and shear stress, termed the cell damage law, has been established and then used to investigate cell damage in the bioprinting process [13]. Recent evidence indicates the extensional stress that cells experience during the bioprinting process can also play a crucial role in determining their viability after bioprinting [14, 15]. Extensional stress is generated due to the abrupt velocity change the cell suspension experiences as it is driven through the geometrically contracted region of the needle. Compared to shear stress, extensional stress can lead to more acute cell damage [16, 17]. Therefore, considering both shear and extensional stresses is of importance when establishing a relationship between cell damage and the bioprinting process, but this has rarely been taken into account.

Whereas the cell damage caused by shear stress has been investigated with the help of a plate-and-cone rheometer [18], studying cell damage caused by extensional stress has proved challenging due to the difficulty in producing a pure extensional flow with cell suspensions. In this chapter, a novel method is developed to determine a cell damage law considering extensional stress using cultured Schwann cells (RSC96) and myoblasts (L8). Specifically, because cell damage in the bioprinting process is an aggregation of both shear and extensional stress-induced cell damage, we conducted experiments in which we dispensed living cells in alginate solutions and measured the resulting percent cell damage. As we can determine the percent cell damage attributable to shearing from the established cell damage law, cell damage due to extensional stress can be calculated and then an extensional stress-based cell damage law established. This approach provides an overall representation of the cell damage introduced by the bioprinting process. We also evaluated the degree of cell damage (injured or dead) within 6 h of bioprinting as well as the viability and proliferation of printed cells after 24 and 72 h to understand the influence of cell damage on the longer-term preservation of biological functions in biological constructs.

5.3 Modelling cell damage in the bioprinting process

5.3.1 Cell damage in bioprinting

During bioprinting, several assumptions are made as the cell suspension is dispensed through the cylindrical needle (Figure 5.1): (1) the printed cell suspension is incompressible; (2) the fluid flow inside the needle tip is considered to be developed flow, and thus the velocity profile does not change with time; (3) there is no slip between the cell suspension and the wall of the needle; and (4) the pressure at the exit of the needle equals the ambient air pressure.

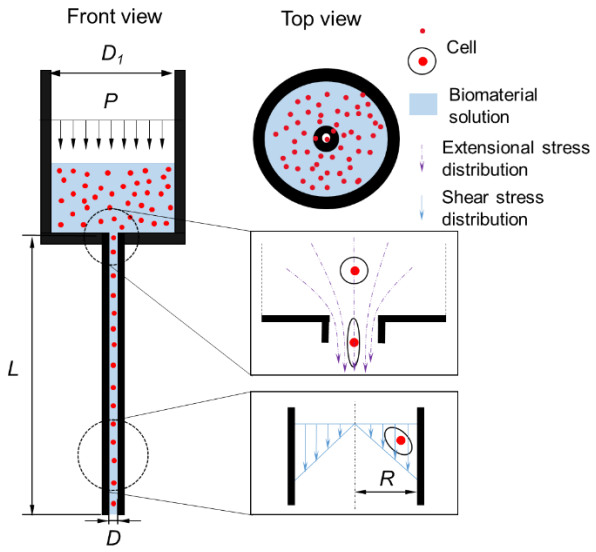

Figure 5. 1 Schematic of bioprinting needle and distributions of extensional and shear stresses inside the needle during bioprinting. D1=4.2mm; D=100 - 330 μm and R=50 - 165 μm; L=11 mm.

Cell damage in the form of membrane damage or breakage may occur during the bioprinting process due to process-induced stresses, i.e., both shear and extensional stresses (the influence of hydrostatic pressure on cell damage in bioprinting is ignored as concluded by [13]). For given bioprinting conditions, cell damage can generally be expressed as a function of stress and exposure time, i.e.,

$$D_t = f_1(D_{et}(\tau_e, t_e), D_{st}(\tau_s, t_s),), \tag{5.1}$$

where D_t represents the percent cell damage caused; D_{et} is the percent extensional stress-induced cell damage; τ_e and t_e are the magnitude of extensional stress and associated exposure time, respectively; D_{st} is the percent shear stress-induced cell damage; and τ_s and t_s are the magnitude of shear stress and associated exposure time, respectively.

Figure 5.2 shows a simulation (details given later) of the velocity change rate for both extensional (left) and shear (right) flow of a non-Newtonian solution as it is driven through a bioprinting process. The left figure shows that the major velocity change in the fluid at the contraction of the needle is along the flow direction, which causes significant extensional stress on the cells; in contrast, the major velocity change in the needle tip (right figure) is perpendicular to the flow, which results in significant shear stress on the cells. Based on these observations, it is rational to assume that cell damage in the contractive

area is mainly caused by extensional stress but in the needle tip is mainly caused by shear stress. Thus, the total cell damage caused by both external and shear stresses during the bioprinting process can be expressed by

$$D_t = D_{et} + (1 - D_{et}) \cdot D_{st}. \tag{5.2}$$

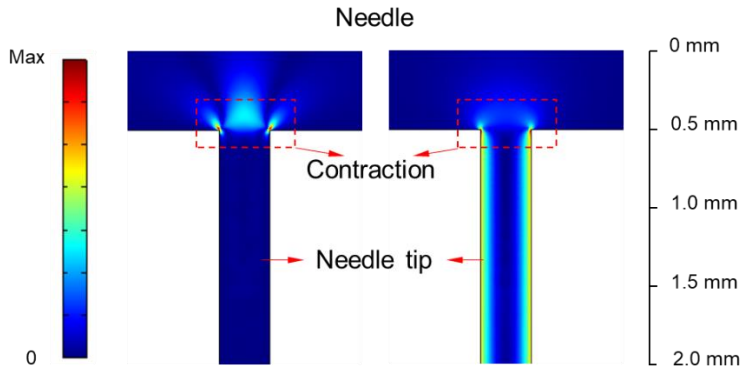

Figure 5. 2 Simulation of extensional (left) and shear (right) rate of a non-Newtonian fluid inside a bioprinting needle

5.3.2 Shear stress-induced cell damage in bioprinting

The development of a shear stress-induced cell damage law aims to bridge the relation between cell damage and shear stress within a certain exposure time. Previously reported models to describe cell damage induced by shear stress include power law models and polynomial models [19, 20]. These have simple formations and are good at fitting experimental data when sufficient data are available. However, they are limited to accurately represent and predict the trend with upper and lower limits, such as a theoretical value of cell damage from 0 to 100%. Exponential equations and modifications thereof have been used in statistics for their inherent ability to confine the output of an equation within a numerical range. Previous cell damage evaluations show that the trend in cell damage is similar to an exponential equation as stress or exposure time increases [13, 20]. Therefore, an exponential-based equation is used in this chapter to describe cell damage related to both stress and exposure time:

$$D(\tau, t) = \left(1 - e^{f_2(\tau,t)}\right) \times 100\%, \tau, t \geq 0, f_2(\tau, t) \leq 0. \tag{5.3}$$

Cell damage is expected to increase from zero (no shear stress or exposure time) to 100% as the applied stress or exposure time increases. For shear stress-induced cell damage, the cell damage law can then be written as

$$D_s(\tau_s, t_s) = (1 - e^{-a_1 \cdot {\tau_s}^{b_1} \cdot {t_s}^{c_1}}) \times 100\%, \quad (5.4)$$

where a_1, b_1, and c_1 are constant coefficients that can be determined from experiments. The format of this cell damage law is reasonable because the percent damaged cells follows the expected trend, growing from 0 to 100%. Also, it mathematically guarantees the theoretical situation that no cell damage occurs if either τ_s *or* t_s equals zero.

Biomaterial-cell suspensions show non-Newtonian flow behavior. Thus, a power law model is often used [21]:

$$\tau_s = K\gamma^n + \tau_0, \quad (5.5)$$

where K is the consistency index [Pa·s^n], n is the dimensionless flow behavior index, γ is the shear rate [s^{-1}], and τ_0 is the yield stress.

Based on the assumptions for biomaterials and cells employed in bioprinting, the pressure drop in the needle can be given by

$$\Delta P = P - P_{en}, \quad (5.6)$$

where P is the applied air pressure and P_{en} is the pressure drop at the abrupt contraction area of the needle. Based on the force balance and assumptions, the shear stress distribution along the radial direction in the needle tip can be written as

$$\tau_s(r) = \frac{\Delta P r}{2L}, \quad (5.7)$$

where L is the length of the needle tip [11 mm] and $\tau_s(r)$ is the shear stress at radial position r. For cell suspensions characterized by Eqn. 5.5, the flow velocity V in the needle tip can be given by [13]

$$V(r) = \frac{n}{n+1}\left(\frac{\Delta P R}{2KL}\right)^{\frac{1}{n}} \cdot R\left[1 - \left(\frac{r}{R}\right)^{\frac{n+1}{n}}\right], \quad (5.8)$$

where R is the inner diameter of the needle tip. The velocity of a cell suspension in the needle tip is known to be a function of radius r. Thus, the length of time required for cells to go through the needle tip will differ for different radial distributions, according to

$$t_s(r) = \frac{L}{V(r)}. \quad (5.9)$$

For a cell suspension with a given cell density, the total cell number and the damaged cell number in the needle tip can be calculated if the needle size is known. By employing the cell damage law, the percent cell damage caused by shear stress in the needle tip, D_{st}, can be calculated using

$$D_{st}(\tau_s, t_s) = \frac{2\int_0^R r \cdot D_s(\tau_s, t_s) dr}{R^2} \times 100\%. \quad (5.10)$$

5.3.3 Extensional stress-induced cell damage in bioprinting

The extensional stress caused by the sudden velocity change in the direction of flow as the fluid is flowing through the abrupt contraction of the bioprinting needle can be determined if the velocity change and extensional viscosity of the fluid are known [22]. Unlike a Newtonian fluid in which the extensional viscosity is proportional to the shear viscosity, the extensional viscosity for a non-Newtonian fluid is complicated. Although many extensional rheometers have been made to measure extensional viscosity, their use is time-consuming and obtaining the viscosity over a wide range of extensional strain rates is challenging [23, 24].

When the fluid flows across the contraction of a needle, the entry contraction flow is subject mainly to extensional deformation, and an entry pressure drop accordingly occurs [25]. Compared to methods to measure extensional viscosity, those for the measurement and calculation of entry pressure drop are easy to perform [26]. If the pressure drop is known, the average extensional stress can be determined using the following equation if the geometrical angle of the contraction is close to 90° [27, 28]:

$$\tau_e = \frac{3}{8}(n+1)P_{en}, \quad (5.11)$$

where *n* is the flow behavior index, which can be determined from a flow behavior test.

Capillary rheometers can be employed to detect the pressure drop of a fluid at the contraction of the capillary [29]. The fluid is extruded with a prescribed shear rate from circular capillaries that have various length-diameter ratios (*L*/*D*), and the contraction pressure drop then determined with Bagley's method, which plots the pressure drop at a constant shear rate versus *L/D* ratio by imposing a linear fit on the data [30]. The linear Bagley plot is then extrapolated to zero, and that point is recognized as the entrance pressure drop.

The conditions of bioprinting are similar to those of a capillary rheometer, where cell suspensions are extruded through a capillary-like cylindrical needle with a large *L/D* ratio. Therefore, Bagley's method to determine the pressure drop can be applied to bioprinting. However, this can be challenging for experimental methods that use trial-and-

error to adjust the dispensing pressure so as to achieve the proposed shear rate when needles with different *L/D* values are used, and becomes more time-consuming if many bioprinting conditions (e.g., printing pressures, needle diameters, and biomaterial-cell suspension types) are examined.

Compared to experimental methods, simulation analysis, once verified by experiments, is more efficient and economical. In this study, computational fluid dynamics (CFD) is applied to simulate the flow profile (i.e., mass flow rate) of biomaterial-cell suspensions inside the printing needle [31]. After verification, the simulated data are then used to determine the pressure drops with the assistance of Bagley's method.

As the cell suspension is treated as an incompressible fluid, the conservation of mass and momentum equations are used as the governing equations:

$$\nabla \cdot \mathbf{u} = 0, \tag{5.12}$$

$$\rho(\mathbf{u} \cdot \nabla \mathbf{u}) = -\nabla P + \mu \nabla^2 \mathbf{u} + \mathbf{F}, \tag{5.13}$$

where **u** is the velocity vector, ρ is the fluid density, μ represents the viscosity of the fluid, *P* is pressure, and **F** is external force. Considering the small value of the Reynolds number of biomaterial-cell suspensions flowing in the needle [16], the flow profile is solved in a laminar stationary state.

Assuming the time the cells are exposed to extensional stress can be neglected due to the quite limited effective contractive length (Figure 2), the cell damage law (Eqn. 5.3) for extensional stress can be modified and derived as

$$D_{et}(\tau_e) = (1 - e^{-a_2 \cdot {\tau_s}^{b_2}}) \times 100\%, \tag{5.14}$$

where a_2 and b_2 are constant coefficients that can be obtained using experimental data.

5.4 Materials and Methods

5.4.1 Cell culture

A Schwann cell line (RSC96) and a myoblast line (L8) purchased from the American Type Culture Collection were each maintained in a 5% CO_2, humidified incubator at 37 °C with standard Dulbecco's modified Eagle's medium (DMEM; Sigma-Aldrich) supplemented with 10% fetal bovine serum (FBS; Gibco, Life Technologies) for culturing.

5.4.2 Materials preparation

Medium viscosity sodium alginate powder (alginic acid sodium salt from brown algae, A2033, Sigma-Aldrich) was first dissolved in deionized water to form a 0.2% w/v alginate solution. A 0.22-μm bottle-top filter (Thermo Fisher Scientific) was applied to sterilize the dissolved alginate solution, and the filtered medium then transferred into a −40 °C freezer for 24 h and later freeze-dried (FreeZone Freeze Dryer; Labconco). The sterilized alginate was thoroughly dissolved in calcium-free DMEM (Gibco, Life Technologies) with 1% antibiotic (100× penicillin and streptomycin; Sigma-Aldrich) added to form a 2.0% w/v alginate stock solution. Trypan blue was purchased from Sigma-Aldrich. Calcein AM, ethidium homodimer-1, propidium iodide (PI), and Hoechst 33342 were purchased from AnaSpec. Annexin V-FITC and associated binding buffer were purchased from Biovision. Ultrapure salmon sperm DNA solution was purchased from Thermo Fisher Scientific.

5.4.3 Characterization of cell damage under shearing using a plate-and-cone rheometer

Cell damage was evaluated using a cone-plate type rheometer (RVDV-III; Brookfield) with a CP-52 spindle cone at room temperature (~22 °C). RSC96 and L8 cells were separately mixed with alginate solution to obtain 1.5% uniform alginate/cell suspensions with a cell density of 1×10^6 cells/mL. The rheometer was placed within a laminar flow sterile air hood and wiped with 70% ethanol three times in the sterile atmosphere. The cone and plate of the rheometer (which directly contact the cells) were immersed in 70% ethanol for 10 min and then dried for another 15 min in the hood before use. A 2-mL prepared cell suspension was then transferred into the plate of the rheometer and subjected to varying shear rates (10, 40, 80, 120, and 160 rpm) for 10, 30, 60, and 120 s at room temperature. To examine cell damage, 100 μL of the sheared cell suspension were removed and mixed with 30 μL of 0.2% trypan blue (a dye to stain the damaged cells with ruptured membranes), and the number of damaged cells manually counted with the assistance of an optical microscope (Leica Microsystems). Cell damage was examined on four suspensions, and the percent cell damage calculated as the number of damaged cells

divided by the total cell number. Cell suspensions retained in tubes were treated as positive controls. The difference in cell damage between the sheared and control groups was attributed to the corresponding shear stress.

5.4.4 Characterization of cell suspension flow behavior using the rheometer

The flow behaviors of alginate solution, the alginate-RSC96 cell suspension, and the alginate-L8 cell suspension were evaluated using the same rheometer at room temperature. A 2-mL cell suspension containing 1.5% alginate and a cell density of 1×10^6 cells/mL was loaded into the gap between the cone and plate of the rheometer for each test. During shearing, the cone was pre-set to rotate at a series of angular speeds, and the associated shear stress recorded. Five samples were tested for each cell type, with the average reported herein.

5.4.5 Characterization of mass flow rate of cell suspensions in bioprinting

Alginate-RSC96 cell and alginate-L8 cell suspensions each with a cell density of 1×10^6 cells/mL were separately loaded into the syringe of the bio-plotter (3D bio-plotter, EnvisionTEC, Germany) to determine the mass flow rate. Suspensions were driven under varying dispensing pressures (50, 100, 200, and 400 KPa) through a 200-μm needle as well as through needles of varying diameters (100, 200, 250, and 330 μm) at a fixed bioprinting pressure of 200 KPa. The mass flow rate was then examined using a digital weight scale. By controlling the printing time, three printed droplets for each printing condition were weighed and the average thereof used to represent the flow rate.

5.4.6 Simulation of flow profiles of alginate-cell suspensions in bioprinting

Due to the structural symmetry of the bioprinting needle, two-dimensional representations of needles were built instead of 3D structures using CFD software (COMSOL, Stockholm, Sweden). The geometry was then fitted with grids, with refined grids in the region of the wall of the tip and contraction. Flow behaviors of cell suspensions and dispensing pressures were given as initial conditions. The boundary conditions were specified such that the pressure at the exit of needle was equal to ambient air pressure, and there was no slip flow at any needle wall. After initial simulations, the meshed grid was

refined until the magnitude of the velocity for different areas in the domain did not change significantly.

The simulated mass flow rate could then be obtained from the solved flow model. Once verified by experiments, the flow profile of each suspension could be obtained, and thus the pressure drop at the contraction of the needle determined with the help of Bagley's method.

5.4.7 Characterization of cell damage in the bioprinting process

Cell suspensions with a cell density of 1×10^6 cells/mL were loaded into a sterilized syringe of the 3D bio-printer for printing. The suspensions were first extruded under varying dispensing pressures (50, 100, 200, and 400 KPa) through a cylindrical needle with a 200-μm tip diameter. Cells were stained both immediately and 6 h after bioprinting with Hoechst 33342, Annexin V-FITC, and PI. For immediate staining, 100 μL of the bio-printed cell suspensions were transferred into 15-mL tubes containing 3 mL of cell culture medium. The solution was uniformly mixed and then centrifuged for 10 min at 1000 rpm. After aspirating the medium, 500 μL of 1X binding buffer with 5 μL Annexin V-FITC, 25 μg/mL PI, and 1 μg/mL Hoechst 33342, which selectively stain damaged cells (injured cell membrane), dead cells (cell nucleus), and cell DNA, respectively, were added to the tube for 10 min in a 37 °C incubator. Cells were then transferred onto a glass slide and analyzed under a fluorescence microscope (Axioimager M1, Carl Zeiss). Three samples for each bioprinting pressure were examined, and the number of damaged cells, dead cells, and total cells manually counted from images randomly taken from three fields of each glass slide (three slides for each testing sample) using ImageJ software (National Institutes of Health, Bethesda, Maryland, USA).

For the 6 h examination, a 100-μL cell suspension was first transferred after bioprinting into the well of a 12-well plate that contained 900 μL of cell culture medium. After 6 h in the cell culture incubator, the culture medium in the well was transferred to a 15-mL tube; attached cells were detached using 200 μL trypsin + EDTA (Sigma-Aldrich) and then transferred into the same tube. The cells were examined using the same procedure as described above.

Cylindrical needles of varying diameters (100, 200, 250, and 330 μm) were also considered under a constant printing pressure of 200 KPa. Cell damage was examined immediately and 6 h after bioprinting following the same procedures as described above.

5.4.8 Characterization of cell viability after bioprinting

Alginate-RSC96 cell and alginate-L8 cell suspensions were respectively printed under varying dispensing pressures (50, 100, 200, and 400 KPa) and then cultured in 12-well tissue culture plates. A live/dead assay was applied to evaluate the viability of cells 6, 24, and 72 h after bioprinting. Briefly, calcein AM (1 μg/mL) and ethidium homodimer-1 (0.5 μg/mL), which selectively stain live or dead cells, respectively, were added into the wells with cells. After 20 min staining in the cell culture incubator, the culture plates with stained cells were moved to the fluorescence microscope for image capture (Carl Zeiss Axiovert 100). Cell viability was assessed by counting stained cells on images randomly taken from samples. For each bioprinting pressure, three wells were used for the printed cells, and three random images of each well were taken and analyzed using ImageJ. Viability was calculated as the percent live cells among the total number of live and dead cells.

5.4.9 Characterization of cell proliferation after bioprinting

Total cell number represented by the fluorescent labelling of cell DNA was applied to quantify the proliferation of cells. Before testing, standard values of Hoechst-labeled DNA were investigated followed the procedure reported in [32]. Briefly, serial dilutions of the stock solution of ultrapure salmon DNA were prepared in TNE buffer (10 mM Tris, 1 mM EDTA, 2 M NaCl, pH 7.4). Then, 100 μL of TNE buffer with varying DNA content (20, 50, 200, 500, 2000, or 5000 ng) were pipetted into the wells of a black opaque 96-well plate. An additional 100 μL of TNE buffer with 20 μg/mL Hoechst were added to obtain a solution with a final concentration of 10 μg/mL in 200 μL per well. The fluorescence was measured 15 min later using a fluorescence microplate reader (SpectraMax M2e; Molecular Devices) after the DNA was sufficiently stained. The detected fluorescence values were used to calculate a DNA standard curve.

RSC96 and L8 cells were suspended separately in DMEM plus 10% FBS and counted after trypsinization. Serial dilutions were made in the DMEM solution so that 100 µL contained 1×10^3, 5×10^3, 1×10^4, 2.5×10^4, 5×10^4, 7.5×10^4, 1×10^5, and 1.25×10^5 cells. Wells were seeded with 100 µL of cell solution and the plate incubated for 12 h at 37 °C in 5% CO_2 to allow cell attachment. The culture medium was then gently pipetted out and the remaining cells rinsed once with PBS. The black plate was then moved to a −40 °C freezer for 1 h. After thawing at room temperature, 100 µL of deionized water were added to each well and the plate incubated for another 1 h. Before the examination, 100 µL of TNE buffer with 20 µg/mL Hoechst were added to each well to stain the DNA for 15 min, and then the plate removed to the plate reader. The values obtained were used to calculate a cell standard curve. For both DNA and cell standard curves, five samples were prepared for each DNA amount or cell concentration.

Alginate-RSC96 and alginate-L8 suspensions, both with a cell density of 1×10^6 cells/mL, were dispensed under varying air pressures (50, 100, 200, and 400 KPa). Then 10 µL of the printed suspension was transferred into the well of a black opaque 96-well plate, with subsequent addition of 90 µL of cell culture medium. After culturing for 24 and 72 h, cell DNA were examined following the same procedure of cell standard curve plotting as outlined above; results were recorded from five samples of each printing. The same volume of medium without cells was used as a negative control.

5.4.10 Statistical analysis

Mean values and standard deviation (SD) values of all data were calculated. Statistical significance was determined by ordinary one-way analysis of variance, and multiple comparisons were performed using Tukey's test and GraphPad Prism (GraphPad Software) with an acceptable significance level of $P < 0.05$.

5.5 Results

5.5.1 Cell damage under shearing

Shearing experiments demonstrate that both shear stress and exposure time influence cell damage, as shown in Figure 5.3. For both RSC96 and L8 cells, the percent damaged cells increases as the shear stress increases. Moreover, the percent damaged cells

increases with exposure time for a given shear stress. RSC96 cells appear to be more easily injured by shear force compared to L8 cells because the percent damaged RSC96 cells is higher than for L8 cells under the same shear stress and exposure time, (e.g., at 100 Pa for 10 s, the average damage for RSC96 cells is 2.32 vs. 2.12% for L8 cells; at 1000 Pa and 120 s, the average damage for RSC96 cells is 31.10 vs. 25.49% for L8 cells).

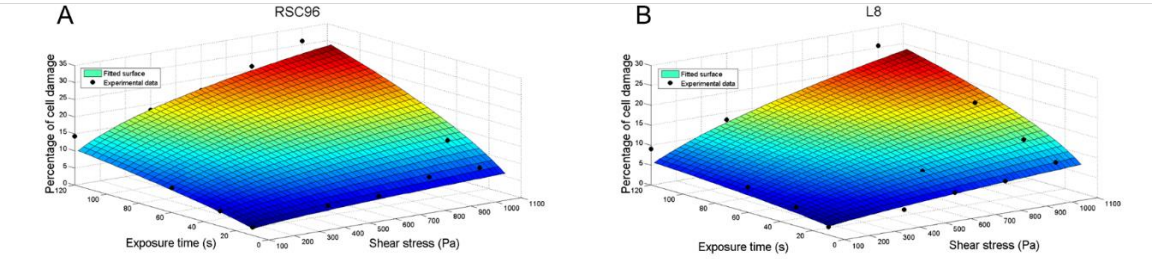

Figure 5. 3 Experimental and model results of shear stress-induced cell damage

Based on the experimental data, the shear stress-induced cell damage law (Eqn. 5.4) was applied to describe the damage, and the fitted cell damage percentages plotted in Figure 5.3. For alginate-RSC96 cells, the percent cell damage is given as,

$$D_{sRSC96}(\tau_s, t_s) = (1 - e^{-3.9\times10^{-4}\times{\tau_s}^{0.48}\times{t_s}^{0.71}}) \times 100\% \quad (5.15)$$

and for L8 cells is given by

$$D_{sL8}(\tau_s, t_s) = (1 - e^{-3.2\times10^{-4}\times{\tau_s}^{0.61}\times{t_s}^{0.52}}) \times 100\%. \quad (5.16)$$

The reliability of the damage laws for RSC96 and L8 cells was verified by fitted R-squared values of 0.93 and 0.91, respectively.

5.5.2 Flow behavior characterization of alginate-cell suspensions

The flow behavior of the alginate-RSC96 and alginate-L8 cell suspensions has been achieved in our previous work [18]. All of the alginate-based solutions demonstrate non-Newtonian flow behavior with respect to non-linear relations of shear stresses and shear rates. At the low concentration of alginate used, the yield stress τ_0 was taken to be zero [33]. Therefore, a power-law model (i.e., Eqn. 5.5) can be applied to describe the flow behavior.

A method to calculate the flow behavior directly based on the bioprinting flow rate can be used if the printed solution can be expressed by a power-law flow model [21]. Compared to analyzing flow behavior from a rheometer test, this method is more accurate

and efficient for obtaining flow behavior parameters (K and n) by eliminating the errors induced by the inconsistent experimental environments of the rheometer and bioprinting tests. With the mass flow rates obtained and shown in Table 5.1, K and n values for RSC96 cells, written as K_R and n_R, were calculated to be 30.01 and 0.34, respectively; for the alginate-L8 cell suspension, K_L and n_L equaled 21.64 and 0.38, respectively.

Table 5. 1 Measured mass flow rates under different bioprinting conditions

Measured flow rate	Applied air pressure (KPa)				
	50	100	200	300	400
RSC96 cell suspension (g/s)	$(2.0\pm0.5)\times10^{-4}$	$(1.9\pm0.34)\times10^{-3}$	$(2.1\pm0.52)\times10^{-2}$	$(4.8\pm0.56)\times10^{-2}$	$(1.1\pm0.12)\times10^{-1}$
L8 cell suspension (g/s)	$(3.5\pm0.93)\times10^{-4}$	$(2.2\pm0.28)\times10^{-3}$	$(1.2\pm0.47)\times10^{-2}$	$(3.9\pm0.71)\times10^{-2}$	$(8.3\pm1.45)\times10^{-2}$

5.5.3 CFD flow profile verification using mass flow rates

The experimental flow rates suggest that larger volumes of cell suspensions can be dispensed when the dispensing pressure or the diameter of the needle is larger, as shown in Figure 5.4. COMSOL simulation was conducted to represent the flow rate of the cell suspension, with the results plotted in Figure 5.4. The simulated mass flow rates match the experimental flow rates well, indicating the COMSOL model is reliable for predicting the mass flow rate of cell suspensions under varying bioprinting conditions, and appropriately represents the flow pattern of cell suspensions.

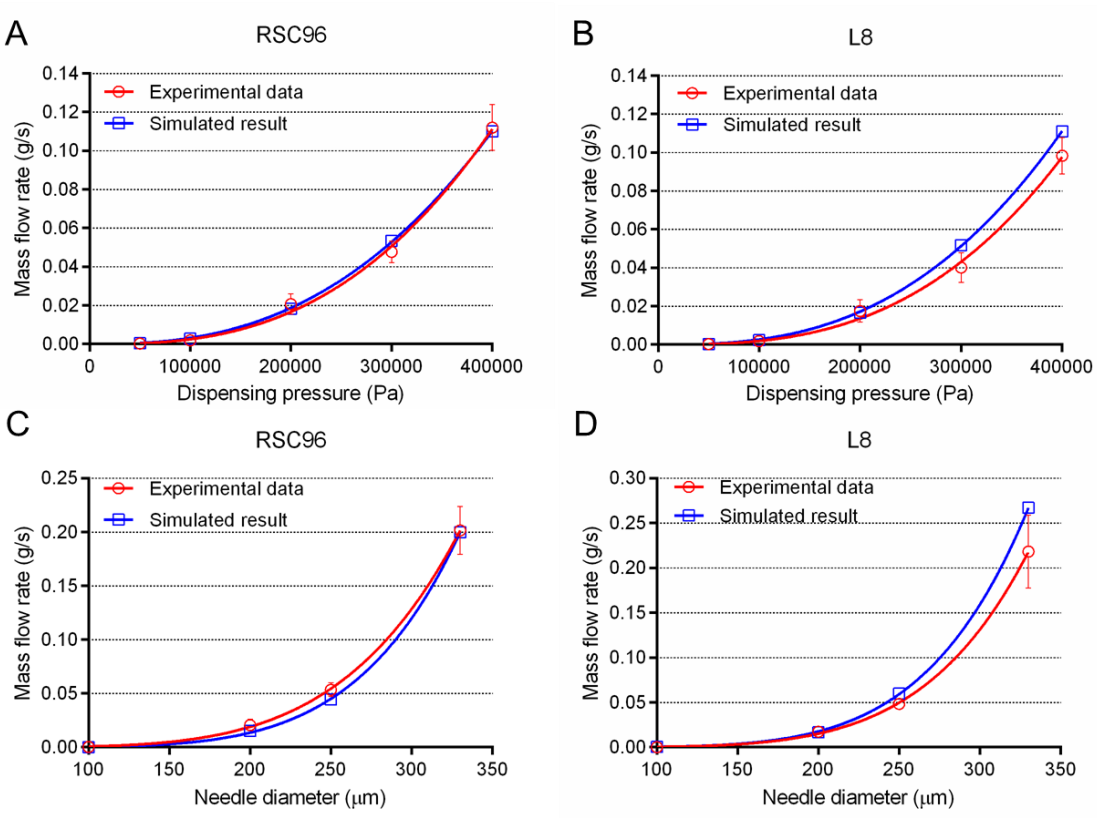

Figure 5. 4 Experimental and simulated mass flow rate of bioprinting: mass flow rate of (A) alginate/RSC96 suspension and (B) alginate/L8 suspension at varying dispensing pressures from 50 to 400 kPa (fixed needle diameter of 200 μm); mass flow rate of (C) alginate/RSC96 suspension and (D) alginate/L8 suspension at varying needle sizes from 100 to 330 μm (fixed pressure of 200 kPa).

5.5.4 Pressure drops at the contraction of the bioprinting needle

Verified by the experimental results, the CFD flow model combined with Bagley's method was then adopted for determining the pressure drop at the abrupt contraction of the needle during bioprinting. The results shown in Table 5.2 indicate that both higher air pressure or larger needle diameter can lead to a higher pressure drop at the contractive region for our cell suspensions, which results in larger extensional stress as from Equation (5.11). The calculated extensional stresses displayed in Table 5.2 are used later to evaluate extensional stress-induced cell damage.

Table 5. 2 Pressure drops and related extensional stresses under varying bioprinting conditions

Dispensing pressure (KPa)	Needle diameter (μm)	Pressure drop (Pa) / Extensional stress (Pa)	
		RSC96	L8
50	200	843 / 424	846 / 438
100		1683 / 846	1689 / 874
200		3363 / 1690	3369 / 1743
400		6571 / 3302	6629 / 3431
200	100	1803 / 906	1804 / 934
	200	3363 / 1690	3369 / 1743
	250	4438 / 2230	4454 / 2305
	330	5699 / 2864	5767 / 2984

5.5.5 Cell damage introduced in the bioprinting process

Cell damage after bioprinting was measured by counting fluorescently labeled cells (see section 5.4.7), with the results shown in Figure 5.5. Both injured cells (green only, indicating injured membrane) and dead cells (green and red, indicating injured membrane and nucleus) are observed after bioprinting (Figures 5.5B, D, F, and H), indicating that cells are damaged during bioprinting by the process-induced stresses. The results also show that larger bioprinting pressures damage more cells (including both injured and dead cells), presumably due to the higher process-induced shear and extensional stresses. Figures 5.5I to L show that the percentage of dead cells is higher compared to injured cells, which suggests that cells are sensitive to the process-induced stresses and their status can be quickly altered from unaffected to dead within the bioprinting period. The number of damaged RSC96 cells is slightly higher than for L8 cells under the same conditions, which suggests that RSC96 cells are more sensitive to process-induced stresses than L8 cells.

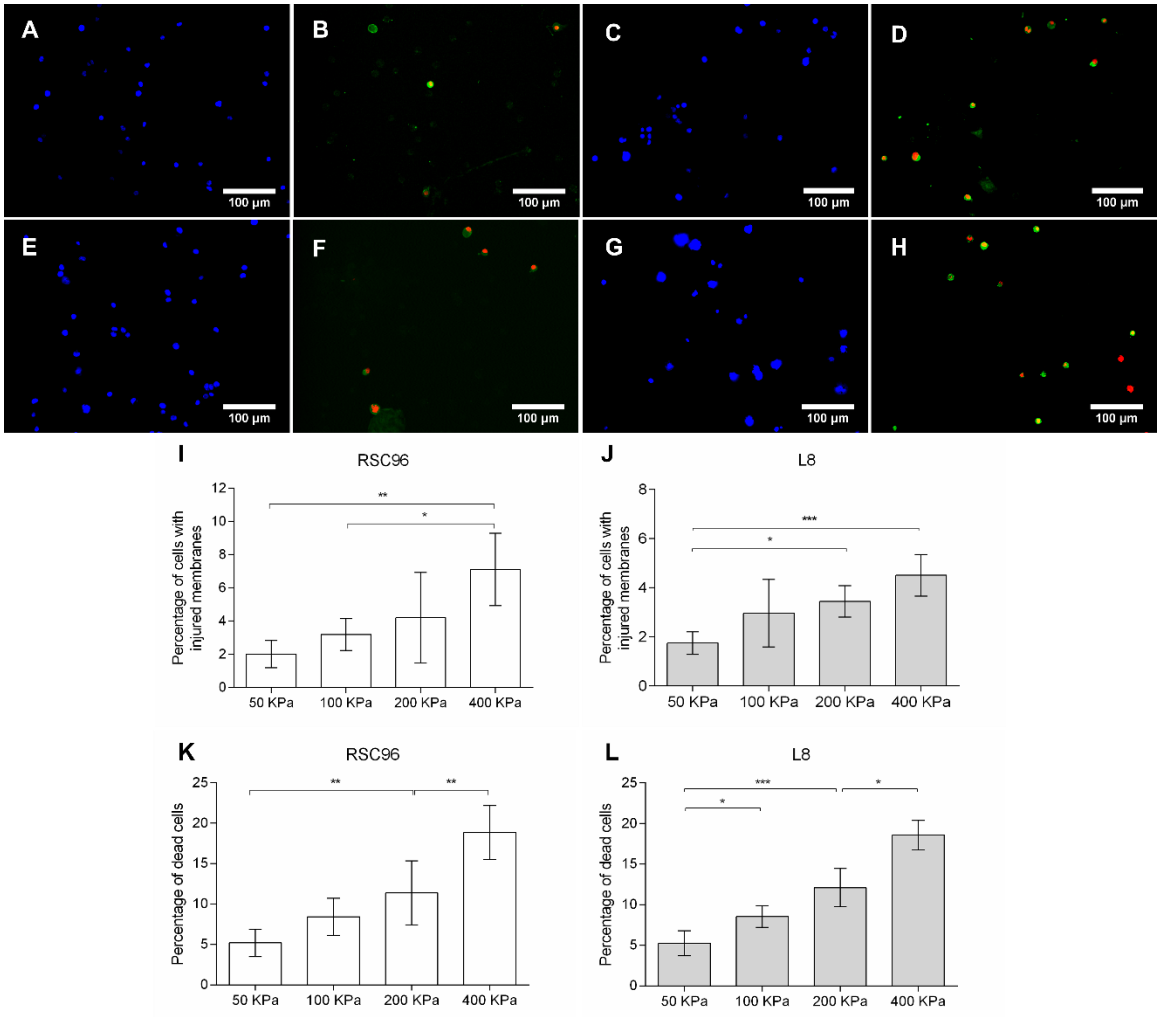

Figure 5. 5 Evaluation of cell damage immediately after bioprinting: Hoechst stained RSC96 cells printed at (A) 100 kPa and (C) 400 kPa; Damaged and dead RSC96 cells stained by Annexin V-FITC and PI printed at (B) 100 kPa and (D) 400 kPa; Hoechst stained and Annexin V-FITC/PI stained L8 cells printed at 100 kPa (E, F) and 400 kPa (G, H), respectively; percent injured (I, J) and dead (K, L) RSC96 and L8 cells, respectively, for different printing pressures.

The percent damaged cells due to the bioprinting process and shear stress in bioprinting are given in Figure 5.6. Cell damage introduced by shear stress during bioprinting can be calculated using Equations (5.6)-(5.10), as well as the established cell damage law (Eqns. 5.15 and 5.16). For both RSC96 and L8 cells, Figure 5.6 shows that the percent shear stress-induced cell damage in bioprinting is low, and decreases slightly as

the bioprinting pressure increases from 50 to 400 KPa. However, the total percent damaged cells is significantly higher than can be expected from shear stress alone, which indicates additional factors contribute to cell damage during bioprinting. This additional factor is believed to be extensional stress.

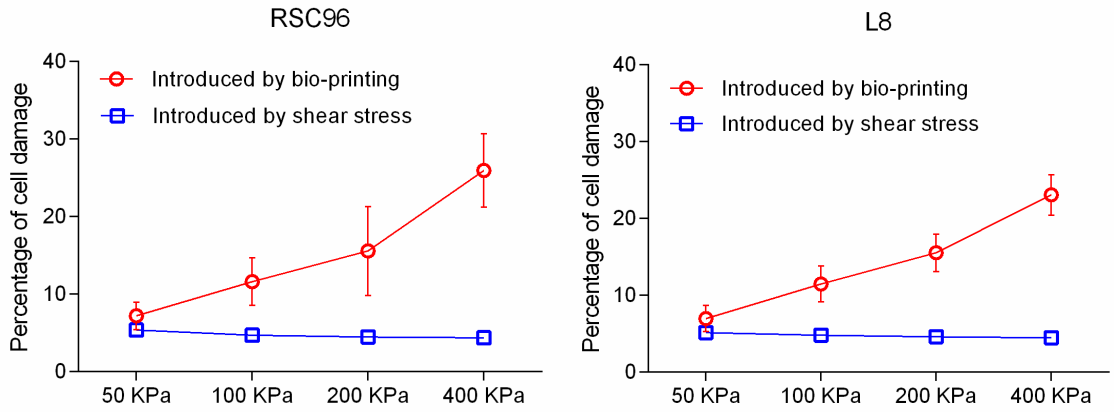

Figure 5. 6 Percent bioprinting process-induced and shear stress-induced cell damage

The percent cell damage introduced by extensional stress can be obtained using results from Figure 5.6 and Equation (5.2), and the extensional stress-induced cell damage law for both RSC96 and L8 cells in Equation (5.14) can be rewritten as

$$D_{etRSC96} = \left(1 - e^{-5.46\times10^{-5}\times{\tau_e}^{1.04}}\right) \times 100\%, \tag{5.17}$$

$$D_{etL8} = \left(1 - e^{-1.35\times10^{-4}\times{\tau_e}^{0.91}}\right) \times 100\%, \tag{5.18}$$

with R-squared values of 0.98 and 0.97, respectively.

Cell damage after passing through needles of varying diameters (under the same dispensing pressure of 200 KPa) was also evaluated immediately after bioprinting, and the percent cell damage recorded and used to verify the developed method. Figure 5.7 shows the experimental cell damage and predicted results considering both extensional and shear stresses. The predicted results match the experimental data for both RSC96 and L8 cells well, which confirms the reliability and accuracy of our method for predicting cell damage for a wide range of bioprinting conditions.

Cell damage was also evaluated 6 h after bioprinting. Most damaged cells at this time point are dead; very few merely injured cells are seen in the fluorescent microscopy images, indicating that the status of injured cells changes within 6 h of printing.

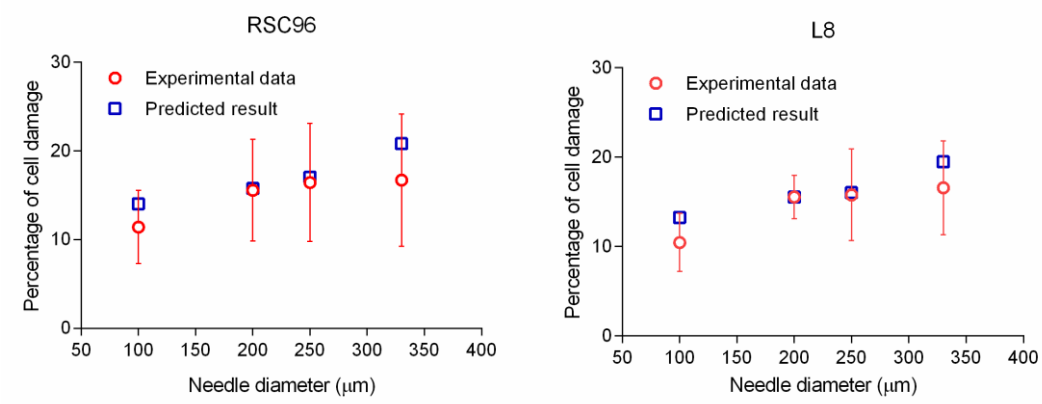

Figure 5. 7 Experimental and predicted cell damage for cell suspensions printed from needles with various diameters

5.5.6 Cell viability and proliferation after bioprinting

The viability of RSC96 and L8 cells was evaluated 6, 24, and 72 h after bioprinting, with the results given in Figure 5.8. More cells are dead for higher bioprinting pressures at each time point. Compared to the cell damage evaluation in section 5.5.5, the percentages of dead cells for these two cell types are lower than when tested immediately after bioprinting (Figures 5.5 and 5.8). For RSC96 cells, the average percent damaged cells immediately after bioprinting for dispensing pressures of 50, 100, 200, and 400 KPa were 7.20, 11.62, 15.57, and 25.95% but 6 h later were 6.79, 10.42, 14.49, and 23.45%, respectively. For L8 cells, the immediate values for cell death were 6.99, 11.70, 15.53, and 23.08% but after 6 h were 6.53, 11.67, 15.00, and 20.13%, respectively. The percentage of dead RSC96 cells within 72 h did not change significantly regardless of printing pressure, but was greatly reduced for L8 cells after 72 h. This indicates the cell reproduction rate of RSC96 cells is close to its death rate during post-bioprinting culture, while L8 cell reproduction appears to exceed cell death during this period.

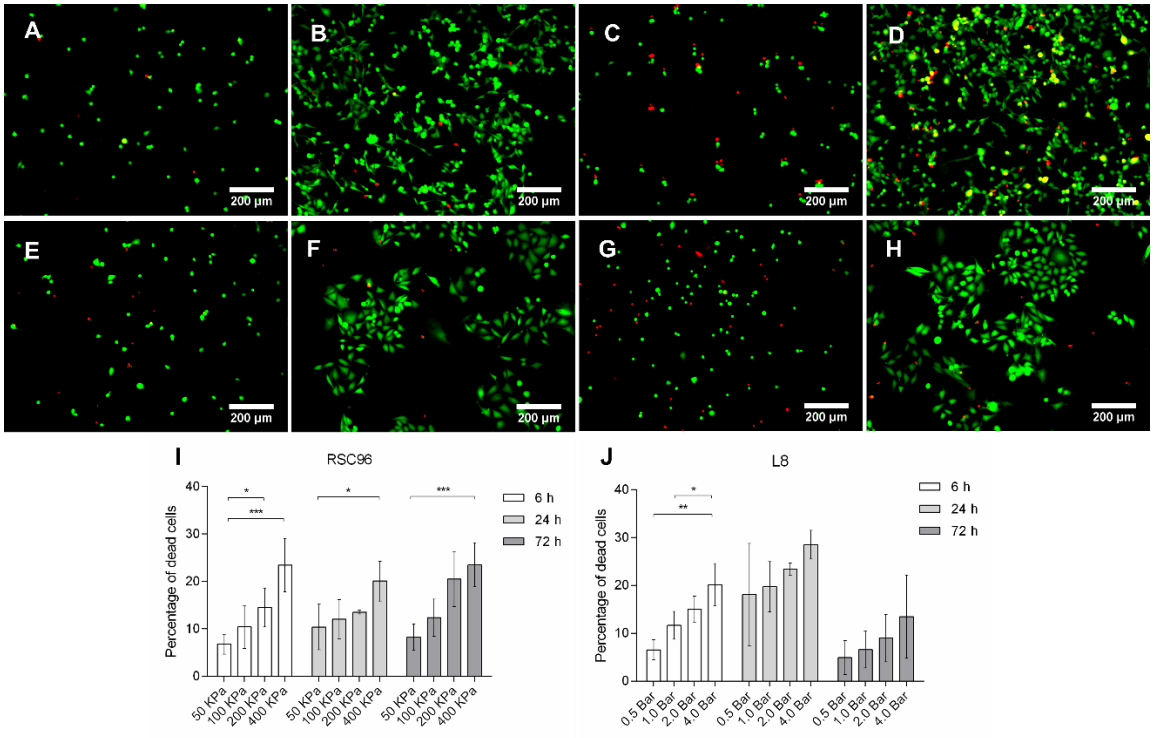

Figure 5. 8 Live/dead assay of cell viability in the first 72 h after bioprinting: viability of RSC96 cells printed at (A, B) 50 kPa or (C, D) 400 kPa after 6 and 72 h, respectively; viability of L8 cells printed at (E, F) 50 kPa or (G, H) 400 kPa after 6 and 72 h, respectively; statistical summary of percent dead (I) RSC96 and (J) L8 cells 72 h after printing.

Linear relationships between fluorescent DNA staining and cell number are shown in Figures 5.9A to C. Based on these correlations, absorbance values can be used to represent the number of cells and thus cell proliferation. The fluorescence values in Figures 5.9D and E confirm that bioprinting reduces the number of living cells, and higher bioprinting pressures can bring about more cell damage. Moreover, the proliferation rates of cells after bioprinting decrease compared to control cells from 24 to 72 h (e.g., for RSC96 cells printed at 50 and 400 KPa, the ratios of fluorescence are 89.49 and 70.93% after 24 h and 82.75 and 67.08% after 72 h, respectively; for L8 cells, the values are 90.37 and 72.67% after 24 h and 86.71 and 71.65% after 72 h, respectively), which suggests the proliferation of surviving cells is reduced after bioprinting.

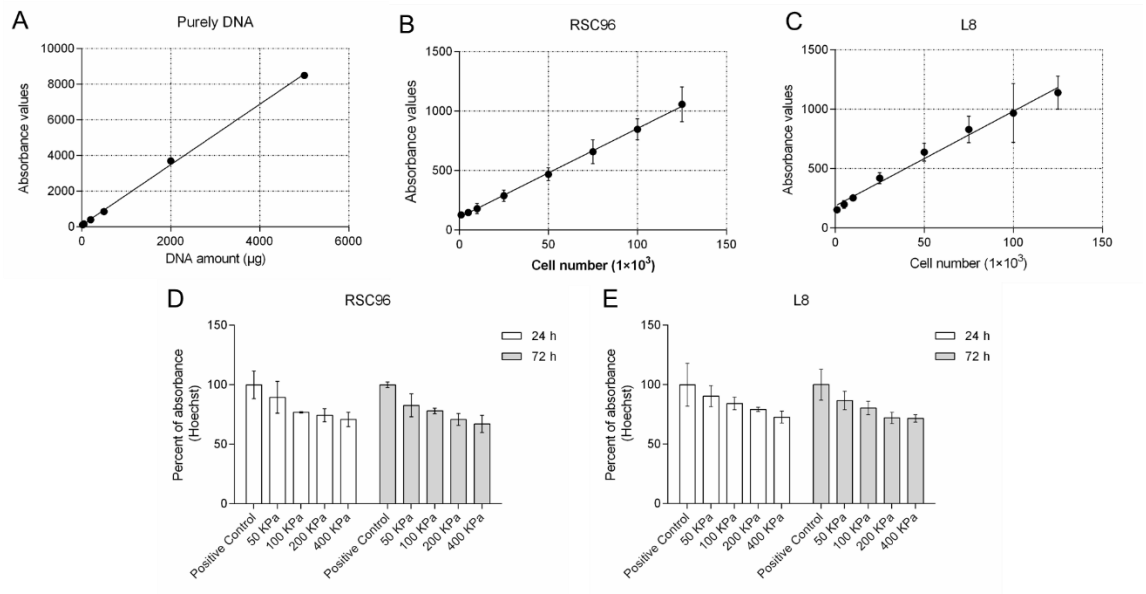

Figure 5. 9 Cell proliferation assay: standard curves of the amount of (A) pure DNA, (B) RSC96 cell number, and (C) L8 cell number versus fluorescence; absorbance of (D) RSC96 cells and (E) L8 cells printed at varying pressures and tested at 24 and 72 h.

5.6 Discussion

Alginate is a biological material derived from natural seaweed [34, 35]. It is a low-cost and biocompatible material that can be used with many cell types to maintain cell viability [36, 37]. DMEM is a general nutrient medium that has been extensively used for cell culture. Therefore, the use of DMEM-dissolved alginate solution in this study was not expected to result in any adverse effects on cell survival, and cell damage could therefore be attributed to the bioprinting process. Note that the standard DMEM formulation includes a physiological level of calcium ions, which can react with alginate to form alginate hydrogel [17, 38]. To avoid this reaction, calcium-free DMEM was used.

In this study the effect of shear stress on cell damage was evaluated using trypan blue, a dye that can traverse the membrane of injured cells [39]. Because a large number of testing groups and samples were prepared for shear stress-induced cell damage experiments, the use of trypan blue is efficient and economical. However, trypan blue stains all damaged cells with injured membranes, and is unable to distinguish between merely injured and dead cells. This limits our investigation of cell status. The more sophisticated utilization of a panel of fluorescent dyes including Hoechst, PI, and Annexin

V can separately identify all cells, dead cells, and injured cells with broken membranes. Therefore, cell status can be distinguished more clearly and studied statistically.

Our experimental results verify that bioprinting process-induced stresses are the major factors that introduce cell damage, because the cell membrane of both injured and dead cells were recognized using Annexin V but few cells were stained by PI only. The results also show that most damaged cells are dead immediately after bioprinting, indicating they are sensitive to bioprinting process-induced stresses; furthermore, those cells that are injured immediately after printing advance from injury to death very quickly.

Cells derived from different tissue components have various physical, chemical, and biological properties [40]. For example, cells in soft or mineralized tissues subject to uniform situations of mechanical stress transmission and sensation would have different responses to external stimulation. Estimates of cell properties indicate that the elastic modulus of isolated cells generally ranges from 0.1 KPa (alveolar epithelium) to an approximate upper limit of 40 KPa (myocytes) [41]. The magnitude of the elastic modulus is determined by diverse cell molecular structures, such as the cell membrane and cytoskeleton, and can determine the ability of different cell types to withstand stresses and recover their normal phenotype [42, 43]. The present study shows that Schwann cells (RSC96) are weaker than myoblasts (L8) because more RSC96 cells are damaged under similar mechanical stresses. This can largely be explained by the inherent elastic nature of these cell types. Schwann cells are the major glial cells in the peripheral nervous system and have inherently weak elastic properties compared to cells from other tissues (e.g., muscle) [36, 44]. Thus, it is reasonable to expect that Schwann cells will be more susceptible to mechanical damage.

The bioprinting process involves both shear and extensional stresses, which are acting on cells as the cell suspensions are forced to flow. Establishing a relationship between these stresses and cell damage is important for understanding the mechanism of cell damage introduced by the bioprinting process and the performance of cells after bioprinting. Here, a novel method was developed to establish the relation between both shear and extensional stresses and cell damage. The results indicate that shear and extensional stresses can introduce cell damage depending on the magnitude of the stresses and exposure time. Higher pressures applied during bioprinting cause a larger shear stress

in cells travelling through the needle tip; on the other hand, the exposure time as they flow through the needle simultaneously decreases. This explains why less shear stress-induced cell damage is observed when higher bioprinting pressures are used (Figure 5.6). Cells appear to be more sensitive to extensional stress because, at the same pressure, extensional stress causes a higher percent cell damage over a much shorter time compared to that introduced by shear stress (Figures 5.3, 5.5, and 5.6). Therefore, reducing the extensional stress during bioprinting is important to improve the viability of printed cells.

Evaluating the effect of extensional stress that occurs at the abrupt contraction of flow on cell damage requires information about the flow profile at that region and the percent cell damage introduced by the stress. As the flow at the contraction of the needle is complicated, in this chapter we simplified the situation to try and determine the average extensional stress. This is reasonable because we obtained statistical results for cell damage from bulk cell suspension flow under various conditions. If the aim is to investigate the effect of extensional stress on a single cell during bioprinting, then the dynamic flow profile of each streamline at the contraction must be considered.

A cell damage law must be reliable with acceptable error, must ensure that the percent damage is between 0 and 100%, and should have incremental trends in percent cell damage as the magnitude of stress and exposure time increases from zero to infinity. Based on the experimental results, exponential functions were applied to describe the cell damage introduced by shear and extensional stresses and performed according to expected incremental trends with acceptable errors.

We examined three cell states after bioprinting: unchanged cells with regular phenotypes, cells that survived but are injured or quiescent, and dead cells. The immediate and 6 h cell damage tests show that most injured cells remain quiescent and die within 6 h. As the total percentage of damaged cells at 6 h is slightly lower than immediately after bioprinting, we believe some injured cells have the ability to recover to their regular phenotypes [12, 18]. This assumption is also supported by live/dead assay results 6 h after bioprinting. The cell proliferation assay showed that the proliferation rate of bio-printed cells is slower than non-printed cells under different bioprinting conditions within 72 h. This demonstrates that most living cells maintain their ability to proliferate after bioprinting, while some cells are alive but injured and may lose this function.

Our method represents an advance in predicting cell damage; only the flow behaviors of RSC96 and L8 cell suspensions and the printing conditions are required, which greatly simplifies the experimental procedures to evaluate cell viability in 3D bioprinting. The model clearly points out that high cell viability can be obtained if the shear or extensional stresses are small. One way to reduce the stresses is to use a tapered (instead of cylindrical) needle due to the lower dispensing pressure required if the bioprinting flow rate is fixed [45, 46].

5.7 Conclusions

The cell damage that occurs in the 3D bioprinting process reduces the viability and functioning of cells within the printed construct. Improving the viability of cells thus becomes important. This paper characterized the bioprinting process-induced cell damage for RSC96 and L8 cells and, and based on the results, developed a novel method that considers not only the process-induced shear stress but also the extensional stress to describe the cell damage in bioprinting. The model illustrates the importance of extensional stress on cell damage. Limited cell damage was observed at low bioprinting pressures, where the effect of shear stress was dominant; however, more cell damage occurred at higher pressures due to extensional stress. Moreover, this study characterized the type of cell damage as well as the viability and proliferative functions of printed cells. Dead cells constitute a large proportion of the total number of damaged cells, with most injured cells dying within 6 h of printing. The proliferation rate of printed cells is slightly lower than non-printed cells, demonstrating that bioprinting can affect the ability of some printed cells to proliferate.

The established models satisfactorily describe the bioprinting process-induced cell damage for RSC96 and L8 cells, and thus can be used to predict cell damage and optimize the viability of cells. They also can be applied to analyze the bioprinting process-induced cell damage for other cell types; however, modifications may be needed to consider other factors, such as cell-cell and cell-materials interactions, if they become significant with respect to cell damage.

5.8 References

[1] Murphy SV, Atala A. 2014 3D bioprinting of tissues and organs. *Nat Biotechnol*. 32 773-85.

[2] Knowlton S, Onal S, Yu CH, Zhao JJ, Tasoglu S. 2015 Bioprinting for cancer research. *Trends Biotechnol*. 33 504-13.

[3] Rajaram A, Schreyer D, Chen D. 2014 Bioplotting alginate/hyaluronic acid hydrogel scaffolds with structural integrity and preserved schwann cell viability. *3D Print Addit Manuf*. 1 194-203.

[4] England S, Rajaram A, Schreyer DJ, Chen X. 2017 Bioprinted fibrin-factor XIII-hyaluronate hydrogel scaffolds with encapsulated Schwann cells and their in vitro characterization for use in nerve regeneration. *Bioprinting*. 5 1-9.

[5] Ozbolat IT, Hospodiuk M. 2016 Current advances and future perspectives in extrusion-based bioprinting. *Biomaterials*. 76 321-43.

[6] Ferris CJ, Gilmore KG, Wallace GG. 2013 Biofabrication: an overview of the approaches used for printing of living cells. *Appl Microbiol Biotechnol* 97 4243-58.

[7] Izadifar Z, Chang T, Kulyk WM, Chen D, Eames BF. 2015 Analyzing biological performance of 3D-printed, cell-impregnated hybrid constructs for cartilage tissue engineering. *Tissue Eng C Methods* 22 173-88.

[8] Hsieh FY, Lin HH, Hsu S. 2015 3D bioprinting of neural stem cell-laden thermoresponsive biodegradable polyurethane hydrogel and potential in central nervous system repair. *Biomaterials*. 71 48-57.

[9] Tian XY, Li MG, Chen XB. 2013 Bio-Rapid-Prototyping of Tissue Engineering Scaffolds and the Process-Induced Cell Damage. *J Biomimet Biomat Biomed Eng Trans Tech Publ.* 17 1-23.

[10] Ouyang L, Yao R, Chen X, Na J, Sun W. 2015 3D printing of HEK 293FT cell-laden hydrogel into macroporous constructs with high cell viability and normal biological functions. *Biofabrication*. 7 015010.

[11] Smith CM, Stone AL, Parkhill RL, Stewart RL, Simpkins MW, Kachurin AM, Warren WL, Williams SK. 2004 Three-dimensional bioassembly tool for generating viable tissue-engineered constructs. *Tissue Eng*. 10 1566-76.

[12] Chang R, Nam J, Sun W. 2008 Effects of dispensing pressure and nozzle diameter on cell survival from solid freeform fabrication-based direct cell writing. *Tissue Eng A* 14 41-48.

[13] Li M, Tian X, Zhu N, Schreyer DJ, Chen X. 2009 Modeling process-induced cell damage in the biodispensing process. *Tissue Eng C Methods* 16 533-42.

[14] Bae YB, Jang HK, Shin TH, Phukan G, Tran TT, Lee G, Hwang WR, Kim JM. 2016 Microfluidic assessment of mechanical cell damage by extensional stress. *Lab Chip*. 16 96-103.

[15] Ning L, Chen X. 2017 A brief review of extrusion-based tissue scaffold bio-printing. *Biotechnol J*. 12 1600671.

[16] Down LA, Papavassiliou DV, Edgar A. 2011 Significance of extensional stresses to red blood cell lysis in a shearing flow. *Ann Biomed Eng*. 39 1632-42.

[17] Aguado BA, Mulyasasmita W, Su J, Lampe KJ, Heilshorn SC. 2011 Improving viability of stem cells during syringe needle flow through the design of hydrogel cell carriers. *Tissue Eng A*. 18 806-15.

[18] Ning L, Guillemot A, Zhao J, Kipouros G, Chen D. 2016 Influence of flow behavior of alginate-cell suspensions on cell viability and proliferation. *Tissue Eng C Methods* 22 652-62.

[19] Paul R, Apel J, Klaus S, Schügner F, Schwindke P, Reul H. 2003 Shear stress related blood damage in laminar couette flow. *Artif Organs.* 27 517-29.

[20] Nair K, Gandhi M, Khalil S, Yan KC, Marcolongo M, Barbee K, Sun W. 2009 Characterization of cell viability during bioprinting processes. *Biotech J*. 4 1168-77.

[21] Chen X, Li M, Ke H. 2008 Modeling of the flow rate in the dispensing-based process for fabricating tissue scaffolds. *J Manuf Sci Eng*. 130 021003.

[22] Lee SS, Yim Y, Ahn KH, Lee SJ. 2009 Extensional flow-based assessment of red blood cell deformability using hyperbolic converging microchannel. *Biomed Microdevices*. 11 1021-27.

[23] Boger D. 1987 Viscoelastic flows through contractions. *Annu Rev Fluid Mech*. 19 157-82.

[24] Meissner J, Hostettler J. 1994 A new elongational rheometer for polymer melts and other highly viscoelastic liquids. *Rheol Acta*. 33 1-21.

[25] Yang J, Dai Y, Li J. 2014 A different extensional viscosity prediction based on entry pressure drop. *J Appl Polym Sci*. 131 40536.
[26] Liang J, Yang J, Tang C. 2011 Melt shear viscosity of PP/Al (OH) 3/Mg (OH) 2 flame retardant composites at high extrusion rates. *J Appl Polym Sci*. 119 1835-41.
[27] Cogswell F. 1972 Measuring the extensional rheology of polymer melts. *Trans. Soc. Rheol*. 16 383-403.
[28] Rajagopalan D. 2000 Computational analysis of techniques to determine extensional viscosity from entrance flows. *Rheol Acta*. 39 138-51.
[29] Hatzikiriakos SG, Dealy JM. 1992 Wall slip of molten high density polyethylenes. II. Capillary rheometer studies. *J Rheol*. 36 703-41.
[30] Aho J, Syrjala S. 2006 Determination of the entrance pressure drop in capillary rheometry using Bagley correction and zero-length capillary. *Annual transactions of the Nordic Rheology Society*. 14 143-48.
[31] Ferziger, H, Milovan P. 2012 Computational methods for fluid dynamics. *Springer Science and Business Media*.
[32] Rage R, Mitchen J, Wilding G. 1990 DNA fluorometric assay in 96-well tissue culture plates using Hoechst 33258 after cell lysis by freezing in distilled water. *Anal Biochem*. 191 31-34.
[33] Tian X, Li M, Cao N, Li J, Chen X. 2009 Characterization of the flow behavior of alginate/hydroxyapatite mixtures for tissue scaffold fabrication. *Biofabrication*. 1 045005.
[34] Augst AD, Kong HJ, Mooney DJ. 2006 Alginate hydrogels as biomaterials. *Macromol Biosci*. 6 623-33.
[35] Rowley JA, Madlambayan G, Mooney DJ. 1999 Alginate hydrogels as synthetic extracellular matrix materials. *Biomaterials*. 20 45-53.
[36] Ning L, Xu Y, Chen X, Schreyer DJ. 2016 Influence of mechanical properties of alginate-based substrates on the performance of Schwann cells in culture. *J Biomater Sci Polym Ed*. 27 898-915.
[37] Drury JL, Mooney DJ. 2003 Hydrogels for tissue engineering: scaffold design variables and applications. *Biomaterials*. 24 4337-51.
[38] Draget KI, Skjåk-Bræk G, Smidsrød O. 1997 Alginate based new materials. *Int J Biol Macromol*. 21 47-55.

[39] Strober W. 2001 Trypan blue exclusion test of cell viability. *Curr Protoc Immunol*. A3-B.

[40] Hall P, Woods A. 1990 Immunohistochemical markers of cellular proliferation: achievements, problems and prospects. *Cell Prolif*. 23 505-22.

[41] Levental I, Georges PC, Janmey PA. 2007 Soft biological materials and their impact on cell function. *Soft Matter*. 3 299-306.

[42] Janmey PA, McCulloch CA. 2007 Cell mechanics: integrating cell responses to mechanical stimuli. *Annu Rev Biomed Eng*. 9 1-34.

[43] Gu Y, JY, Zhao Y, Liu Y, Ding F, Gu X, Yang Y. 2012 The influence of substrate stiffness on the behavior and functions of Schwann cells in culture. *Biomaterials*. 33 6672-81.

[44] Close R. 1972 Dynamic properties of mammalian skeletal muscles. *Physiol Rev*. 52 129-97.

[45] Li M, Tian X, Schreyer DJ, Chen X. 2011 Effect of needle geometry on flow rate and cell damage in the dispensing-based biofabrication process. *Biotechnol Prog*. 27 1777-84.

[46] Billiet T, Gevaert E, De Schryver T, Cornelissen M, Dubruel P. 2014 The 3D printing of gelatin methacrylamide cell-laden tissue-engineered constructs with high cell viability. *Biomaterials*. 35 49-62.

CHAPTER 6

3D Bioprinting of Scaffolds Containing Living Schwann Cells for Potential Nerve Tissue Engineering Applications

This chapter has been submitted as " Liqun Ning, Haoying Sun, Tiphanie Lelong, Romain Guilloteau, Ning Zhu, David J. Schreyer, and Xiongbiao Chen, 3D Bioprinting of Scaffolds Containing Living Schwann Cells for Potential Nerve Tissue Engineering Applications. *Biofabrication*". It is under reviewing. According to the Copyright Agreement, "the authors retain the right to include the journal article, in full or in part, in a thesis or dissertation".

6.1 Abstract

3D bioprinting shows great potential for producing tissue-like constructs with encapsulated cells to support the regeneration of tissues after injury or disease. Preparing tailored biomaterials to maintain the viability and functions of cells is challenging. Moreover, producing such constructs with sufficient structural support and functions that promote the reorganization of encapsulated cells so as to mimic natural tissues requires even more effort. This chapter presents a comprehensive research of 3D bioprinting of scaffolds with encapsulated Schwann cells using composite hydrogels based on varying concentrations of alginate, fibrin, hyaluronic acid, and RGD peptide. In hydrogel investigation, the composited hydrogel microstructures and mechanical stiffness after gelation were examined and, based on the morphological spreading of cells, suitable hydrogel combinations by adjusting the concentration of fibrin were identified and prepared. During the bioprinting process, the flow behavior of hydrogel solutions and bioprinting process parameters (e.g., dispensing pressure, dispensing head speed, crosslinking process) which determine the structure of the printed scaffolds were evaluated and regulated, and based on the results, scaffolds with fully interconnected channels were produced. Schwann cell performance in the scaffold was investigated in terms of viability, proliferation, orientation, and the ability to produce laminin, an extracellular matrix protein thought to be beneficial in guiding nerve regeneration. The developed bioprinting processes promote the alignment of Schwann cells inside scaffolds, and maintains high cell

viability and other cellular functions, demonstrating its great potential for applications in the field of nerve tissue engineering.

Key words: 3D bioprinting, hydrogel, scaffold, cell function, cell alignment

6.2 Introduction

A major objective of tissue engineering is to create bioengineered tissue substitutes with properties that promote the regeneration of tissues rendered dysfunctional by disease or damage [1]. For example, to promote the repair of peripheral nervous system (PNS) injuries caused by crushing or transection of axons, bioengineered tissue substitutes act as bridges to link separated nerve segments and stimulate axon growth and reconnection [2]. Bioengineered scaffolds are 3D porous tissue substitutes made from biomaterials and living cells. They are designed to support and guide the regeneration of targeted tissues by facilitating cell differentiation, migration, and proliferation [3, 4]. To fabricate such scaffolds, a major challenge is successfully orchestrating the formation of structures with expected tissue functions by using suitable biomaterials and cells. From this challenge, the first key consideration is preparing biomaterials with tailored biological and chemical properties that can maintain the viability and facilitate the functions of incorporated cells and, subsequently, facilitate the migration and organization of host cells after implantation. The second key consideration is the fabricating techniques that manipulate the biomaterials and cells so as to produce bioengineered constructs with high structural fidelity and sufficient mechanical properties that can offer necessary cues to support cell organization and ECM deposition [5, 6].

The preparation of biomaterial is crucial in scaffold fabrication because it provides the fundamental support and necessary structural interface for interactions with cells and tissues [7]. In biomaterial preparation, biocompatibility, which refers to the characteristic of passively allowing or actively producing positive effects on cells and tissues, should be considered at the outset [8]. Hydrogels are one of the most extensively used biomaterial types in scaffold fabrication due to their inherent ability to provide an aqueous environment for cells [9]. High water content retention makes hydrogels compatible with cell delivery and encapsulation [10-13]. Despite these advantages, the use of individual hydrogel for scaffold fabrication is challenging because it either faces the problem of providing cell-

binding domains to facilitate the attachment of incorporated cells, or suffers from poor manipulative ability during the scaffold fabricating process.

Therefore, tailored hydrogels that contain adequate cell-binding domains for cell attachment while can be manipulated into a desired architecture are demanded [14, 15]. The feasibility of fabricating scaffolds from hydrogels is also heavily dependent on the fabrication technique [7]. The 3D bioprinting technique has been generating great interest in hydrogel-based scaffold fabrication. With recent advances in bioprinting, living cells incorporated within the hydrogel can be deposited in a layer-by-layer pattern to form spatially controlled porous structures [16, 17]. In this process, a hydrogel solution containing cells is loaded into a syringe of the bioprinter, forced to flow through a connected needle, and deposited to a predefined location by controlling the printing force (e.g., dispensing pressure) and speed of the printing head (or dispensing head). Feasibility of using a hydrogel in 3D bioprinting is also known as bioprintability; a hydrogel with good bioprintability is identified to have a flow behavior and viscosity that ensure regular deposition, and an appropriate crosslinking mechanism to generate a structure with sufficient mechanical strength to avoid structural failure [18]. Preparing biocompatible and bioprintable hydrogels in 3D scaffold bioprinting is important and challenging. Moreover, using prepared hydrogels to produce a scaffold that can reorganize encapsulated cells to mimic natural tissues is also a demanding task.

Alginate is a natural hydrogel that has been extensively used in scaffold bioprinting due to the availability of a simple calcium-based crosslinking mechanism and its ability to maintain cell viability [19]. However, its utilization is limited due to its poor cell adhesion support. High concentration of alginate increases the viscosity, which can relieve the challenge in the scaffold bioprinting process, however, it also reduces proliferation and other measures of cell performance [13, 20]. The situation can be improved if RGD (Arg-Gly-Asp) peptide, a special protein sequence recognized by specific cell-adhesion molecules, is used to modify low concentration alginate hydrogels [19]. Hyaluronic acid (HA) is another compatible hydrogel to cell viability and has been used in bioprinting to regulate the viscosity of the printed solution [21], although it lacks adhesion sites for cell attachment. Fibrin is a protein hydrogel that can be obtained via proteolysis of fibrinogen with thrombin, the key proteins involved in blood clotting [22, 23]. When factor XIII,

another plasma protein involved in blood clotting is contained, the covalent crosslinks between fibrin fibers can be introduced, resulting in improved gel stability [24]. Unlike alginate and HA, fibrin hydrogels contain adequate cell-binding sites to promote cell attachment and therefore other cellular functions [25]. However, bioprinting fibrinogen independently is challenging due to its poor inability to form fibrin scaffolds with sufficient mechanical stability. Hence, although the three hydrogels mentioned above have limitations, using them together may capitalize on the benefits of each.

In the PNS, Schwann cells are the major glial cells which promote axonal regeneration by producing a favorable growth pathway, and eventually forming myelin around axons [5, 13]. Therefore, the utilization of scaffolds with organized Schwann cells has great potential to facilitate the reconnection of axons in PNS injuries. This chapter presents a comprehensive study on 3D bioprinting scaffolds using cell-biomaterial suspensions comprised of alginate, HA, fibrin, RGD peptide, and Schwann cells. In this studied, two parts which include hydrogel investigation and bioprinting process development were majorly investigated. For hydrogel preparation, the influence of initial fibrinogen concentrations on the properties of the hydrogel formed, including the microstructures and mechanical stiffness was examined and a suitable concentration determined experimentally in terms of the ability to support Schwann cell spreading. In scaffold bioprinting, the flow behavior and viscosity of the tailored hydrogel solution were evaluated and, on this basis, bioprinting parameters including the dispensing pressure, speed of the dispensing head, and concentration of crosslinkers were determined experimentally so as to obtain scaffolds with desired outer shape and inner structure. Multiple cellular analyses, including cell viability, proliferation, morphology, orientation, and protein expression, were then conducted over a period of 10 days in culture for the scaffolds containing the encapsulated Schwann cells. The results demonstrate the ability of our bioprinting process developed to produce scaffolds that have great potential for nerve tissue regeneration.

6.3 Materials and methods

6.3.1 Materials

Low-viscosity sodium alginate (MW 12000-80000 Da) and hyaluronic acid were obtained from Sigma-Aldrich, Canada. Fibrinogen and thrombin TISSEEL VHSD kits were purchased from Baxter, Canada. Calcium chloride ($CaCl_2$), sodium chloride (NaCl), sodium hydroxide (NaOH), PEI (polyethyleneimine), MTT [3-(4,5-dimethylthiazol-2-yl)-2,5-diphenyltetrazolium bromide], BSA (bovine serum albumin), DMSO, Tween 20, EDC [N-(3-dimethylaminopropyl)-N'-ethylcarbodiimide hydrochloride], NHS (N-hydroxysuccinimide), MES, DAPI fluorescent dye, aprotinin (from bovine lung), EACA (6-aminocaproic acid), and 100× penicillin-streptomycin (PS) were purchased from Sigma-Aldrich, Canada. Hoechst 33342, RGD peptide (GGGGRGDS), calcein-AM, and propidium iodide (PI) were purchased from AnaSpec, USA. Primary S100 antibody (EP1576Y) was purchased from Abcam, USA.

6.3.2 Bulk hydrogel preparation

Sodium alginate powder was first dissolved in deionized water to form a 0.2% w/v solution. A 0.22-μm bottle-top filter (Thermo Scientific) was then used to sterilize the prepared alginate solution. The filtered solution was removed to a -40 °C freezer for 24 h and later freeze-dried using a freeze-dryer (FreeZone, Labconco) under sterile conditions for 72 h. The alginate powder obtained was combined with sterilized HA powder and dissolved in 0.9% NaCl to achieve a final 2% w/v alginate plus 1% w/v HA solution.

Alginate was also covalently bonded with RGD peptide as described in a previous study [26]. Briefly, 305 mM EDC, 115 mM NHS, and 300 mM NaCl were dissolved in 100 mM MES buffer, with 10 N NaOH added dropwise to the solution to adjust the pH to near 6.5. Sterilized alginate solution and RGD solution (RGD to alginate ratio 1:250, w/w) were mixed in a centrifuge tube that was then rotated over 48 h for complete reaction at room temperature. The reacted solution was dialyzed for 3 d at 4 °C to remove all unreacted reagents, and the dialyzed solution was lyophilized and dissolved in 0.9% NaCl with HA powder to eventually form a 2% RGD modified alginate with 1% HA solution.

Fibrinogen (containing 1U/mL factor XIII [23]) and thrombin powder were prepared in sterile solution according to the manufacturer's instructions. Fibrinogen powder was dissolved in 500 μg/mL aprotinin solution at 37 °C to obtain a 90 mg/mL stock solution. Thrombin was dissolved in 0.9% NaCl and 40 μM $CaCl_2$ solution to obtain a 500 U/mL stock solution. Six independent hydrogel solution groups were prepared using the stock hydrogel solutions: (1) 1% alginate + 0.5% HA (hereafter AH); (2) RGD modified 1% alginate + 0.5% HA (hereafter RAH); (3) 1% alginate + 0.5% HA + 10 mg/mL fibrinogen (hereafter 10FAH); (4) 1% alginate + 0.5% HA + 20 mg/mL fibrinogen (hereafter 20FAH); (5) 1% alginate + 0.5% HA + 40 mg/mL fibrinogen (hereafter 40FAH); and (6) 1% RGD modified alginate + 0.5% HA + 40 mg/mL fibrinogen (hereafter FRAH). A 40-uL aliquot from each group was then transferred onto a PEI-coated (0.5% w/v PEI dissolved in deionized water, filtered sterilized) round glass slide to cover the slide surface, and crosslinked for 10 min with 100 mM $CaCl_2$ solution (for AH only) or 100 mM $CaCl_2$ + 25 U/mL thrombin (for groups including fibrinogen) for gelation.

6.3.3 Characterization of bulk hydrogels

The composition of each of the six hydrogel preparations (plus a fibrin-only gel) was assessed using Fourier transform infrared spectroscopy (IlluminatIR II FTIR microscope accessory, Smith's Detection) equipped with an attenuated total reflectance (ATR) objective. Spectra were obtained from 4500 to 550 cm^{-1} at a resolution of 2 cm^{-1}. Hydrogels of each group were lyophilized before scanning.

The microstructure of each crosslinked hydrogel was also evaluated. Lyophilized samples of each of the hydrogels were sputter-coated with a thin layer of gold and analyzed by scanning electron microscopy (SEM; SU8010, Hitachi). Representative images of each sample were recorded at magnifications of 400 x and 2000 x.

A plane strain compression test, also known as a Watts-Ford test, was performed on all prepared hydrogel groups except RAH and FRAH. Since these two composited hydrogels included only a small amount of RGD peptide compared to AH and 40FAH, respectively, we assumed that inclusion of RGD peptide would not significantly alter the physical properties. Figure 6.1 is a schematic of the mechanical test procedure. A 200-μL of hydrogel solution from each group was first loaded into a cuboid mold, and crosslinked

from above by spraying an atomized calcium medium (100 mM) for 5 min. After the hydrogel was pre-gelled in the mold, liquid crosslinkers were then carefully pipetted into the mold for extended crosslinking overnight at room temperature. The obtained hydrogel was demolded and transferred into a well containing crosslinking solution for another 24 h for complete gelation. The result was a hydrogel sheet 9 mm × 17 mm × 1.2 mm in size, which was then flattened between two parallel anvils of a compressive testing instrument (Texture Technologies Corp.). During the compressive test, the lower anvil (with a width of a) remained fixed, while the upper anvil was lowered at a preset speed v of 0.01 mm/s. The loading force F and the associated displacement D of the upper anvil were automatically measured during the compression, and later used to calculate the equivalent compressive stress σ and strain ε using equations for classical plastic deformation in a plane strain compression test [27]:

$$\sigma = \frac{\sqrt{3}}{2}\frac{F}{aL}, \tag{6.1}$$

$$\varepsilon = \frac{2}{\sqrt{3}}\ln\left(\frac{h_0+2D}{h_0}\right). \tag{6.2}$$

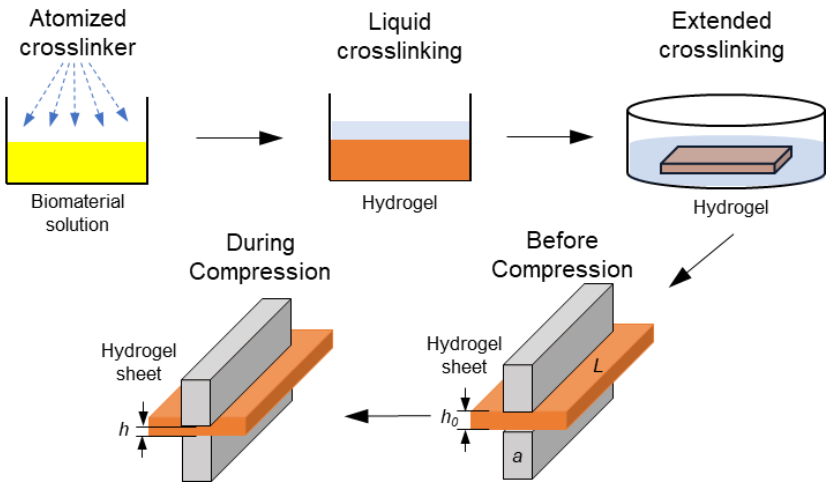

Figure 6. 1 Schematic of process to test the mechanical stiffness of hydrogels.

6.3.4 Schwann cell culture and preliminary evaluation of morphology

Schwann cells were isolated from the sciatic nerve of Sprague-Dawley rats using a previously described D-valine selection method [28]. Briefly, the sciatic nerve was isolated, stripped of the epineurium, teased, and cut into 2-mm fragments. The fragments were digested in collagenase for 1 h at 37 °C, then strained to remove debris. Cells were cultured

in Dulbecco's Modified Eagle's Medium (DMEM, Sigma) with D-valine (Sigma-Aldrich, Canada) and 10% fetal bovine serum (FBS, Sigma) in a humidified incubator at 37 °C with 5% CO_2, and their purity assessed with immunofluorescence staining for Schwann cell marker protein S100 and DAPI [23]. Cultures from passages 4 through 12 were used for experiments. All live animal procedures were performed after approval by the University (of Saskatchewan) Committee on Animal Care and Supply.

Hydrogel solution from each group was gently mixed with Schwann cells (1×10^6 cells/mL) to obtain uniformly blended cell-biomaterial suspensions. Forty-uL aliquots of this cell suspension were then transferred onto round glass slides for 10 min crosslinking. The cell-encapsulating hydrogels obtained were rinsed twice with TBS (Tris buffered saline), and then cultured in a 24-well plate using DMEM culture medium containing 10% FBS, 10 mM $CaCl_2$, and 1% penicillin-streptomycin. After 4 d, calcein-AM solution with a final concentration of 1 μg/mL was added to each well for 30 min, and the stained hydrogel was observed under a fluorescence microscope (Carl Zeiss Axiovert 100). Three hydrogels were prepared for each group and three random images taken for each hydrogel sample. Cell circularity was analyzed using ImageJ software (National Institutes of Health, USA). Fibrin hydrogels with cells were also prepared and used as a positive control group.

6.3.5 Bioprinting parameter analysis and 3D scaffold bioprinting

6.3.5.1 Characterization of flow behavior

The process of 3D bioprinting scaffolds using 40FAH and FRAH hydrogel solutions with or without the inclusion of Schwann cells was studied (Figure 6.2). For Schwan cell scaffold bioprinting, cells were carefully added to the hydrogel solutions in a sterilized environment to obtain final biomaterial suspensions containing 1×10^6 cells/mL. The uniformly mixed suspensions were then loaded into the autoclaved syringe of the bioprinter (3D Bio-plotter, EnvisionTEC.), extruded through a 200-μm autoclaved needle, and deposited into a container containing calcium/thrombin solution to stabilize the printed hydrogel into a scaffold structure at room temperature (~22 °C).

The flow behavior of 40FAH solution was characterized on a rheometer with a parallel geometry (AR G2 rheometer, TA Instruments). A 150-μL aliquot of the hydrogel solution was loaded between the upper and lower plates. The upper plate was preset to

rotate at a series of speeds with the lower plate remaining immobile. Shear stress on the suspension under each rotating speed was recorded during the shearing, with the temperature set at either 4 or 22 °C. Also, the viscosity of 40FAH under these two given temperatures was recorded (2% alginate with 1% HA solution was also tested as a control group under 22 °C). The test was repeated three times and the average shear stress value was calculated.

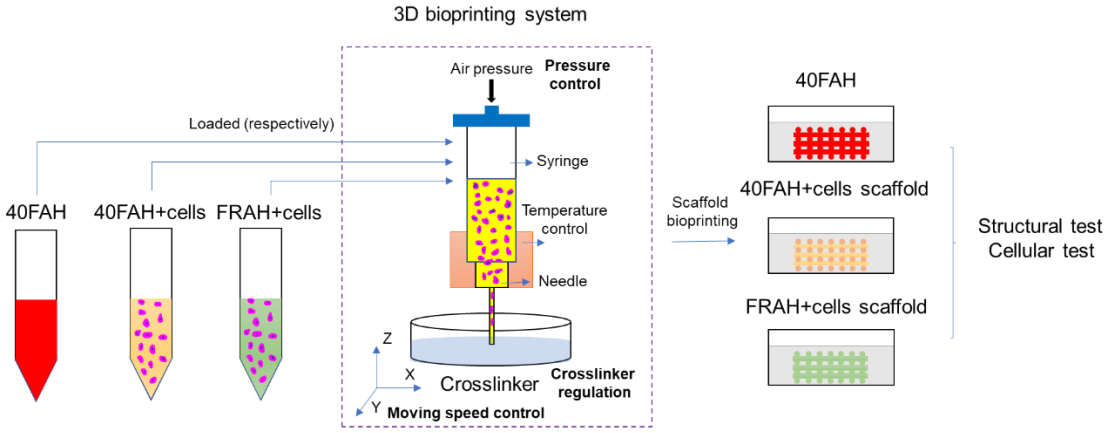

Figure 6. 2 Schematic of process for both cell-incorporated and non-cell scaffold bioprinting

6.3.5.2 Evaluation of the mass flow rate

The mass flow rate of the hydrogel solution was evaluated before scaffold bioprinting. 40FAH solution loaded into the syringe was extruded under a series of bioprinting pressures (20, 30, 40, 50, and 60 KPa) over a defined time period, with the solution droplet deposited on a weighting paper later transferred to a digital scale. The average mass obtained from three droplets was recorded and used to calculate the mass flow rate.

6.3.5.3 Regulation of calcium concentration and speed of the dispensing head

Crosslinking solutions containing 10 U/mL thrombin and a series of calcium concentrations from 10 to 60 mM were prepared. Then, 1 mL of crosslinking solution was pipetted into the wells of a 12-well plate that had been coated with 0.5% PEI at 37 °C for 24 h. 40FAH was extruded into these wells at a pressure of 30 KPa and a dispensing head speed of 6 mm/s to build three-layer scaffolds, with the strand angle of each layer set at 90°

relative to the printing stage. For each crosslinking solution, the hydrogel material was printed five times into separate wells. If at least three scaffolds with stable layers and pores could be observed, the calcium concentration of the crosslinking solution was deemed appropriate for scaffold bioprinting.

The influence of the speed of the dispensing head on scaffold bioprinting was also investigated by varying the speed from 1 to 11 mm/s. The other bioprinting parameters were held constant, including bioprinting pressure at 30 KPa and the concentration of $CaCl_2$ in crosslinking solution at 20 mM. Again, five scaffolds were printed at each speed. If at least three integrated scaffolds could be built, the speed was considered appropriate for scaffold bioprinting.

6.3.5.4 Influence of dispensing head speed on strand diameter

To determine the influence of dispensing head speed on strand diameter, the dispensing head speed was set at 4, 6, and 10 mm/s and the applied pressure held at 30 KPa. 40FAH was extruded and deposited into wells of a 12-well plate containing 1 mL 20 mM calcium and 10 U/mL thrombin to build one-layer scaffolds. After 3 min pre-gelation, the crosslinking solution was replaced by a new medium that contained 100 mM calcium and 25 U/mL thrombin for another 15 min to complete the crosslinking of the printed scaffolds. Five images of the printed strands for each dispensing head speed were then captured using an optical microscope (Carl Zeiss Axiovert 100) and the strands widths were measured.

6.3.5.5 Influence of dispensing head speed on the orientation of fibrin fibers inside the printed strand

One-layer scaffolds made from the alginate, fibrin, and HA mixtures were created as described above, except that bioprinting speeds of 2, 6, and 9 mm/s were applied and the fibrinogen concentration reduced to 10 mg/mL (equivalent to 10FAH). Droplets were also produced and crosslinked as a negative control group. After complete gelation, scaffolds and droplets were fixed in -20 °C methanol for 1 h, rinsed with TBS containing 10 mM $CaCl_2$, then blocked with 1% BSA, 3% horse serum, 10 mM calcium, and 0.1% Tween 20 in TBS for 2 h. Goat anti-fibrinogen (1:1000, Sigma Aldrich) in blocking solution was then added to each well for 3 h at room temperature. Printed hydrogels were

washed three times in TBS containing 10 mM calcium and 0.05% Tween 20 (first time, 1 h at room temperature; second time, overnight at 4 °C; third time 1 h at room temperature). Hydrogels were then incubated with Alexa Fluor 488 mouse anti-goat antibody (1:1000, Thermo Fisher Scientific) in blocking solution for 3 h at room temperature, and washed a second time following the same procedure. Each scaffold coverslip was mounted on a glass slide using ProLong Gold antifade mountant (Thermo Fisher Scientific).

Images of stained scaffolds were captured using a fluorescence microspore (Axio Imager M1, Zeiss) with a 40× oil immersion objective lens. The orientations of fibrin fibers inside the scaffold strand and the droplet were measured using the orientation distribution function of ImageJ.

6.3.5.6 3D scaffold bioprinting

Predesigned, multilayer 3D scaffolds with dimensions of 8 mm × 8 mm × 2 mm were printed using 40FAH. The strand angle of each layer was set at 90° relative to the printing stage. Spacing between the centers of adjacent strands was preset at 1 mm. Each biomaterial solution was printed into a crosslinking solution containing 20 mM $CaCl_2$ and 10 U/mL thrombin at a dispensing head speed of 9 mm/s and dispensing pressure of 30 KPa. After 3 min pre-crosslinking, the crosslinking solution was replaced by 100 mM calcium and 25 U/mL thrombin for another 15 min to complete gelation.

6.3.5.7 Evaluation of 3D printed scaffolds morphology

Both the external shape and internal porous structure of printed scaffolds were imaged at 05ID-2 beamline at the Biomedical Imaging and Therapy facility (BMIT) at the Canadian Light Source (CLS), with the technique of synchrotron-based X-ray inline phase contrast imaging-computed tomography (SR-inline-PCI-CT). In this process, the printed scaffold was held in a special plastic holder and placed on a rotating scanning stage. The data were collected at a photon energy of 30 keV by means of a beam monitor AA-60 (Hamamatsu) combined with a digital camera (Hamamatsu C9300-124), with an effective pixel size of 8.6 μm. 3000 projections were captured in 180 degree CT scan with the exposure time of 20 ms per projection. Phase retrieval and reconstructed were done by PITRE 3.1. The 3D model of the construct was built by Avizo 9.1 (FEI Company).

6.3.6 Evaluation of Schwann cells encapsulated in printed scaffolds

6.3.6.1 Evaluation of cell viability

40FAH and FRAH hydrogels mixed with Schwann cells were used for scaffold bioprinting following the printing procedure described above. After printing, solidified scaffolds were rinsed twice with DMEM solution, and then submerged in culture medium (DMEM with 10% FBS, 5 ug/mL EACA, 10 mM $CaCl_2$, 50 ug/mL aprotinin, and 1% antibiotics) in a 37 °C incubator containing 5% CO_2. A live/dead assay was used to assess cell viability. Fluorescent dyes calcein-AM and PI, which selectively stain live or dead cells, were applied to the scaffold at final concentrations of 1 and 25 μg/mL, respectively. After a 30-min incubation, cell viability was assessed by manually counting stained cells on images randomly taken from scaffolds observed with a fluorescence microscope (Carl Zeiss Axiovert 100). Cell viability for both 40FAH and FRAH scaffolds was measured on day 1, 4, and 10; five images for each group were obtained and analyzed using ImageJ, with viability calculated as percent live cells among the total number of cells.

6.3.6.2 Evaluation of cell proliferation

An MTT assay was performed to analyze cell number and thus the proliferation of cells. Before the evaluation, the standard relation between Schwann cell number and MTT absorbance was identified. Briefly, Schwann cells (cell number of 2×10^3, 4×10^3, 8×10^3, 2×10^4, 4×10^4, 8×10^4, 1.2×10^5, and 2×10^5) were either laid over the surface of wells of a 12-well plate, or uniformly mixed with AH solution that was then loaded into another 12-well plate. After gelation, both seeded cells and encapsulated cells were cultured for 12 h in an incubator in 1 mL of DMEM solution containing 10% FBS. A 100-μL aliquot of MTT solution (5 mg/mL) was then added to each cell well for another 2 h (for seeded cells) or 5 h (for encapsulated cells) of incubation. After removing the medium, DMSO solution (1 mL) was added to the wells with seeded cells to dissolve the formazan precipitate produced. For encapsulated cells, the hydrogel was first frozen at -40 °C for 24 h and then freeze-dried for another 24 h. Upon completion of dehydration, 1 mL DMSO was added for 24 h at room temperature to dissolve the formazan precipitate. Absorbance of dissolved

formazan was measured at 555/650 nm using a microplate reader (SpectraMax 250, Molecular Devices).

The proliferation of Schwann cells encapsulated in scaffolds was examined following the same processing method described above on day 1, 4, and 10, with the absorbance value obtained for day 1 normalized to 100%.

Cell number was also assessed using a fluorescent staining method. Cells encapsulated in scaffolds were first stained with Hoechst 33342 (1 μg/mL) and incubated for 30 min at 37 °C. Scaffolds were then observed under a fluorescence microscope (Carl Zeiss Axiovert 100), images of scaffold strands were captured randomly. Cell number was assessed by manually counting stained cells on five images taken from each of three scaffolds prepared from each hydrogel solution. The average cell number in one single strand counted on day 1 was normalized to 100%.

6.3.6.3 Evaluation of cell alignment and circularity within scaffolds

The spreading and growth orientation of Schwann cells encapsulated in 40FAH and FRAH scaffolds printed in a two-layer pattern were analyzed on day 4 and 10 using S100 immunocytochemistry. Printed scaffolds were fixed, rinsed, and blocked as in Section 2.5.5. Rabbit anti-S100 (1:200; Abcam) in blocking solution was then used to stain cells for 3 h. Scaffolds were washed three times and then labeled with Alexa Fluor 488 goat anti-rabbit antibody (1:500) and DAPI (1:1000) for another 3 h. After washing, scaffolds were mounted and observed in a confocal fluorescence microspore (Leica SP5). The long axis alignment and circularity of S100 stained Schwann cells were measured from images obtained from the examined scaffolds with the assistance of ImageJ. Three images were analyzed for each scaffold.

6.3.6.4 Evaluation of extracellular matrix protein expression in scaffolds

Immunocytochemistry was also employed to investigate Schwann cell phenotype with respect to laminin protein expression at day 4 and 10. The staining procedure was the same as for S100 staining, except that the primary antibody used was rabbit anti-laminin (1:200, Sigma) and the secondary antibody was Alexa Fluor 555 goat anti-rabbit (1:500).

Images were observed using confocal fluorescence microscopy, and the fluorescence intensity associated with Schwann cells was measured using ImageJ.

6.3.7 Statistical analysis

Mean values and standard deviation (SD) values were calculated for all quantitative measures. The statistical significance of experimental data was calculated using one-way analysis of variance (ANOVA). Pairwise comparisons were performed using Tukey's test using Graphpad Prism (GraphPad Software) with an acceptable significance level of $p < 0.05$.

6.4 Results

6.4.1 Characterization of hydrogel properties

The composition of each hydrogel group after gelation was investigated using IR spectroscopy. Figure 6.3A shows that hydrogels prepared using a combination of alginate and HA demonstrate spectral characteristics related to carboxylate anions: an antisymmetric stretch at 1597 cm^{-1} and a symmetric stretch at 1417 cm^{-1}. These band positions are in agreement with those previously reported without significant shifts (i.e., less than 5 cm^{-1}) [29], indicating that both alginate and HA remain intact in the hydrogels formed. Figure 6.3B shows that the inclusion of RGD peptide results in an additional absorption peak at 1650 cm^{-1}, which represents amine groups of the RGD peptide, suggesting that the RGD successfully bonded to the alginate [30]. Fibrin spectral characteristics in Figure 6.3C show absorption bands at 1535 and 1238 cm^{-1}, which represent amide groups II and III [31]. These two peaks are absent in the AH hydrogel spectra but appear in the 40FAH hydrogel spectra, confirming the inclusion of fibrin. Notably, the carbonyl peak of the AH hydrogel has merged and shifted from 1597 to 1642 cm^{-1}, which might indicate that carboxyl groups have reacted with protonated NH_2 groups on fibrin [19].

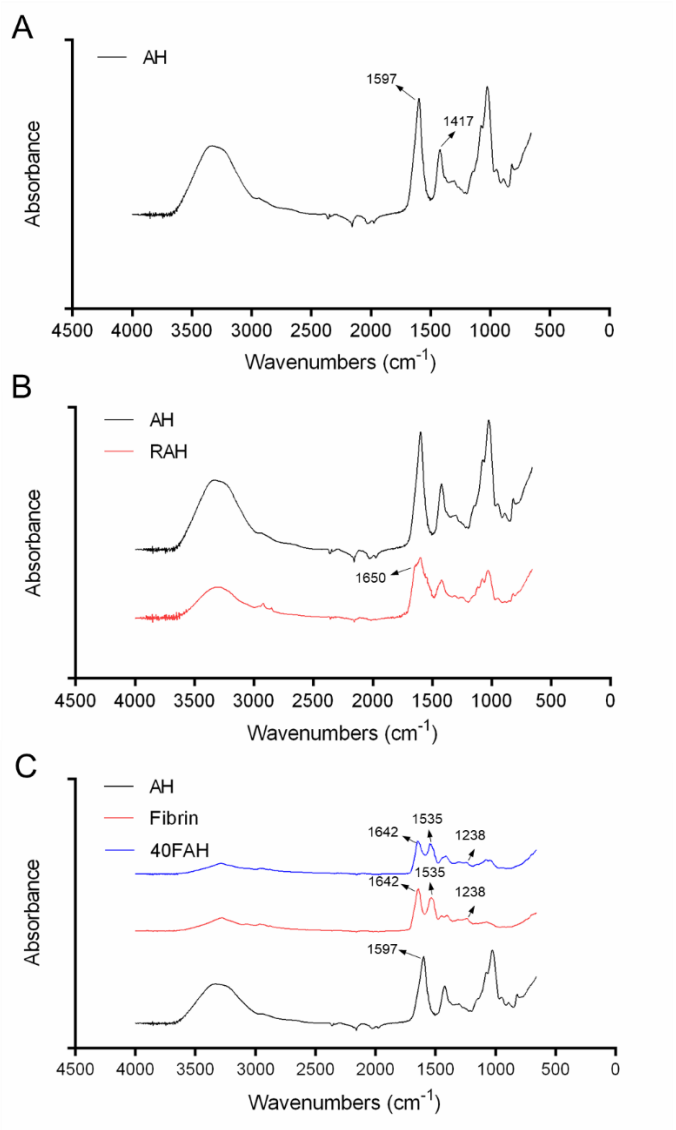

Figure 6. 3 FTIR spectra of hydrogels: A, AH; B, AH and RAH; and C, AH, fibrin, and 40FAH

The microstructures of each gelled biomaterial group were examined using SEM. Figure 6.4 shows no significant structural differences between AH and RAH at the microscale (Figures 6.4A, B). Images of AH and RAH feature similar sheet-like structures with limited pores. With the inclusion of fibrinogen (to form fibrin), microfibers appear along with the AH structures (Figures 6.4C-F); more microfibers can be identified at higher fibrinogen concentrations. In addition, more micropores appeared at fibrinogen concentrations of 40 mg/mL compared 10 or 20 mg/mL (Figures 6.4C-E). Morphological

differences between 40FAH and FRAH hydrogels are not significant; both share a similar microstructure that features high porosity and prominent fibers (Figures 6.4E, F).

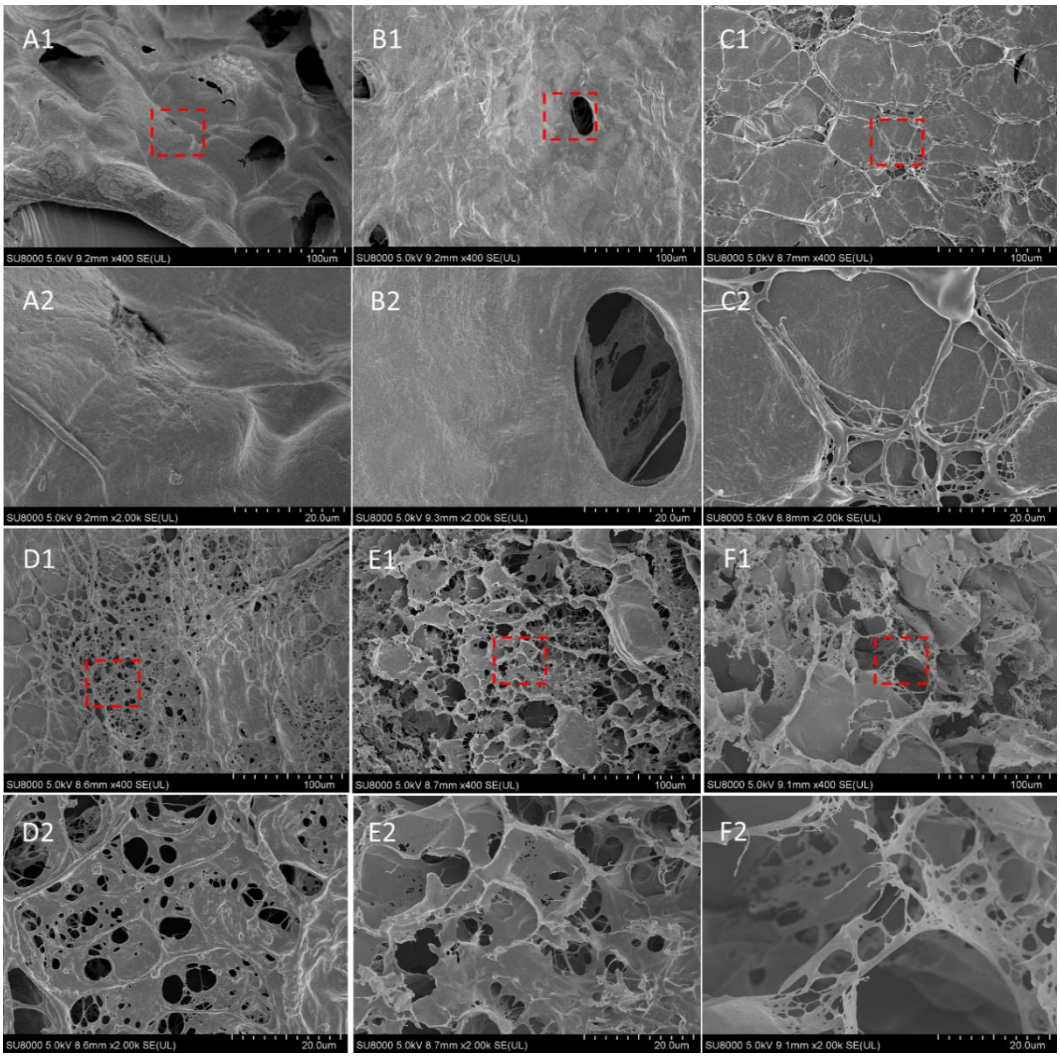

Figure 6. 4 SEM images of prepared hydrogels: A, AH; B, RAH; C, 10FAH; D, 20FAH; E, 40FAH; and F, FRAH.

Figure 6.5 shows the demolded hydrogel samples as well as their equivalent stress-strain states as the strain range extends up to 70-80%. The molded homogeneous hydrogels sheet shown in Figures 6.5A and 6.5B ensures the reliability of results from our compressive tests. The continuous increase of the equivalent stress-strain responses shown in Figures 6.5C and 6.5D demonstrates that the addition of fibrinogen to the hydrogel enhances stiffness: more formation of fibrin makes the hydrogels stiffer. Results from the first 30% of the strain curve in Figure 6.5D show that the effect of fibrin on the mechanical

properties of the 10FAH, 20FAH, and 40FAH hydrogels is not significant, as the responses within this strain range have close values.

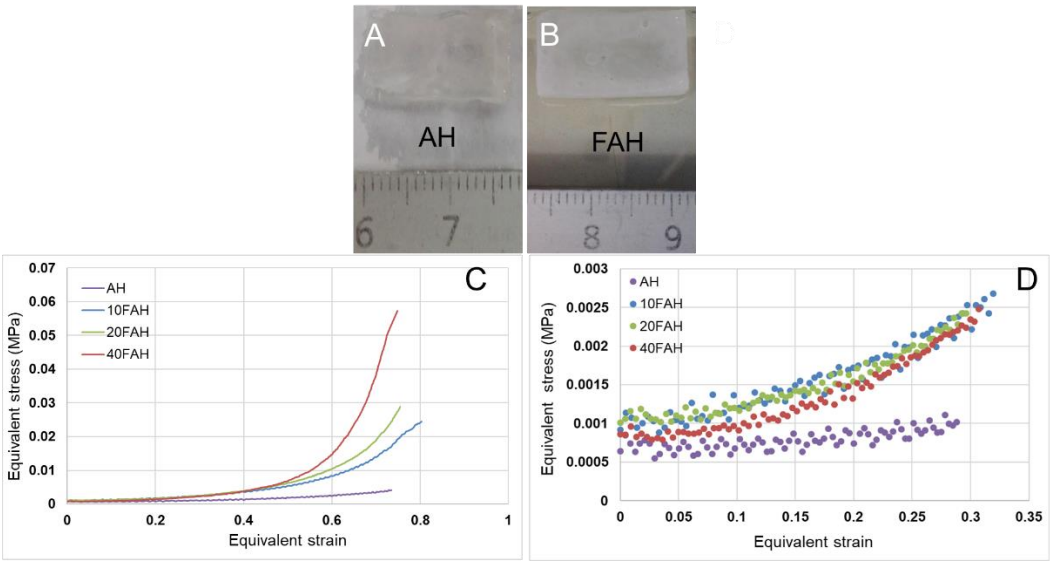

Figure 6. 5 Evaluation of mechanical stiffness of hydrogels: A and B, Demolded AH and FAH hydrogels; C, equivalent stress-strain responses as the strain range extends up to 70-80%; and D, equivalent stress-strain responses at a strain level of 30%.

Schwann cells encapsulated in each hydrogel were stained with calcium-AM for preliminary investigation of cellular morphology. Cell circularity was measured as an indicator of Schwann cell attachment to the hydrogel: failure of attachment is expected to result in spherical cell morphology. Figure 6.6 shows that Schwann cells cultured in pure fibrin hydrogel, which is expected to provide the best matrix attachment, have the lowest circularity at 0.521±0.070 (Figure 6.6G) while those in the AH hydrogel have the highest circularity at 0.905± 0.015 (Figure 6.6A), indicating that most cells in the AH hydrogel maintain their roundness and do not achieve an attachment-mediated spreading phenotype after 4 d of culture. The circularity of cells in the RAH hydrogel was lower at 0.854±0.022 (Figure 6.6B). Compared to the AH hydrogel, cell circularity values also decreased as fibrinogen was added. For example, the average circularity values of cells in the 10FAH, 20FAH, and 40FAH hydrogels were 0.885±0.025, 0.876±0.020, and 0.738±0.066, respectively (Figures 6.6C-E). Cellular circularity in the FRAH hydrogel had a smaller value of 0.658±0.014 after culture compared to the 40FAH hydrogel, which contained the same amount of fibrin (Figure 6.6F); this demonstrates that the spreading of Schwann cells

can be facilitated not only by regulating the fibrinogen concentration but also by adding RGD peptide to the alginate.

Based on this preliminary study, 40FAH and FRAH hydrogels were used as biomaterials for scaffold bioprinting in all subsequent experiments.

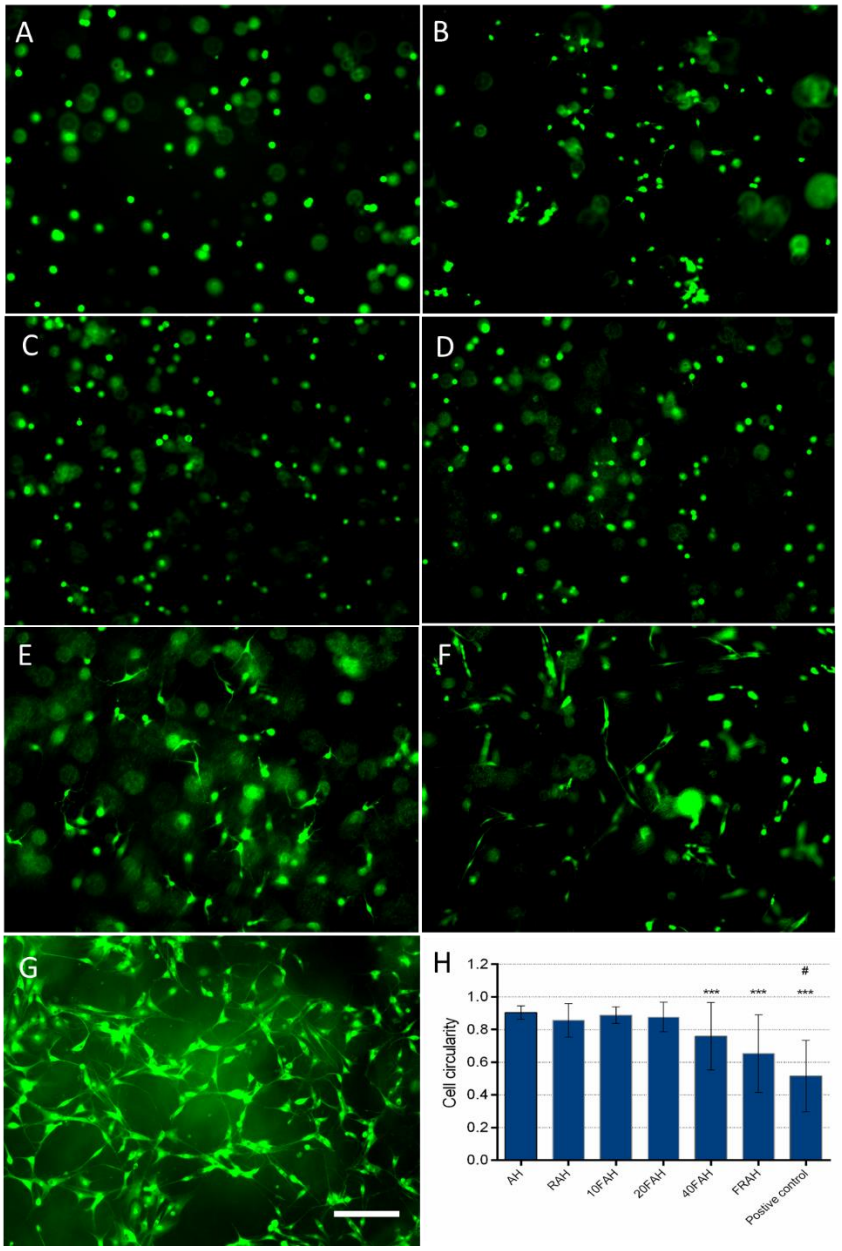

Figure 6. 6 Circularity assessment of Schwann cells encapsulated in diverse hydrogels: A, fibrin; B, AH; C, RAH; D, 10FAH; E, 20FAH; F, 40FAH; G, FRAH; and H, Statistical results of cellular circularity. Scale bar represents 200 μm; *** represents $p<0.001$

compared to the first four groups, # represents $p<0.05$ compared to the 40FAH and FRAH.

6.4.2 Evaluation of 3D scaffold bioprinting

The results of flow behavior analysis for the 40FAH solution at 4 and 22 °C are shown in Figures 6.7A, B. The hydrogel solution exhibits a non-Newtonian, shear thinning flow behavior because the resulting shear stress-shear rate curve has a nonlinear, concave pattern [32]. Figure 6.7A also verifies that the yield stress of the 40FAH solution at both temperatures approximately equals zero [33]. Therefore, a power law model without considering the yield stress can be used to represent the flow behavior of the hydrogel solution [34]. Figure 6.7C exhibits low viscosity values of 40FAH at both 4 °C (1.23-7.35 Pa·s) and 22 °C (0.56-4.36 Pa·s) in the tested range of shear rate. The viscosity of the control group (alginate and HA solution) at 22 °C shows a litter lower viscosity than the performance of 40FAH solution. Compared to previous study with alginate and HA solution, the 40FAH solution at 22 °C could be dispensed under controllable manner [20].

One important element for controlled production of a scaffold by bioprinting is the solution mass flow rate of the printed biomaterial, which can be regulated by changing the dispensing pressure. Figure 6.7D shows the mass flow rate of the 40FAH solution under a series of dispensing pressures ranging from 20 to 60 KPa. A higher pressure will extrude more hydrogel solution from the bioprinting needle. Based on the flow behavior pattern obtained from the rheometer test, the flow rate trend can be described and predicted [33], with the result shown in Figure 6.7D.

If the pressure is known, the mass flow rate can be obtained accordingly from the relationship described above. Based on the flow rate, the dispensing head speed is therefore determined in terms of scaffold structural requirements, such as the porosity and structural stability. Because our bioprinting method is combined with the submerge technique by which the hydrogel solution is deposited in a reservoir containing crosslinking solution for scaffold gelation, the concentration of crosslinkers becomes another crucial element to determine the success of scaffold bioprinting. Figure 6.7E shows how the printability is affected by the dispensing head speed and concentration of the calcium crosslinker. In detail, the influence of dispensing head speed on structure's integrity shows that, in a fixed

20 mM of calcium ions, a wide range of speeds (2 to 10 mm/s) can be applied to build scaffolds. In contrast, when the speed is too fast (over 11 mm/s) or too slow (less than 1 mm/s in this case), stacked scaffold with multiple layers is hard to produce. Meanwhile, when the dispensing head speed is preset at a given value, low concentrations of calcium ions (20 to 40 mM) are adequate for the success of scaffold bioprinting. However, three-layer scaffolds are hard to achieve at calcium concentrations >50 mM or <10 mM.

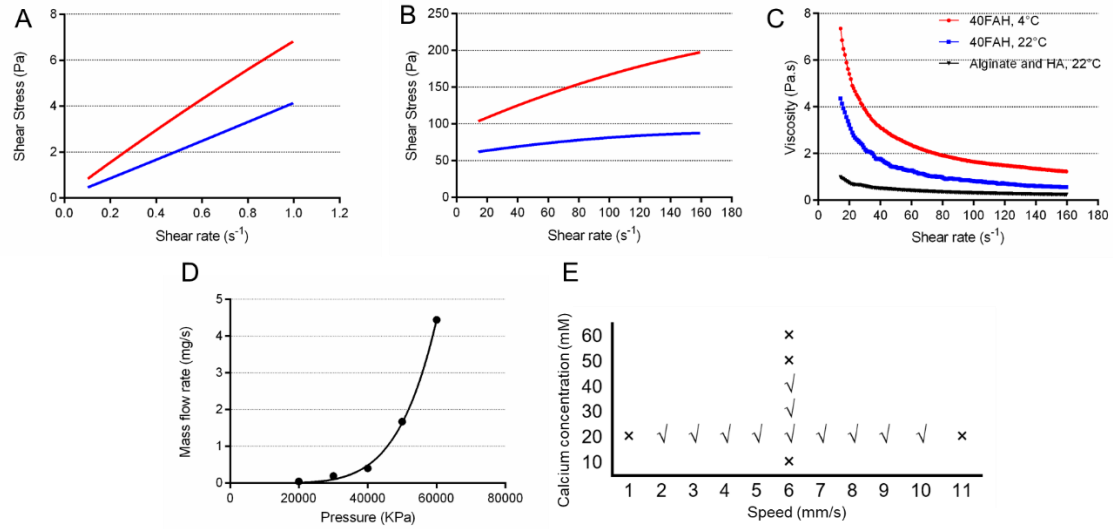

Figure 6. 7 Bioprinting control for building scaffolds: A, shear stress of 40FAH hydrogel at a low shear rate; B, flow behavior of 40FAH hydrogel over a wide range of shear rates; C, mass flow rate under various dispensing pressures; and D, printability under various dispensing head speeds and calcium concentrations (check represents adequate printability, × represents poor printability).

The speed of the dispensing head not only affects the printability of scaffolds but also determines the diameter of scaffold strands and their inner stresses if the dispensing pressure is known. Theoretically, the diameter of a printed strand equals the inner diameter of the bioprinting needle if the dispensing head speed is preset [35]:

$$v = \frac{4Q}{\pi\rho d^2}, \tag{6.3}$$

where v is the speed of the dispensing head, Q is the mass flow rate, ρ is the solution density (close to 1 g/mL herein), and d is the inner diameter of the bioprinting needle. Figure 6.8 shows the variation of strand diameters (top view) under different dispensing head speeds for a constant dispensing pressure and crosslinking solution concentration. A faster speed

can lead to narrower strands under the same dispensing pressure; however, the strands all display larger diameters than predicted by theoretical calculations for the dispensing head speeds applied (theoretical values: 4 mm/s, bigger than needle diameter; 6 mm/s, close to needle diameter; 10 mm/s, less than needle diameter). This is probably due to surface tension of the hydrogel solution as it deposited on the preset surface, and the effect of crosslinking rate [36].

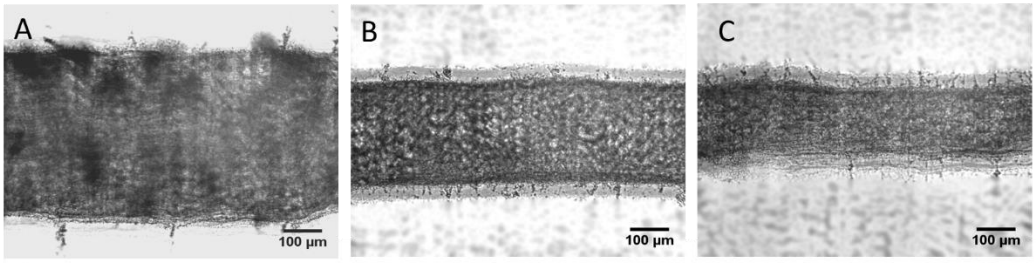

D

	Printed diameter (µm)	Predicted diameter (µm) $(d = \sqrt{\frac{4Q}{\pi\rho v}})$
4 mm/s	515±24	252
6 mm/s	362±13	205
10 mm/s	252±14	160

Figure 6. 8 Influence of dispensing head speed on the diameter of printed strands: strands formed at A, 4 mm/s; B, 6 mm/s; and C, 10 mm/s. D, Comparison of actual and theoretical diameters.

Immunofluorescence staining of fibrin allowed for the observation of fibrin fibers inside the printed strands. Thus, the influence of dispensing head speed on the orientation of fibrin fibers within strands can be observed. Fibrin fibers appeared to be oriented parallel to the printing direction, with this orientation being more obvious when higher dispensing head speeds were applied (Figures 6.9A-C). For example, the strand printed at 2 mm/s had 74.67±8.34% of fibrin fibers distributed within ± 20° of the strand orientation, with this value increasing to 94.36±3.51% at 9 mm/s. However, fibrin fibers in droplets formed random mesh networks, with only 40.67±7.23% of fibers oriented within ±20° relative to the 0° orientation defined for image analysis (Figures 6.9D1, D2).

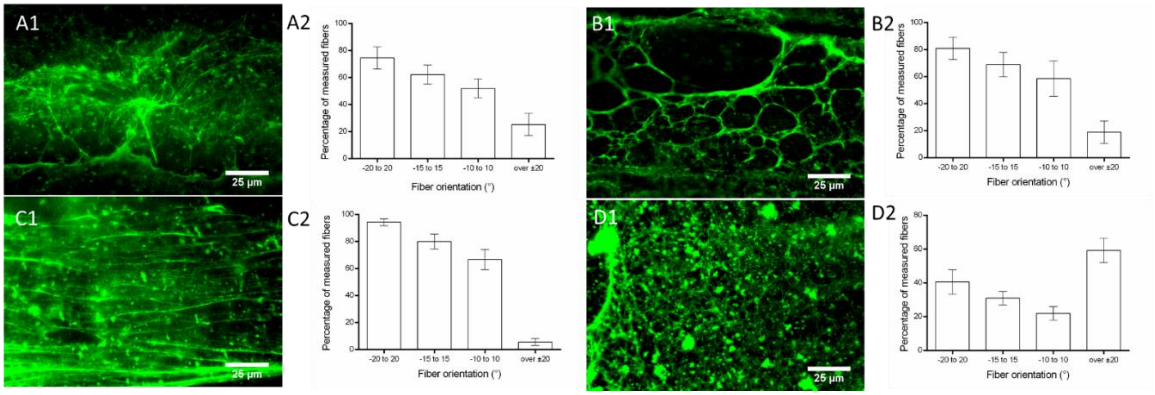

Figure 6. 9 Orientation of fibrin fibers inside printed strands and dispensed droplets: fibrin fiber orientation at a dispensing head speed of A, 2 mm/s; B, 6 mm/s; and C, 9 mm/s. D, Fibrin fiber orientation inside a droplet.

After investigating elements including the flow behavior of the hydrogel solution, dispensing pressure, speed of the dispensing head, and crosslinking agent concentration, scaffolds were produced using low viscosity 40FAH and FRAH solutions, resulting in the printed structures. Figure 6.10 reveals the example of scaffold produced by 40FAH. The 3D multi-layer scaffold has integrated morphologies with predesigned pores and architecture (Figures 6.10A to 6.10C), indicating that porous tissue structures can be achieved using a low viscosity hydrogel solution following our bioprinting method. The sufficient mechanical support from subjacent layers of the scaffold made it stable to be handled by hands or forceps during the transition for image capturing. Both phase retrieval images and 3D reconstructed structure after SR-inline-PCI-CT imaging confirm that the scaffold with fully interconnected channels and pore networks can be fabricated (Figures 6.10D to 6.10F), with the quantitatively average porosities of 39.42±11.93% and 43.65±8.42% for 40FAH and FRAH hydrogel scaffolds, respectively.

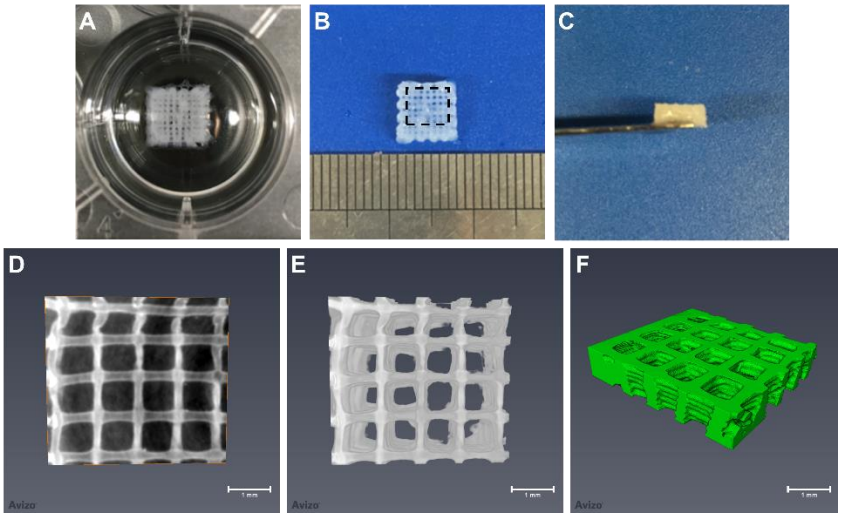

Figure 6. 10 Observations of printed 40FAH scaffolds. A, scaffold in the crosslinking medium after bioprinting; B, top view of scaffold shape and size; C, side view of scaffold; D, a phase retrieval slice of printed scaffold captured using our SR-inline-PCI-CT imaging technique; E, top view of a scaffold after reconstruction; and F, reconstructed 3D scaffold

6.4.3 Performance of Schwann cells encapsulated in 3D scaffolds

The viability of Schwann cells encapsulated in 40FAH and FRAH hydrogel scaffolds was evaluated at days 1, 4, and 10 in culture. Figures 6.11A-F shows that more than 89% of cells were alive in both the 40FAH and FRAH scaffolds at day 1, and this number increased to over 95% by day 4 and 10 (Figure 6.11M). This indicates that our bioprinting technique does not significantly reduce Schwann cell viability, with almost all cells surviving inside the scaffolds for at least 10 days.

Both MTT assay and fluorescent staining were conducted to evaluate the proliferative functions of Schwann cells encapsulated in the scaffolds (Figure 6.11). Standard MTT curves verified the feasibility of our method to analyze the proliferation of both seeded and encapsulated cells due to the linear relations between cell numbers and absorbance (Figure 6.11N). MTT absorbance readings (Figure 6.11O) increased with culture time, demonstrating that the cells were able to proliferate. Absorbance values obtained from the two different scaffolds were similar, suggesting that 40FAH and FRAH hydrogels have similar abilities to maintain the ability of encapsulated cells to proliferate.

Manual counts of Hoechst-stained cells also showed that Schwann cell numbers inside the two scaffolds were continuously increasing, verifying the results of the MTT assay (Figures 6.11G-L, P).

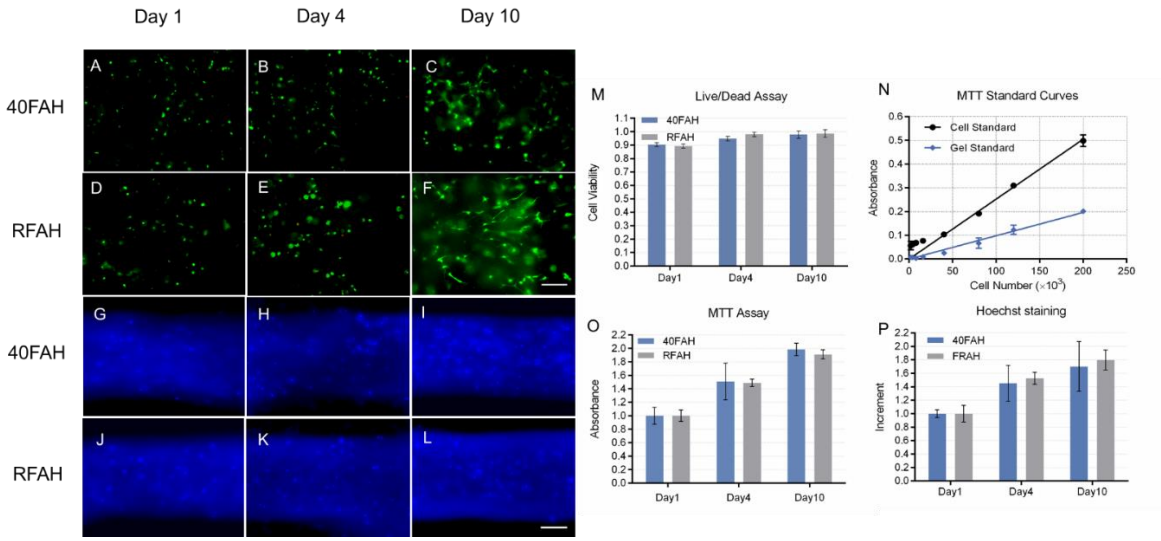

Figure 6. 11 Viability and proliferation of Schwann cells encapsulated in 40FAH and FRAH scaffolds. A-F, live and dead assay by fluorescent staining on days 1, 4, and 10; G-K, Hoechst staining of cells on days 1, 4, and 10; M, statistical cell viability analysis; N, MTT standard curves; O, MTT assay for cell proliferation; P, Statistical cell proliferation analysis from Hoechst staining.

Immunocytochemical staining was employed to quantitatively investigate the performance of the Schwann cells encapsulated in the scaffolds in terms of cell alignment, morphological circularity, and expression of ECM protein laminin. The results for S100 labelled cells are shown in Figure 6.12. Over 52.49±9.50% of cells tended to align parallel to the printed strand (oriented ±20° relative to strand direction) in the 40FAH scaffolds at day 4, with this number rising to over 64.55±7.94% at day 10. Quantitative alignment of cells encapsulated in the FRAH scaffolds was notably higher, at 55.81±8.42% at day 4 and over 76.36±8.77% at day 10. Cellular circularity values for the S100 stained cells of 0.62 and 0.55 at day 4 and 0.56 and 0.53 at day 10 for the 40FAH and FRAH hydrogels, respectively (Figure 6.12G), indicate that the encapsulated cells were well attached to the matrix.

The expression of laminin by Schwann cells was also investigated using laminin immunocytochemistry (Figure 6.12H) because production of this extracellular matrix

protein is thought to be one way in which Schwann cells promote axon growth. The intensity of stained laminin was markedly increased at longer culture times, indicating that the Schwann cells produce increasing amounts of laminin in culture. The intensity was also higher for FRAH scaffolds than for 40FAH scaffolds, but the difference was not significant.

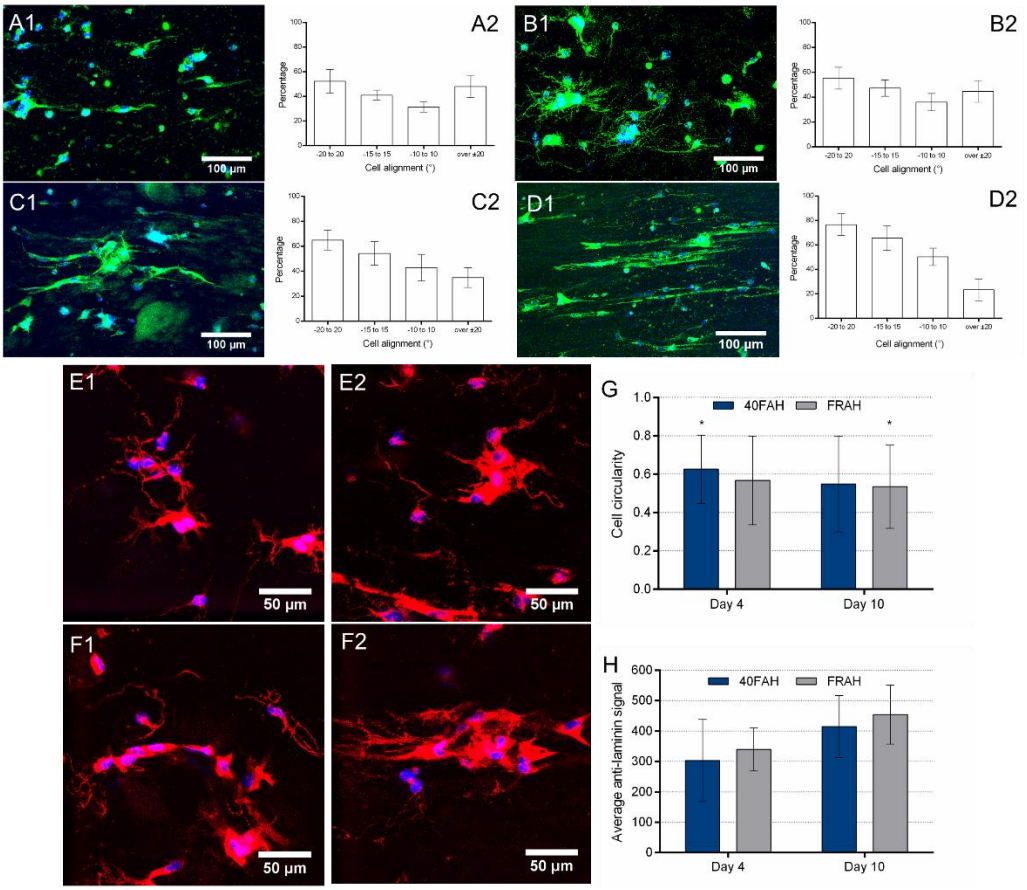

Figure 6. 12 Immunocytochemical staining for Schwann cells encapsulated in hydrogel scaffolds. Schwann cells in 40FAH scaffolds stained with S100 at A1, day 4 and B1, day 10. Schwann cells in FRAH scaffolds stained with S100 at C1, day 4 and D1, day 10. A2, B2, C2, D2 cell alignment statistics. Cells in E1, E2 40FAH scaffolds and F1, F2 FRAH scaffolds stained with anti-laminin at day 4 and 10. G, quantification of cell circularity in 40FAH and FRAH scaffolds. H, quantification of laminin expression in 40FAH and FRAH scaffolds. *represents $p<0.05$.

6.5 Discussion

The success of scaffold bioprinting with encapsulated cells normally needs first, tailored hydrogels to support functions of cells, and second, bioprinting method to produce

a scaffold with expected stability and structure. Since most individual hydrogel faces either biological or printable problems, using multiple hydrogels becomes one option which covers drawbacks from individual hydrogel and may capitalize on the benefits of each. By tuning the concentrations, the tailored hydrogel mixture can be achieved to promote the functions of cells. It is also known that using high concentrations of hydrogel usually increases the solution viscosity, making for easier manipulation in bioprinting and production of scaffolds with good structural support. Low concentrations decrease solution viscosity and can compromise bioprintability, but it often provides more suitable environment for cells after gelation [7]. Here, we kept low concentrations of 1% alginate and 0.5% HA in the mixture based on the performance of Schwann cells [13, 20], while examined fibrinogen (to produce fibrin) concentrations from 10 to 40 mg/mL. We also used RGD modified alginate (1%) as a biomaterial because covalently bonding RGD peptide to alginate provides adhesion sites and thus improves cell attachment to alginate [26].

The hydrogel microstructures and cell morphologies observed indicate that encapsulated Schwann cells perform better in an environment with a high concentration of fibrin that offers sufficient micro-scale pores and fibers for cell metabolism and attachment. Although low concentrations of fibrin provide cell-binding fibers in the hydrogel, inadequate porosity can still restrict achievement of the spreading phenotype of Schwann cells. SEM images showed that alginate and RGD modified alginate have similar microstructures, but that more cells spread in the RGD modified alginate when other conditions are held constant.

The mechanical stiffness of a hydrogel has significant effects on both surface-seeded and encapsulated cells [37, 38]. Previous study illustrated that Schwann cells prefer a softer environment in culture when alginate is used as a cell substrate [13]. Here, we employed the plane strain compression test to measure hydrogel stiffness. This method is usually applied in metal forming and tribological simulation, and becomes useful for thin or soft material samples that pose challenges for classical tensile or uniaxial compression tests. It can determine stress-strain curves up to considerably higher strains than tensile tests using far less material, thus allowing the exploration of a wider range of deformations without instability [39]. Results here show that adding fibrin can enhance the mechanical

stiffness of hydrogels, but not significantly. In the first 30% of equivalent strain, all hydrogel samples share a similar stress-strain trend. As combined with cell circularity results, it appears that Schwann cells are more sensitive to biological cues compared to the mechanical properties when the mechanical stiffness of hydrogel substrates is at a low level.

The bioprintability of a hydrogel solution can generally be determined by its flow behavior and crosslinking mechanism [40-42]. A bioprintable solution should be regulated and controlled in the bioprinting process, and crosslinked with sufficient mechanical stability after structural deposition. Therefore, the evaluation of flow behavior is very important and provides four important pieces of information for bioprinting. First, flow pattern. Most biomaterial solutions exhibit non-Newtonian flow behavior, and those with a shear thinning flow pattern are commonly recommended in bioprinting due to their ability to reduce the viscosity at high shear rates, i.e., in the bioprinting needle, therefore making it easy for solution to flow through the needle [43]. Second, viscosity. High viscosity materials are easily deposited but may restrict cell functions and cause cell damage because a high dispensing pressure is required [34, 44]. Low viscosity biomaterial solutions are good with respect to cell performance, but may have problem in bioprinting control and structural stability. Therefore, evaluating the viscosity of a biomaterial solution indicates if the solution is appropriate for the bioprinting process. The viscosity of biomaterial solutions can be altered not only by the hydrogel concentration but also by temperature [45]. Increasing temperature normally decrease solution viscosity and vice versa; therefore, selecting suitable temperatures is required for the expected viscosity to be obtained. Generally, printing temperature is kept within a certain range (0 - 37°C) in order to preserve cell viability. Third, the flow rate in bioprinting can be calculated beforehand if the flow behavior is known [33, 46]. For a given needle size and dispensing pressure, the flow rate of a solution can be predicted and thus the dispensing head speed selected based on the required strand size. Last, as biomaterial solution is forced through the needle, stresses such as shear stress and extensional stress can be introduced, which can deform cells and potentially breach cell membranes [45, 47]. By evaluating the flow behavior of the biomaterial solution, the stresses produced during bioprinting can be theoretically calculated, which helps the prediction of cell damage during bioprinting [7, 34].

Bioprinting with submerged crosslinking technique used in present study can relieve the problem in bioprinting scaffolds by low viscosity hydrogel solution. It provides adequate crosslinking agents and keeps the construct moist during strands deposition, therefore ensures the gelation of biomaterials and the stack of scaffold layers without causing shrinkage. Moreover, it favors the formation of porous structures and preserve the vertical collapse because of the buoyancy provided by the crosslinking medium. However, this method is only suitable for materials that have a relatively rapid crosslinking rate, otherwise the buoyancy would have negative effect on structural stacking [7]. Our previous work illustrates that coating the predefined deposition area with the polycation PEI is essential for ensuring the stability of the first structural layer; the buoyancy effect and crosslinking rate can be adjusted by adding polyvinyl alcohol (PVA) to the crosslinking medium to fabricate multiple-layer alginate scaffolds [20]. In the present study, we simplified the procedure by only modulating the calcium ion concentration and the dispensing head speed to adjust the crosslinking rate, with scaffolds being successfully produced.

Effectively directing the growth of cells and facilitating tissue regeneration is in the ultimate goal of scaffold-based tissue engineering [48]. For nerve repair, it is important to provide a linearly arrayed substrate for the growth of regenerating axons in one direction. Here, we studied the alignment of fibrin fibers within the strand because the molecular structure of fibrin enables fibrin fiber networks to undergo reorganization when external stresses or tensions are applied [49]. The shear stress and shear thinning experienced by the hydrogels as they are dispensed through the needle could be used to reorganize the polymeric chains such as fibrin into a more linear and stretched conformation [50]. The present study also demonstrates that fibers can be further aligned by increasing the dispensing head speed at a given dispensing pressure because higher speeds can further stretch it in the direction of movement thus provide tensile stress inside the printed strand after gelation. Compared to other methods, controlling the dispensing head speed in 3D bioprinting is much easier to organize the orientation of fibers [51, 52].

Structural evaluation of scaffold provides necessary evidence to verify the feasibility of bioprinting method. An efficient, accurate and nondestructive evaluation technique which faithfully represents the structure of scaffold is therefore demanded. The

SR-inline-PCI-CT shows promise for the non-invasive 3D visualization of hydrogel scaffolds both *in vitro* and in longitudinal animal studies. It has great utility for soft tissue engineering due to its capacity to overcome the limited absorption difference between hydrogel scaffolds and natural tissues by deriving contrast from refraction or phase effects rather than absorption [53]. Compared to other evaluation method such as laboratory based micro-CT scanning, hydrogel scaffold can be scanned directly without any further treatment, overcoming the problem of partial damage in post-processing. In addition, the scanning process is much faster compared to laboratory based micro-CT scanning, which makes it possible to investigate many samples within a short period. Here, clear 3D images of porous scaffolds with fully interconnected channels were reconstructed, proving the feasibility of our bioprinting method in hydrogel scaffold fabrication, demonstrating the great potential of synchrotron phase-based X-ray imaging techniques to inform tissue engineering and biofabrication.

The live/dead assay showed over 89% live Schwann cells at 1 day after bioprinting, demonstrating the effectiveness of our bioprinting method in preserving the viability of Schwann cells. This is attributed to the low bioprinting pressure and therefore low process-induced stresses [54]. Results of cell viability in 10 days also verifies the biocompatibility of the materials and the suitability of scaffold structures to maintain high cell viability [7, 45]. Cell proliferation results demonstrate that the proliferative functions of Schwann cells can be maintained in both 40FAH and FRAH scaffolds, with similar trends of cell number increase in the two scaffolds types.

Immunocytochemical labeling of Schwann cells demonstrates that the cellular alignment along the longitudinal axis of the strand can be induced. At day 4 of culture, Schwann cells started to spread along the longitudinal axis of strand, and after culturing for 10 d, most of cells were elongated and reoriented following the direction of strand. This is probably due to the physical guidance cues provided by aligned fibrin fibers as tensile stress is included. It can predict that simply encapsulating Schwann cells in hydrogels cannot regulate cellular organization, and the alignment of cells would not be induced if only carbohydrate-based hydrogels are used to build the structure [20, 55]. Because the orientation of fibrin fiber is highly responsive to mechanical stress and tension, a simple

strategy based on controlling bioprinting pressures and dispensing head speeds can be employed to regulate the orientation of cells inside scaffolds [56].

Laminin is a major glycoprotein of the extracellular matrix of nerve tissue and appears to be an important guidance molecule for axon growth. It can also stimulate the mitosis of Schwann cells that form myelin around mature axons in the PNS [57, 58]. The location of anti-laminin labeled cells indicated the extensive penetration of laminin inside the scaffolds, demonstrating the ability of encapsulated Schwann cells to express proteins within the hydrogel matrix. Quantitative analysis of laminin intensity showed that the expression of laminin can be facilitated by regulating biomaterial composition, e.g., if RGD is included in the scaffold biomaterials. However, the difference in laminin deposition between RGD and non-RGD scaffolds was not statistically significant. This result verifies the importance of fibrin as a scaffold biomaterial to ensure the beneficial performance of Schwann cells.

6.6 Conclusions

This chapter presents a comprehensive study for bioprinting hydrogel scaffolds with encapsulated Schwann cells. Properties of prepared hydrogels were investigated including the microstructure and mechanical stiffness. It is determined that not only the cell-binding sites, but also the porosity of hydrogel can significantly affect the attachment of Schwann cells. With observed Schwann cell spreading, hydrogel compositions including 40FAH and FRAH were determined for further scaffold bioprinting. Mechanically stable scaffolds with integrated structures can be printed using the prepared hydrogel compositions by controlling the dispensing pressure, dispensing head speed, and concentration of calcium in crosslinking solution in certain ranges. The scaffolds obtained from this developed bioprinting process can support the performance of encapsulated Schwann cells in terms of high cell viability, proliferation and cellular protein expression. Moreover, high bioprinting speed in the printable range can realigning fibrin fiber in the longitudinal axis of strand, and the reorganized fibers facilitate Schwann cell elongation and alignment in the same direction. Overall, hydrogel preparation and bioprinting processes developed in this chapter is feasible to produce scaffolds bearing living, oriented

Schwann cells, which have great potential for supporting peripheral nerve regeneration after injury.

6.7 References

[1] Langer R, Vacanti JP. 1993 Tissue engineering. *Science*. 260 920-26.

[2] Rajaram A, Chen XB, Schreyer JD. 2012 Strategic design and recent fabrication techniques for bioengineered tissue scaffolds to improve peripheral nerve regeneration. *Tissue Eng. Part B.* 18 454-67.

[3] Gu Y, Zhu J, Xue C, Li Z, Ding F, YanY, Gu X. 2014 Chitosan/silk fibroin-based, Schwann cell-derived extracellular matrix-modified scaffolds for bridging rat sciatic nerve gaps. *Biomaterials*. 35 2253-63.

[4] Hutmacher DW, Sittinger M, Risbud MV. 2004 Scaffold-based tissue engineering: rationale for computer-aided design and solid free-form fabrication systems. *Trends Biotechnol*. 22 354-62.

[5] Kijeńska E, Prabhakaran MP, Swieszkowski W, Kurzydlowski K, Ramakrishna S. 2014 Interaction of Schwann cells with laminin encapsulated PLCL core–shell nanofibers for nerve tissue engineering. *Eur Polym J.* 50 30-38.

[6] Struzyna LA, Katiyar K, Cullen DK. 2014 Living scaffolds for neuroregeneration. *Curr Opin Solid State Mater Sci.* 18 308-18.

[7] Ning L, Chen X. 2017 A brief review of extrusion-based tissue scaffold bio-printing. *Biotech J*. 12 1600671.

[8] Williams DF. 2008 On the mechanisms of biocompatibility. *Biomaterials*. 29 2941-53.

[9] Lee KY, Mooney DJ. 2001 Hydrogels for tissue engineering. *Chem Rev*. 101 1869-80.

[10] Benoit DS, Schwartz MP, Durney AR, Anseth KS. 2008 Small functional groups for controlled differentiation of hydrogel-encapsulated human mesenchymal stem cells. *Nat Mater.* 7 816-23.

[11] Wendt D, Marsano A, Jakob M, Heberer M, Martin I. 2003 Oscillating perfusion of cell suspensions through three-dimensional scaffolds enhances cell seeding efficiency and uniformity. *Biotechnol Bioeng.* 84 205-14.

[12] Hunt NC, Grover LM. 2010 Cell encapsulation using biopolymer gels for regenerative medicine. *Biotechnol Lett.* 32 733-42.

[13] Ning L, Xu Y, Chen X, Schreyer DJ. 2016 Influence of mechanical properties of alginate-based substrates on the performance of Schwann cells in culture. *J Biomater Sci Polym Ed*. 27 898-915.

[14] Hollister SJ. 2005 Porous scaffold design for tissue engineering. *Nat. Mater*. 4 518-24.

[15] Kang HW, Lee SJ, Ko IK, Kenglea C, Yoo JJ, Atala A. 2016 A 3D bioprinting system to produce human-scale tissue constructs with structural integrity. *Nat Biotechnol*. 34 312-19.

[16] Mehrban N, Teoh GZ, Birchall MA. 2016 3D bioprinting for tissue engineering: Stem cells in hydrogels. *Inter J Bioprinting*. 2 6-19.

[17] Levato R, Visser J, Planell JA, Engel E, Malda J, Mateos-Timoneda, MA. 2014 Biofabrication of tissue constructs by 3D bioprinting of cell-laden microcarriers. *Biofabrication*. 6 035020.

[18] Fedorovich NE, De Wijn JR, Verbout AJ, Alblas J, Dhert W. 2008 Three-dimensional fiber deposition of cell-laden, viable, patterned constructs for bone tissue printing. *Tissue Eng Part A*. 14 127-33.

[19] Augst AD, Kong HJ, Mooney DJ. 2006 Alginate hydrogels as biomaterials. *Macromol Biosci*. 6 623-33.

[20] Rajaram A, Schreyer JD, Chen D. 2014 Bioplotting alginate/hyaluronic acid hydrogel scaffolds with structural integrity and preserved schwann cell viability. *3D Printing Add Manuf*. 1 194-203.

[21] Baier LJ, Bivens KA, Patrick CW, Schmidt CE. 2003 Photocrosslinked hyaluronic acid hydrogels: natural, biodegradable tissue engineering scaffolds. *Biotechnol Bioeng*. 82 578-89.

[22] Ahmed TA, Dare EV, Hincke M. 2008 Fibrin: a versatile scaffold for tissue engineering applications. *Tissue Eng Part B*. 14 199-215.

[23] England S, Rajaram A, Schreyer DJ, Chen XB. 2017 Bioprinted fibrin-factor XIII-hyaluronate hydrogel scaffolds with encapsulated Schwann cells and their in vitro characterization for use in nerve regeneration. *Bioprinting*. 5 1-9.

[24] Weisel JW. 2004 The mechanical properties of fibrin for basic scientists and clinicians. *Biophys Chem*. 112 267-76.

[25] Lee YB, Polio S, Lee W, Dai GH, Menon L, Carroll, RS, Yoo SS. 2010 Bio-printing of collagen and VEGF-releasing fibrin gel scaffolds for neural stem cell culture. *Exp Neurol*. 223 645-52.

[26] Rowley JA, Madlambayan G, Mooney DJ. 1999 Alginate hydrogels as synthetic extracellular matrix materials. *Biomaterials*. 20 45-53.

[27] Aksenov SA, Puzino YA, Bober SA, Kliber J. 2015 Processing of plane strain compression test results for investigation of AISI-304 stainless steel constitutive behavior. *J Chem Tech Metallurgy*. 50 644-50.

[28] Kaewkhaw R, Scutt AM, Haycock JW. 2012 Integrated culture and purification of rat Schwann cells from freshly isolated adult tissue. *Nat Protoc.* 7 1996.

[29] Wang MD, Zhai P, Schreyer DJ, Zheng RS, Sun XD, Cui FZ, Chen XB. 2013 Novel crosslinked alginate/hyaluronic acid hydrogels for nerve tissue engineering. *Front Mater Sci*. 7 269-84.

[30] Liao YT, Wu KCW, Yu J. 2014 Synthesis of mesoporous silica nanoparticle-encapsulated alginate microparticles for sustained release and targeting therapy. *J Biomed Mater Res Part B Appl Biomater*. 102 293-302.

[31] Devi MP, Sekar M, Chamundeswari M, Moorthy A, Krithiga G, Murugan NS, Sastry TP. 2012 A novel wound dressing material-fibrin–chitosan–sodium alginate composite sheet. *Bull Mater Sci*. 35 1157-63.

[32] Chhabra RP, Richardson JF. 1999 Non-Newtonian flow in the process industries: fundamentals and engineering applications. Butterworth-Heinemann, Oxford,.

[33] Chen X, Li M, Ke H. 2008 Modeling of the flow rate in the dispensing-based process for fabricating tissue scaffolds. *J Manuf Sci Eng*. 130 021003.

[34] Li M, Tian X, Zhu N, Schreyer DJ, Chen XB. 2009 Modeling process-induced cell damage in the biodispensing process. *Tissue Eng Part C*. 16 533-42.

[35] Tian X, Li M, Cao N, Li JW, Chen XB. 2009 Characterization of the flow behavior of alginate/hydroxyapatite mixtures for tissue scaffold fabrication. *Biofabrication*. 1 045005.

[36] Chen X, Ke H. 2006 Effects of fluid properties on dispensing processes for electronics packaging. *IEEE Trans Electron Packag Manuf* 29 75-82.

[37] Gu Y, Ji Y, Zhao Y, Liu Y, Ding F, Gu XS, Yang YM. 2012 The influence of substrate stiffness on the behavior and functions of Schwann cells in culture. *Biomaterials*. 33 6672-81.

[38] Huang G, Wang L, Wang S, Han YL, Wu JH, Zhang QC, Xu F, Lu TJ. 2012 Engineering three-dimensional cell mechanical microenvironment with hydrogels. *Biofabrication*. 4 042001.

[39] Tritz J, Rahouadj R, de Isla N, Charif N, Pinzano A, Mainard D, Bensoussan D, Netter P, Stoltz JF, Benkirane JN. 2010 Designing a three-dimensional alginate hydrogel by spraying method for cartilage tissue engineering. *Soft Matter*. 6 5165-74.

[40] Ozbolat IT, Hospodiuk M. 2016 Current advances and future perspectives in extrusion-based bioprinting. *Biomaterials*. 76 321-43.

[41] Choi YJ, Kim TG, Jeong J, Yi HG, Park JW, Hwang W, Cho, DW. 2016 3D Cell Printing of Functional Skeletal Muscle Constructs Using Skeletal Muscle-Derived Bioink. *Adv Healthc Mater*. 5 2636-45.

[42] Dolati F, Yu Y, Zhang Y, DeJesus, AM, Sander EA, Ozbolat IT. 2014 In vitro evaluation of carbon-nanotube-reinforced bioprintable vascular conduits. *Nanotechn*. 25 145101.

[43] Guvendiren M, Lu HD, Burdick JA. 2012 Shear-thinning hydrogels for biomedical applications. *Soft Matter*. 8 260-72.

[44] Billiet T, Gevaert E, De Schryver T, Cornelissen M, Dubruel P. 2014 The 3D printing of gelatin methacrylamide cell-laden tissue-engineered constructs with high cell viability. *Biomaterials*. 35 49-62.

[45] Ning L, Guillemot A, Zhao J, Kipouros G, Chen XB. 2016 Influence of flow behavior of alginate-cell suspensions on cell viability and proliferation. *Tissue Eng Part C*. 22 252-62.

[46] Li M, Tian X, Schreyer DJ, Chen XB. 2011 Effect of needle geometry on flow rate and cell damage in the dispensing-based biofabrication process. *Biotechnol Prog*. 27 1777-1784.

[47] Bae YB, Jang HK, Shin TH, Phukan G, Tran TT, Lee G, Hwang WR, Kim JM. 2016 Microfluidic assessment of mechanical cell damage by extensional stress. *Lab Chip*. 16 96-103.

[48] Kim HN, Jiao A, Hwang NS, Kim MS, Kim DH, Suh KY. 2013 Nanotopography-guided tissue engineering and regenerative medicine. *Adv Drug Del Rev.* 65 536-58.

[49] Liu W, Carlisle C, Sparks E, Guthold M. 2010 The mechanical properties of single fibrin fibers. *J Thromb Haemost*. 8 1030-36.

[50] Malda J, Visser J, Melchels FP, Jungst T, Hennink WE, Dhert W, Groll J, Hutmacher DW. 2013 25th anniversary article: engineering hydrogels for biofabrication. *Adv Mater*. 25 5011-28.

[51] Lopez-Lopez MT, Scionti G, Oliveira AC, Duran J, Campos A, Alaminos M, Rodriguez IA. 2015 Generation and characterization of novel magnetic field-responsive biomaterials. *PLoS One*. 10 E0133878.

[52] Matsumoto T, Sasaki JI, Alsberg E, Egusa H, Yatani H, Sohmura T. 2007 Three-dimensional cell and tissue patterning in a strained fibrin gel system. *PLoS One*. 2 E1211.

[53] Izadifar Z, Honaramooz A, Wiebe S, Belev G, Chen XB, Chapman D. 2016 Low-dose phase-based X-ray imaging techniques for in situ soft tissue engineering assessments. *Biomaterials*. 82 151-67.

[54] Chang R, Nam J, Sun W. 2008 Effects of dispensing pressure and nozzle diameter on cell survival from solid freeform fabrication-based direct cell writing. *Tissue Eng Part A*. 14 41-48.

[55] Khademhosseini A, Vacanti JP, Langer R. 2009 Progress in tissue engineering. *Sci Am.* 300 64-71.

[56] Mozetic P, Maria Giannitelli S, Gori M, Trombetta M, Rainer A. 2017 Engineering muscle cell alignment through 3D bioprinting. *J Biomed Mater Res Part A*. 105 2582-88.

[57] Cohen J, Burne JF, McKinlay C, Winter J. 1987 The role of laminin and the laminin/fibronectin receptor complex in the outgrowth of retinal ganglion cell axons. *Dev Biol*. 122 407-18.

[58] Zhu N, Li M, Guan Y, Schreyer DJ, Chen XB. 2010 Effects of laminin blended with chitosan on axon guidance on patterned substrates. *Biofabrication*. 2 045002.

CHAPTER 7

Conclusions and Future Recommendations

7.1 Conclusions

Extrusion-based bioprinting has evolved, showing great promise for fabricating scaffolds in tissue engineering. Despite its advances, fabricating customized scaffolds from hydrogels containing living cells, however, is still in its infancy, where the major issues are the viability and functionality of the incorporated cells and the scaffold structural stability and integrity. As these issues are heavily influenced by the properties of hydrogel and the bioprinting process, this thesis was aimed at addressing these issues, particularly (1) investigating the influences of hydrogel properties and the bioprinting process on cell viability and functionality, and (2) developing bioprinting processes to fabricate cell-encapsulated, hydrogel-based scaffolds. From this research, several main conclusions were achieved and outlined as follows:

- The limited cell-binding property of alginate hydrogel can be improved with the addition of cell-adhesion supplements. Additionally, the physiological performance and morphological appearance of cells also can be improved and regulated by the mechanical stiffness of hydrogel substrate. Softer hydrogels provide a more conducive environment for biological functions (i.e., proliferation, spreading, and protein secretion) for Schwann cells in culture.
- Cell damage is associated the magnitude and duration of shear stress that the cells experience; particularly, increasing the magnitude and/or duration of shear stress increases the percent cell damage, resulting in the reduction of cell viability and proliferation. Inherently, different cell types demonstrate variation in ability to resist shear stress based on their own cellular properties.
- Cell damage occurring in the bioprinting process is caused by both shear and extensional stresses that the bioprinting process inflicts on the cells. With the help of developed models, the bioprinting process-induced cell damage can be represented and predicted.

- Most damaged Schwann cells and myoblasts die within a short period of time after bioprinting, while only a small number of the damaged cells can recover and survive during culture subsequently.
- The addition of fibrin at an appropriate concentration in alginate/HA/RGD composited hydrogels can greatly improve cell attachment.
- The developed extrusion-based 3D bioprinting process is able to fabricate hydrogel-based, cell-encapsulated scaffolds, with the appropriate structural stability and biologically-conducive support for the encapsulated cells during culture.
- The parameters set for the bioprinting process, such as dispensing pressure, dispensing head speed, and concentration of crosslinking agent, are important to the stability of printed scaffolds and the cell viability/functionality. It is illustrated that with the appropriate settings of process parameters, scaffolds can be printed with structural integrity and a fully interconnected channel architecture, and suitable for supporting cellular functions, as examined in terms of viability, proliferation, spreading, alignment, and protein secretion *in vitro*.

7.2 Future Recommendations

With achievements from this thesis, some recommendations and suggested projects for future studies are given as follow:

1. It is always important to explore new hydrogel or other material types, or significantly simplify the process for synthesizing current materials to achieve the required cell functions in scaffold bioprinting. This thesis verified the compatibility of a multi-component hydrogel for scaffold biofabrication with incorporated living cells, which also suggested the potential of hydrogels for incorporating other biological elements, such as bioactive molecules in bioprinting. Using multiple hydrogels in creating a scaffold takes the advantages from each type, and shows improvements for scaffolds and living cells, however, the process presented in this thesis is normally time-consuming and requires elaborate preparation. To overcome this issue, the development of novel biomaterials which possess both biocompatibility and bioprintability are highly recommended. Recent studies indicate that the developed gelatin methacryloyl (GelMA) has properties to maintain the structural integrity while

facilitate the performance of cells in scaffold bioprinting for several cell types. Therefore in the future, bioprinting scaffolds by GelMA and Schwann cells can be conducted for nerve tissue engineering applications.

2. The physical mechanism behind the cell damage during the 3D bioprinting process needs to be investigated and understood by taking into account cellular mechanisms. Models which describe the relationship between cell damage to the bioprinting process-induced extensional and shear stress have been established in this thesis. As these models are empirically built based on cell damage experiments in bioprinting, they lack the ability to describe the physical mechanism of cell damage induced by stresses, therefore, it would be interesting to explore the cell damage by considering the cellular mechanisms induced under stress. With such an investigation, the model of describing the relationship between the mechanical resistance of a cell to stress can be built, which would then be used to represent cell damage caused by the bioprinting process. This would be beneficial for predicting cell damage and optimizing cell viability. It is noteworthy that using a tapered needle to replace a cylindrical one significantly reduces the percent cell damage. This result suggests that by optimizing the structural design of the bioprinting needle, the viability of cells after bioprinting might be significantly improved, which can be a research recommendation in the future.
3. The 3D bioprinting process can be further improved in terms of scaffold stability and integrity. Although the feasibility of the bioprinting process presented in this thesis, including hydrogel solution preparation, dispensing parameters control, and crosslinking evaluation, has been proved for hydrogel-based scaffold biofabrication, the structural stability of printed scaffolds is still limited by inherent mechanical properties of hydrogels. To overcome this, development of a multi-material bioprinting process is suggested for producing scaffolds. As an example of this process, polymers such as PCL can be printed as frame to provide sufficient structural support, while hydrogels containing living cells can subsequently be printed onto the formed frame to perform the biological functions of scaffolds.
4. Scaffolds with Schwann cells need to be examined *in vivo* for nerve tissue regeneration. This thesis has shown the promising biological performances of 3D printed scaffolds

with encapsulated Schwann cells by means of the *in vitro* evaluations, which preliminary proves the function of printed scaffolds to facilitate the reconnection of peripheral nerve axons. In the future, long-term *in vivo* investigation on the continuation of nerve tissue regeneration using scaffolds implanted between the injured nerve segments would be highly recommended. Moving forward with *in vivo* test, a more challenging problem in nerve tissue engineering is to guide the growth of segmented axons towards their target tissue. As peripheral nerve tissue is spatially-organized by cells and other biological components, to facilitate the regeneration of nerve tissue, investigating the capability of making customized, biomimetic, and cell-localized scaffolds using 3D bioprinting methods is suggested. In this thesis it was demonstrated that the alignment of Schwann cell inside the scaffold can be regulated by simply controlling the dispensing head speed. Such a scaffold has the potential to efficiently guide the growth of axons. Therefore, developing novel bioprinting processes to produce spatially-organized, Schwann cell-containing scaffolds which are designed to direct axon growth in nerve tissue engineering is highly recommended in the future.